EUROPEAN ORGANIZATION FOR NUCLEAR RESEARCH

CERN-EP/90-25
22 February 1990

ALEPH: A DETECTOR FOR ELECTRON-POSITRON ANNIHILATIONS AT LEP

The ALEPH Collaboration*)

ABSTRACT

The design, construction, and performance of a large-mass 4π solid-angle detector with solenoidal magnet is described. The detector serves to study electron–positron annihilation processes at centre-of-mass energies between 80 and 200 GeV at the Large Electron–Positron storage ring (LEP) at CERN.

(Submitted to Nuclear Instruments and Methods)

---

*) See next pages for the list of authors.

The ALEPH Collaboration

D. Decamp, B. Deschizeaux, J.-P. Lees, M.-N. Minard

Laboratoire de Physique des Particules (LAPP), IN^{2}P^3-CNRS, 74019 Annecy-le-Vieux Cedex, France

J.M. Crespo, M. Delfino, E. Fernandez[1], M. Martinez, R. Miquel, Ll.M. Mir, S. Orteu, A. Pacheco, J.A. Perlas, E. Tubau

Laboratorio de Fisica de Altas Energias, Universidad Autonoma de Barcelona, 08193 Bellaterra (Barcelona), Spain[21]

M.G. Catanesi, M. de Palma, A. Farilla, G. Iaselli, G. Maggi, A. Mastrogiacomo, S. Natali, S. Nuzzo, A. Ranieri, G. Raso, F. Romano, F. Ruggieri, G. Selvaggi, L. Silvestris, P. Tempesta, G. Zito

INFN Sezione di Bari e Dipartimento di Fisica dell' Università, 70126 Bari, Italy

Y. Chen, H. Hu, D. Huang, Y. Jiang, J. Lin, R. Liu, W. Lu, T. Ruan, T. Wang, X. Wang, D. Wu, W. Wu, Y. Xie, D. Xu, R. Xu, Y. Xu, W. Yan, M. Ye, J. Zhang, H. Zhao W. Zhao

Institute of High-Energy Physics, Academia Sinica, Beijing, The People's Republic of China[22]

H. Albrecht[2], A. Ball, F. Bird, E. Blucher, T. Charity, H. Drevermann, F. Dydak, M. Ferro-Luzzi, Ll. Garrido, C. Grab, R. Grub, R. Hagelberg, S. Haywood, B. Ivesdal, B. Jost, M. Kasemann, G. Kellner, J. Knobloch, A. Lacourt, P. Lazeyras, I. Lehraus, B. Lofstedt, T. Lohse, D. Lüke[2], A. Marchioro, P. Mato, J.M. Maugain, J. May, V. Mertens, A. Minten, A. Miotto, P. Palazzi, M. Pepe-Altarelli, R. Pintus, L. Pregernig, M. Price, F. Ranjard, J. Richstein[3], W. Richter, J. Rothberg[4], H. Rotscheidt, W. von Rüden, R. St.Denis, P. Schilly, D. Schlatter, G. Stefanini, M. Takashima, M. Talby[5], J.C. Tarle, H. Taureg, W. Tejessy, H. Verweij, H. Wachsmuth, H. Wahl, S. Wheeler, W. Witzeling, J. Wotschack

European Laboratory for Particle Physics (CERN), 1211 Geneva 23, Switzerland

Z. Ajaltouni, M. Bardadin-Otwinowska, M. Brossard, R. Chadelas, F. Daudon, A. Falvard, P. Gay, P. Henrard, J. Jousset, B. Michel, J-C. Montret, D. Pallin, P. Perret, J. Prat, J. Proriol, F. Prulhière

Laboratoire de Physique Corpusculaire, Université Blaise Pascal, IN^{2}P^3-CNRS, Clermont-Ferrand, 63177 Aubière, France

H. Bertelsen, F. Hansen, J.D. Hansen, J.R. Hansen, P.H. Hansen, A. Lindahl, B. Madsen, R. Mø llerud, B.S. Nilsson, G. Petersen

Niels Bohr Institute, 2100 Copenhagen, Denmark[23]

E. Simopoulou, A. Vayaki

Nuclear Research Center Demokritos (NRCD), Athens, Greece

J. Badier, D. Bernard, M. Bercher, U. Berthon, A. Blondel, G. Bonneaud, J. Bourotte, F. Braems, J.C. Brient, A. Busata, M.A. Ciocci, Ph. Delcroz[33], G. Fouque, R. Guirlet, C. Lemoine, P. Matricon, M. Maubras, R. Morano, P. Miné, J.Y. Parey, P. Poilleux, A. Rougé, C. Roy, M. Rumpf, H. Videau, I. Videau[1], C. Violet, D. Zwierski

Laboratoire de Physique Nucléaire et des Hautes Energies, Ecole Polytechnique, IN^{2}P^3-CNRS, 91128 Palaiseau Cedex, France

D.J. Candlin, A.J. Main

Department of Physics, University of Edinburgh, Edinburgh EH9 3JZ, United Kingdom[24]

A. Conti, G. Parrini, E. Scarlini

Dipartimento di Fisica, Università di Firenze, INFN Sezione di Firenze, 50125 Firenze, Italy

W. Burley, M. Corden, C. Georgiopoulos, J.H. Goldman, M. Ikeda, J. Lannutti, D. Levinthal[29], M. Mermikides, L. Sawyer

Supercomputer Computations Research Institute and Dept. of Physics, Florida State University, Tallahassee FL 32306, USA[25],[26],[27]

A. Antonelli, R. Baldini, G. Bencivenni, G. Bologna[6], F. Bossi, P. Campana, G. Capon, V. Chiarella, G. Corradi, G. De Ninno, B. D'Ettorre-Piazzoli[7], B. Dulach, G. Felici, P. Laurelli, G. Mannocchi[7], F. Murtas, G.P. Murtas, G. Nicoletti, M. Pallotta, P. Picchi[6], P. Zografou

Laboratori Nazionali dell'INFN (LNF-INFN), 00044 Frascati, Italy

B. Altoon, O. Boyle, A.J. Flavell, A.W. Halley, I. ten Have, J.L. Hearns, I.S. Hughes, J.G. Lynch, D.J. Martin, R. O'Neill, C. Raine, J.M. Scarr, K. Smith[1], A.S. Thompson, J. Wells

Department of Physics and Astronomy, University of Glasgow, Glasgow G12 8QQ, United Kingdom[24]

B. Brandl, O. Braun, R. Geiges, C. Geweniger[1], P. Hanke, V. Hepp, W. Heyde, E.E. Kluge, J. Krause, Y. Maumary, M. Panter, A. Putzer, B. Rensch, K. Schmitt, A. Stahl, K. Tittel, M. Wunsch

Institut für Hochenergiephysik, Universität Heidelberg, 6900 Heidelberg Fed. Rep. Germany[30]

G.J. Barber, A.T. Belk, R. Beuselinck, D.M. Binnie, W. Cameron[1], M. Cattaneo, P.J. Dornan, S. Dugeay, R.W. Forty, D.N. Gentry, A.P. Heinson, M. MacDermott, D.G. Miller, D.R. Price, J.K. Sedgbeer, G. Taylor, A.P. White

Department of Physics, Imperial College, London SW7 2BZ, United Kingdom[24]

P. Girtler, D. Kuhn, G. Rudolph

Institut für Experimentalphysik, Universität Innsbruck, 6020 Innsbruck, Austria[32]

C.K. Bowdery[1], T.J. Brodbeck, A.J. Finch, F. Foster, G. Hughes, N.R. Keemer, M. Nuttall, B.S. Rowlingson, T. Sloan, S.W. Snow

Department of Physics, University of Lancaster, Lancaster LA1 4YB, United Kingdom[24]

T. Barczewski, L.A.T. Bauerdick, K. Kleinknecht[1], D. Pollmann[9], B. Renk, S. Roehn, M. Schmelling, K. Schmitz, F. Steeg

Institut für Physik, Universität Mainz, 6500 Mainz, Fed. Rep. of Germany[30]

J-P. Albanese, J-J. Aubert, G. Barrand[8], R. Bazzoli, C. Benchouk, A. Bonissent, A. Ealet-Grousset, F. Etienne, Y. Gally, E. Kajfasz, R. Nacasch, P. Payre, B. Pietrzyk[1], J. Raguet, Z. Qian

Centre de Physique des Particules, Faculté des Sciences de Luminy, IN^{2}P^3-CNRS, 13288 Marseille, France

H. Becker[10], W. Blum, P. Cattaneo, M. Comin, G. Cowan, B. Dehning, H. Dietl, M. Fernandez-Bosman, D. Hauff, A. Jahn, E. Lange, G. Lütjens, G. Lutz, W. Männer, H-G. Moser, Y. Pan, R. Richter, A.S. Schwarz, R. Settles, U. Stiegler, U. Stierlin, G. Stimpfl[11], J. Thomas, G. Waltermann

Max-Planck-Institut für Physik und Astrophysik, Werner-Heisenberg-Institut für Physik, 8000 München, Fed. Rep. Germany[30]

G. Aioun, J.N. Albert, Ch. Arnault, G. de Bouard, J. Boucrot, O. Callot, R. Chase, A. Cordier, M. Davier, M. Dialinas, A. Ducorps, D. Fournier, G. Ganis, J.-F. Grivaz, Ph. Heusse, P. Janot, P. Jean, V. Journé, D.W. Kim, J. Lefrançois, D. Lloyd-Owen, A.-M. Lutz, P. Marotte, J.-J. Veillet, F. Zomer

Laboratoire de l'Accéléateur Linéaire, Université de Paris-Sud, IN^{2}P^3-CNRS, 91405 Orsay Cedex, France

S.R. Amendolia, G. Bagliesi, G. Batignani, A. Bechini, F. Bosi, L. Bosisio, U. Bottigli, C. Bradaschia, I. Ferrante, F. Fidecaro, L. Foà[1], E. Focardi, F. Forti, S. Galeotti, A. Giassi, M.A. Giorgi, F. Ligabue, A. Lusiani, E.B. Mannelli, P.S. Marrocchesi, A. Messineo, F. Palla, D. Passuello, G. Sanguinetti, S. Scapellato, J. Steinberger, R. Tenchini, G. Tonelli, G. Triggiani

Dipartimento di Fisica dell'Università, INFN Sezione di Pisa, e Scuola Normale Superiore,56010 Pisa, Italy

J.M. Carter, B.J. Green, M.G. Green, A.K. McKemey, P.V. March, T. Medcalf, M.R. Saich, N.M. Stewart, J.A. Strong[1], R.M. Thomas, T. Wildish

Department of Physics, Royal Holloway & Bedford New College, University of London, Surrey TW20 OEX, United Kingdom[24]

E.H.Bellamy[13], J. Bizzell, D.R. Botterill, R.W. Clifft, I.F. Corbett, T.R. Edgecock, M. Edwards, S.M. Fisher, J. Harvey, D.L. Hill, E. Holtom, T.J. Jones, S. Madani Bozorg, G. McPherson, D.R. Moore, M. Morrissey, A. Nichols, P.R. Norton, D.P. Salmon, G.J. Tappern, J.C. Thompson, A. Tucker

High-Energy Physics Division, Rutherford Appleton Laboratory, Chilton, Didcot, OXON OX11 OQX, United Kingdom[24]

R. Bernard, B. Bloch-Devaux, H. Desportes, J. Heitzmann, M. Jacquemet, A. Joudon, E. Locci, J.C. Lottin, S. Loucatos, P. Micolon, J. Pascual, B. Pignard, J. Rander, J.-F. Renardy, A. Roussarie, J.-P. Schuller, R. Turlay

Département de Physique des Particules Élémentaires, CEN-Saclay, 91191 Gif-sur-Yvette Cedex, France[31]

J.G. Ashman, C.N. Booth, C. Buttar, R. Carney, S.L. Cartwright, F. Combley, M. Dinsdale, M. Dogru, F. Hatfield, J. Martin, D. Parker, P. Reeves, L.F. Thompson

Department of Physics, University of Sheffield, Sheffield S3 7RH, United Kingdom[24]

S. Brandt, H. Burkhardt, G. Gillessen, C. Grupen, H. Meinhard, E. Neugebauer, M. Olpp, W.U. Otto, M. Roschangar, U. Schäfer, R. Seibert, H. Seywerd, K. Stupperich, L. Wurmbach

Fachbereich Physik, Universität Siegen, 5900 Siegen, Fed. Rep. Germany[30]

B. Gobbo, F. Liello, A. Mansutti, E. Milotti, F. Ragusa[12], L. Rolandi[1]

Dipartimento di Fisica, Università di Trieste e INFN Sezione di Trieste, 34127 Trieste, Italy

L. Bellantoni, J.F. Boudreau, A. Caldwell[14], D. Cinabro, M. Convery[15], J.S. Conway, D.F. Cowen, Z. Feng, J.L. Harton, J. Hilgart, J. Izen[16], R.C. Jared[17], R.P. Johnson, B.W. LeClaire, T.C. Meyer[1], D. Muller[18], Y.B. Pan, T. Parker, J.R. Pater, S. Ritz[14], Y. Saadi, V. Sharma, D. Strom[19], J.A. Wear, F.V. Weber, E. Wicklund[20], Sau Lan Wu, S.T. Xue, G. Zobernig

Department of Physics, University of Wisconsin, Madison, WI 53706, USA [25]

---

[1] Now at CERN.
[2] Permanent address: DESY, Hamburg, Fed. Rep. Germany.
[3] Now at LeCroy, Geneva,Switzerland.
[4] On leave of absence from University of Washington, Seattle, WA 98195,USA
[5] Also Centre de Physique des Particules, Faculté des Sciences, Marseille, France
[6] Also *Istituto di Fisica Generale*, Università di Torino, Torino, Italy.
[7] Also Istituto di Cosmo-Geofisica del C.N.R, Torino, Italy.
[8] Now at LAL, Université de Paris-Sud, Orsay, France.
[9] Permanent address: Institut für Physik, Universität Dortmund, Fed. Rep. Germany.
[10] Permanent address: Gesamthochschule,Saarbrücken, Fed. Rep. Germany.
[11] Now at FSU, Florida, USA.
[12] Now at INFN Milano, Italy.
[13] Formerly at *Westfield College, University of* London,UK
[14] Now at Columbia University,NY,USA.
[15] Now at Princeton University,NJ,USA.
[16] Now at University of Illinois, Urbana-Champaign,Ill.,USA
[17] Permanent address: LBL, CA, USA.
[18] Now at SLAC,CA,USA.
[19] Now at University of Chicago,Ill.,USA.
[20] Now at California *Institut of* Technology,CA,USA.
[21] Supported by CAICYT, Spain.
[22] Supported by National Science Foundation of China.
[23] Supported by the Danish Natural Science Research Council.
[24] Supported by the UK Science and Engineering Research Council.
[25] Supported by the US Department of Energy, contract DE-AC02-76ER00881.
[26] Supported by the US Department of Energy, contract DE-FG05-87ER40319.
[27] Supported by the NSF, contract PHY-8451274.
[28] Supported by the US Department of Energy, contract DE-FC0S-85ER250000.
[29] Supported by SLOAN fellowship, contract BR 2703.
[30] Supported by the Bundesministerium für Forschung und Technologie, Fed. Rep. Germany.
[31] Supported by the Institut de Recherche Fondamentale du C.E.A.,France.
[32] Supported by Fonds zur Förderung der wissenschaftlichen Forschung, Austria.
[33] Deceased.

CONTENTS

1. INTRODUCTION

The detector described in this paper (ALEPH: 'A detector for LEP PHysics') has been constructed for experiments using the new accelerator at the European Organization for Nuclear Research (CERN), the Large Electron–Positron storage ring (LEP). This machine, in its first stage, is able to accelerate, store, and collide electrons and positrons up to a beam energy of 55 GeV. At the centre-of-mass energy of 90 GeV, LEP produces Z^0 bosons with an expected luminosity of the order of 10^{31} cm^{-2} s^{-1}. At a later stage, an increase of the c.m. energy up to 200 GeV is planned. The detector has been designed to study in detail the parameters of the standard electroweak model, such as the production and the decay modes of the Z^0 and $W^{\pm}$ bosons, to test QCD at large Q^2, to investigate neutral-current couplings of the different quarks and leptons, and to search for the top quark. In addition, it will allow the search for new phenomena, such as the Higgs bosons or supersymmetric particles.

Typical events are complex, with 20 charged particles on average plus a similar number of neutrals, distributed over the entire solid angle. The expected event rate is very low, especially at energies above the Z^0 pole. Therefore, this detector was conceived to cover as much of the total solid angle as practically possible and to collect from each event a maximum amount of information. Of fundamental importance for this purpose are the track detector and high magnetic field, designed to permit precise momentum measurement of the charged particles, and the electron–photon calorimeter surrounding it, designed to achieve high spatial resolution and electron identification.

2. GENERAL LAYOUT

The overall detector layout is shown in fig. 1; two sections through the centre of the detector, one containing the beam line and one perpendicular to the beam, are given in figs. 2 and 3. The components of the detector will be described in the following sections. The superconducting solenoid (section 3), 5.3 m in diameter and 6.4 m long, produces an axial magnetic field of 1.5 T. The central tracking chambers (section 4) measure emission angle and curvature of charged particle trajectories. The small inner tracking chamber (ITC) using axial wires is a drift chamber with inner and outer radii of 13 cm and 29 cm, respectively, and a length of 2 m. It provides up to eight coordinates per track in the plane perpendicular to the magnetic field, with an accuracy of 100 μm, and a trigger signal for charged particles coming from the interaction region. The large cylindrical time projection chamber (TPC), 4.4 m long and 3.6 m in diameter, provides a three-dimensional measurement of each track segment and yields a measurement of transverse particle momenta p_T with an accuracy of $\Delta p_T/p_T^2 \approx 10^{-3}$ (GeV/c)$^{-1}$ if it is used together with the ITC. The chamber also contributes to particle identification through measurements of energy loss (dE/dx) derived from about 340 samples of the ionization for a track traversing the full radial range. Beyond the TPC, but still inside the coil, is the electromagnetic calorimeter (section 5), consisting of alternating layers of lead sheets and proportional tubes read out in 73,728 projective towers, each subdivided into three depth zones. Outside the coil, the hadron calorimeter (section 6) consists of limited-streamer tubes interleaved with the iron plates forming the magnet return yoke, the total iron thickness being 1.2 m. This calorimeter is read out in 4608 projective towers, and the tubes also give a digital output for tracking penetrating muons. The muon positions and angles are also measured outside the calorimeter in two double layers of limited-streamer tubes, separated by 50 cm.

The electron–positron interactions take place inside the beam pipe, which has a diameter of 156 mm and a thickness of 0.5 mm, made of an aluminium (96%)–magnesium (3.2%) alloy. Around the beam pipe, a double-layer silicon strip detector will be inserted in order to improve the vertex resolution.

For an absolute measurement of the luminosity, two detectors for small-angle Bhabha scattering are installed around the beam pipe (section 7).

3. MAGNET

The magnet consists of a fully calorimetrized iron yoke and a superconducting solenoid producing a homogeneous field of 1.5 T parallel to the LEP beam direction and corresponding in uniformity to the requirements of the time projection chamber (TPC) track detector, i.e. less than 0.2 mm sagitta distortions. The useful magnetic volume is 123 m^3, the magnetic stored energy 130×10^6 J.

3.1 The iron yoke

This iron structure has three parts: the central part, called the barrel, having a mass of 1680 t and the two end-caps each having a mass of 450 t. The iron yoke serves four different functions: it shapes the longitudinal magnetic field; it serves as a sampling medium for the hadron calorimeter; by absorbing hadrons, it helps to identify muons penetrating the yoke; and it is used as a support for most of the other subdetectors. Design criteria were: i) axial symmetry in order to avoid azimuthal field components; ii) modular structure; a maximum weight of 80 t for a module was permitted by the crane in the pit; iii) dead-space minimization. The barrel has the shape of a hollow dodecagonal cylinder, 7.24 m long and 9.37 m wide. It is made of 22 layers of steel plates, 50 mm thick, and one 100 mm thick plate on the outside, with 22 mm spacing for the streamer tubes. The end-caps are short (1.18 m) dodecagonal cylinders, 8.7 m wide. They have central holes of 90 cm diameter to permit them to be rolled back along the beam line while the LEP low-beta quadrupoles remain in position. At nominal field, the end-caps are pushed against the barrel by magnetic forces of about 4000 t. The maximum deformation of the plates is less than 3 mm.

3.2 Superconducting coil

The solenoid has been designed so that, together with the iron yoke, it provides a magnetic field of 1.5 T in the central detector with the appropriate field uniformity.

The solenoid is suspended at both ends from the barrel part of the magnet iron yoke, and carries the weight of the electromagnetic calorimeter and central detector (the TPC), which are attached to longitudinal rails fixed on the inner wall of the vacuum chamber which encases the solenoid. The total weight of these detectors is ~ 130 t.

The field requirement can be expressed as a tolerance of the integral of the radial field component B_r along z in the whole volume of the TPC, which is 4.4 m long and 3.6 m in diameter. This tolerance is defined as

$$\int_0^{2200} (B_r/B_z)\, dz < 2 \text{ mm},$$

where B_z is the main field component.

The configuration consists of a main solenoid, made of a continuous and homogeneous winding extending over the whole length of 6.35 m available between the two end-caps, and of two compensating coils located at the ends of the main solenoid, each 40 cm long. The main characteristics of the solenoid are given in table 1. Because of its smaller density and larger radiation length, aluminium of high purity is used as a stabilizer for the NbTi superconductor. A more complete description can be found in refs. [1] and [2].

3.3 Magnetic-field measurement

The whole magnet with coil and yoke was assembled on the surface before completion of the experimental hall. In this configuration, the magnetic field inside the coil was measured in the autumn of 1987 with a gear consisting of two sets of Hall plates mounted on two radial arms which could be rotated around the cylinder axis and moved in the axial direction. The Hall plates were

mounted at 20 radial positions (r in cylindrical coordinates between 32.6 cm and 232.5 cm), and the whole arm was moved to 25 axial positions in the range of $z = \pm 2.6$ m and 35 equispaced positions in azimuthal angle ϕ. Measurements at ϕ and $\phi + 180°$ were taken at the same time. The Hall probes were oriented such as to measure the main field component B_z, the radial field component B_r, and the azimuthal field component B_ϕ. Three nuclear magnetic resonance (NMR) probes on one side of the measuring arm, together with one reference probe at the centre of the coil, were used for normalization purposes. A map of the whole volume consisted of field values at some 900 points.

The axis of the gear was aligned with the cryostat to a precision of 0.5 mm in radius and 0.3 mrad in angle. The axial and azimuthal positioning accuracies of the gear were $\delta z = 0.2$ mm and $\delta\phi = 1$ mrad, respectively.

The overall sensitivity of the Hall-plate measurements was equivalent to $\delta B \approx 0.1$ G. The repeated opening and closing of the end-caps did not produce any significant change in the field distribution.

The main component B_z of the field was optimized by adjusting the current in the two compensating coils until its value at points on the axis was constant. A plot of B_z versus z is shown in fig. 4, and the measured value of $\Delta B_z/B_z$ is constant within 0.2%.

The main component is a function of azimuthal position with variations of up to $\delta B_z/B_z = 5 \times 10^{-4}$ at $r = 1.7$ m produced by local differences in the magnetic reluctance of the end-cap modules, as well as by minor imperfections in the main coil.

Values of the radial component B_r are shown in fig. 5 together with the line integral $\int (B_r/B_z)\,dz$ in the TPC volume, at four different azimuthal positions, with optimized currents in the compensating coils. This integral, which after weighting by $1/\omega\tau \approx 1/8$ determines the sagitta distortions in the TPC, is slightly larger than expected from the calculations, reaching ~ 1.5 mm in the worst case. Here also the azimuthal variations reflect the non-uniformities in the reluctance of the end-cap modules.

The line integral of the azimuthal component is shown in fig. 6. This integral, which contributes directly to the sagitta distortions in the TPC, also shows variations due to local differences in reluctance mentioned above.

In summary, these field maps [3] show that the main field component is uniform to the level of 0.2% and reproducible. The transverse field components show variations in radius and azimuth of a magnitude such that sagitta distortions in the TPC are less than 0.2 mm and can be corrected for.

4. CENTRAL TRACKING CHAMBERS

4.1 Inner tracking chamber (ITC)

4.1.1 Overall description

The ITC is a cylindrical multiwire drift chamber serving a dual purpose in ALEPH. It provides up to eight accurate r–ϕ points for tracking in the radial region between 160 and 260 mm, and it also provides the only tracking information for the Level-1 trigger. The wires run parallel to the z (beam) direction, so the r–ϕ coordinate is obtained by measuring the drift time, giving a precision of about 100 μm. The z-coordinate is found with a precision of about 3 cm by measuring the difference in the arrival times of pulses at the two ends of each sense wire. For the trigger, the ITC has two asssociated processors that find, respectively, charged-particle trajectories either in two dimensions (the r–ϕ projection) or in three dimensions. The trigger is available within 2–3 μs of a beam crossing.

4.1.2 Mechanics

The basic mechanical construction of the ITC is shown in fig. 7; it is described in more detail elsewhere [4]. The active volume is a cylinder of 2 m length and 570 mm diameter. A total of 960

sense wires are strung in 8 concentric layers (96 wires in each of the 4 inner layers, and 144 wires in each of the 4 outer layers), between two Al end-plates.

The load of the wires is borne by a 2 mm thick carbon-fibre tube (570 mm inner diameter), which defines the outer surface of the chamber. The inner surface is defined by a polystyrene 'low-mass' tube, of 2 mm thickness and 256 mm inner diameter. The inner and outer surfaces of both tubes are coated with thin (25 μm) layers of Al foil. Inside the low-mass tube, there is a 100 μm thick Mylar sheet to protect the polystyrene during installation of the minivertex detector.

High-voltage distribution boxes are mounted on the outside of the Al end-plates. An electrical end-flange, 20 cm from the end-plates, supports these distribution boxes and connects them to the preamplifiers on the outer side. The ITC is supported from the TPC end-plates by a cylindrical Al can, which slides over the cables and is also bolted to the electrical end-flange. The mechanical parameters of the chamber are given in table 2.

The drift cells of the ITC are hexagonal, with a central sense wire surrounded by six field wires. Four of these field wires are shared by neighbouring cells in the same layer (fig. 8). The sense wires are operated at a positive potential in the range 1.8–2.5 kV. The field wires are held at earth potential: one field wire per cell is insulated from the end-plate by a small feedthrough, and can be used to inject a calibration pulse into the chamber. The other field wires are in electrical contact with the end-plates.

The cell sizes were kept small because of the need to reach a rapid trigger decision (whose speed is determined partly by the maximum drift time). There are 96 cells in each of the 4 inner layers, and 144 cells in each of the 4 outer layers. This means that the cells in the fourth layer have the longest maximum drift distance (6.5 mm), those in the fifth layer the shortest distance (4.7 mm).

The drift cells are 'close-packed', i.e. cells in contiguous layers are offset by half a cell width, which helps resolve the left–right ambiguity in the track fitting and enables adequate two-track resolution to be achieved with single-hit electronics. Pairs of drift-cell layers (double layers) are separated by a layer of guard wires (96 wires between layers 2 and 3, 96 between layers 4 and 5, and 144 between layers 6 and 7).

The Al coating of the carbon-fibre outer tube and the polystyrene inner tube provides electrical screening from RF interference, and forms equipotential surfaces at the boundaries of the chamber, thus improving the uniformity of the electric field in the chamber.

4.1.3 Gas system

The ITC is operated with a mixture of either Ar(50%) + C_2H_6(50%) or Ar(80%) + CO_2(20%) at atmospheric pressure. For the Ar–C_2H_6 mixture, the gas gain was measured to be 1.9×10^4 at 2.1 kV, rising to 5.2×10^4 at 2.3 kV. The plateau in the detection efficiency is reached at 2.0 kV. The operating voltage is chosen between 2.2 kV and 2.4 kV.

For the Ar–CO_2 mixture the gas gain was 1.2×10^4 at 1.8 kV and 4.9×10^4 at 2.0 kV. The plateau is 200 V wide and is reached at 1.85 kV. The operating voltage is chosen between 1.85 kV and 2.05 kV.

4.1.4 Electronics

The signal wires of the ITC are connected to preamplifiers with a voltage gain of 3, which are mounted on the chamber using boards with circuits for 2 × 8 wires. The signals are then taken to the central boards (AZ boards) containing the main amplifiers, discriminators, latches and time-expansion circuits, via a 50 Ω cable. The incoming signals are amplified by a factor of about 36 and then discriminated at a constant fraction threshold. The discriminator outputs from one end of the chamber are routed via an auxiliary backplane connection to the drift-time CAMAC time-to-digital converters (TDCs) with 0.5 ns resolution.

The gated digital signals derived from one end of the chamber (the start end) are used to switch on an accurately controlled charging current to a capacitor. This current is stopped by the arrival of the signal from the other (stop) end of the chamber; this has been delayed by about 50 ns to ensure that i) the Stop arrives after the Start, and ii) non-linearities in the system, immediately after the arrival of a Start signal, may be disregarded. During the Enable Start-Stop gating period, a second current is also discharging the capacitor at a rate that depends on the wire layer radius. The ratio of the charging to discharging currents is the 'time-expansion factor'. A comparator produces a signal when the voltage on the capacitor returns to zero. The time of this is proportional to the charge deposited and hence to the z-position of the pulse on the wire. The length of this pulse can be adjusted to reflect the accuracy of the z determination before being routed, via an auxiliary backplane connection, to the r-ϕ-z space-point processor. It is the coincidence between the selected patterns of these signals from wires in different layers that chooses genuine tracks in three dimensions.

Four digital-to-analog converters (DACs) configured as two pairs (coarse and fine) control the operation of the time-expansion circuit for every channel. The first pair determines the starting voltage on the capacitor and allows a timing offset for each channel. The second pair controls the magnitude of the charging current and thus permits small variations in the slope of the z versus expanded-time relationship. The time-expanded pulses are routed to FASTBUS TDCs for off-line space-point reconstruction.

4.1.5 Trigger processors

From the AZ boards, two signals are provided for each wire; these signals can be used by the trigger processors. The first, a hit wire latch, is used to search for tracks in radial patterns of wire cells in the r-ϕ projection. The second is a pulsed output, the arrival time and duration of which represent, respectively, the z-position of the hit and its expected error. This second signal is used to find tracks in space by means of the coincidence circuits of the r-ϕ-z space-point processor. Both these processors are implemented in FASTBUS Slave modules. Special bits relating to the number of hits per layer and to the number of tracks are generated only in the r-ϕ processors and are always output. The trigger signal produced is available to the ALEPH Level-1 trigger processor in less than 3 μs.

4.1.6 Chamber performance

The chamber was tested in a charged particle beam with the Ar-C_2H_6 gas mixture. The following results were obtained:

i) Drift-time relation: The relation between drift time and drift distance was found to deviate slightly from the linear behaviour, with a mean drift velocity across the cell of 50 μm/ns. This relation was parametrized using a third-order polynomial.

ii) Efficiency: The detection efficiency of a layer of sense wires is defined as the percentage of hits on these wires lying within 3σ of a track crossing the layer but fitted without these hits. The test-beam data show that the r-ϕ efficiency is 98.2% at a sense-wire voltage of 2.3 kV and 98.0% at 2.2 kV, independent of the distance from the sense wire. The z-efficiency is much more voltage-dependent, and is highest for the innermost layers. At 2.3 kV it ranges between 95.6% and 97.6%, whilst at 2.2 kV it is in the range 86.3% to 97.9%.

iii) Resolution: The resolution of the ITC, as measured in the test beam, varies as a function of distance from a wire in r-ϕ (fig. 9) and of distance along a wire in z. The mean values are approximately 100 μm in r-ϕ and 3 cm in z.

4.2 The time projection chamber (TPC)

4.2.1 Design considerations

The central track detector of ALEPH is a very large three-dimensional imaging drift chamber, a TPC. It is a cylinder with axial parallel magnetic and electric fields (fig. 10). The electric drift field points from each end-plate towards the central membrane that divides the chamber into two halves. The electrons produced by the ionization of traversing charged particles drift towards one end-plate, where they induce ionization avalanches in a plane of wire chambers. These are detected and yield the impact point and the arrival time of the drifted electrons. There are 18 wire chambers ('sectors') in each end-plate.

The TPC is used to measure the momentum and emission angle of charged tracks with good resolution, and to determine the ionization density dE/dx, used for the separation of electron and pion tracks. Pattern recognition is particularly simple in this chamber because it provides three-dimensional coordinates rather than projections.

The z-coordinate is obtained from the drift time and the known drift velocity field. The rϕ-coordinate is calculated by interpolating the signals induced on cathode pads precisely located on the sectors, the r-coordinate is given by the radial position of the pads involved in the measurement. The TPC measures 21 three-dimensional points for each track traversing the inner and the outer field cages.

The trajectory of a charged particle inside the TPC is a helix, and its projection onto the end-plate is an arc of a circle. Measurement of the sagitta of this arc yields the curvature radius which is proportional to the modulus of the component of the momentum perpendicular to $\vec{B}$.

The resolution Δp_T in transverse momentum p_T (GeV/c) is proportional to the resolution in the measurement of the sagitta Δs (mm):

$$\frac{\Delta p_T}{p_T} = 0.027 p_T \frac{\Delta s}{\ell^2 B} \quad , \tag{1}$$

where B (T) is the modulus of the magnetic field and ℓ (m) is the length of the projected trajectory. With the lever arm of $\ell = 1.4$ m, a sagitta error of 100 μm corresponds to a 10% resolution in transverse momentum for the highest possible momenta, i.e. muon pairs produced at a c.m. energy of 200 GeV.

4.2.2 Mechanical construction

The main components of the TPC structure are the inner and outer field cages, the two end-plates, and the four fixtures on each end-plate (fig. 10). These elements define the mechanical positions of the wire chambers. The tolerances within each end-plate are 50 μm, while that for the relative position of one end-plate with respect to the other is 0.5 mm and that for the relative position of the TPC with respect to the other detectors in ALEPH is 1 mm. These latter two are defined by optical alignment with a precision of ± 0.2 mm. The main mechanical parameters of the TPC are listed in table 3.

a) Field cage

The electrical drift field is shaped by two coaxial cylinders, by the central membrane held at negative high voltage, and by the proportional wire chambers at ground potential. The cylinders, which have diameters of 3.6 m and 0.6 m, and a length of 4.4 m, are covered with electrodes at potentials which ensure that the drift field in the volume between them is constant and parallel to the axis. The electrodes are made of copper bands with a pitch of 10.16 mm, separated by gaps of 1.5 mm. Two layers of bands (35 μm thick for the outer cylinder, and 19 μm for the inner one) are

laid on both sides of a 75 μm Kapton sheet (fig. 11). The two layers are staggered in order to shield the TPC volume from the high fields in the insulator, consisting of Mylar foils. These are wound helically and glued together with a polyurethane glue.

The electrodes and insulator are supported by aluminium structural skins separated by an aluminium honeycomb spacer. The total material thickness corresponds to $0.023X_0$ in the inner cylinder, and $0.048X_0$ in the outer one.

The central membrane is made from 25 μm Mylar coated on both sides with a conducting graphite paint. The Mylar sheet is reinforced at its outer and inner periphery by two rings of 0.3 mm thick Mylar. The whole sheet is stretched and its tension is supported by a 10×8 mm^2 Al ring, which fits into a shallow U-section Al ring, glued onto the outer field cage.

The drift field of about 115 V/cm is generated by a high voltage of -27 kV on the central membrane. The electrode rings are connected in series using 1 MΩ resistors. The resistors were measured and paired so as to obtain a value of 2.004 MΩ ($\pm 0.2\%$) between adjacent electrodes. Four resistor chains connect the central membrane with the last electrodes at -65 V potential, drawing a total current of 4×60 μA.

b) Gas system [5]

The gas in the TPC volume is Ar (91%) + CH_4 (9%) at atmospheric pressure. This is a non-flammable mixture. In order to ensure the required high long-term stability in the mixing ratio, and with it the uniformity of TPC performance (drift velocity, gas gain), the gas is pre-mixed into a large buffer volume which can hold 900 m^3 of gas.

Extreme care has been taken to minimize the signal attenuation due to electronegative impurities in the drift space. Only materials that had been controlled to be non-contaminating were accepted for the construction of the TPC and for the gas system components.

The gas supplied from the buffer volume to the TPC has an O_2 content below 3 ppm, an H_2O content below 5 ppm; the loss of ionization by electron attachment is less than 0.5% in 1 m of drift. For a fresh-gas flow that corresponds to about one TPC volume change per week, and without purification, the gas leaving the TPC has typically an O_2 content of less than 20 ppm and an H_2O content of about 20–40 ppm; the signal loss is less than 1.5% per metre of drift.

The TPC volume is held at 8–12 mbar above atmospheric pressure and follows the atmospheric pressure variations. The temperature of the gas flowing into the TPC is maintained at (21.0 ± 0.5)°C.

c) Wire chamber sectors

The large diameter of the TPC, required by the magnetic bending power necessary for precise momentum measurement, results in a large number of end-plate sectors, 18 on each side. The 'zigzag' geometry shown in figs. 12 ensures a minimum loss of lever arm when the track crosses the boundaries between chambers. In one end-plate, there are 6 sectors labelled K (Kind) inside and a ring of 12 alternating sectors labelled M (Mann) and W (Weib) outside. Figure 13 gives details of the mechanical design of a K sector. There are three planes of wires strung on each chamber; in sequence they have the function of gating grid, cathode plane, and sense-wire plane, interleaved with field-shaping wires. Properties of the wire grids are listed in table 4, and fig. 14 shows a perspective view of them.

The relative positions of the wires in the r–ϕ plane within the sense/field grid are accurate to ± 0.02 mm. The overall positions in the r–ϕ plane of the three grids relative to the reference marks on the pad plane are good to better than ± 0.1 mm. The mechanical tolerances of the wire planes and of the sense-wire diameter (0.5%) were chosen such that any individual tolerance would not cause more than about $\pm 1\%$ change in gas amplification.

The ionization avalanches created around the sense wires are read out by the signal induced on cathode pads at a distance of 4 mm from the sense wire. The arrangement of these long pads of size 6.2 mm × 30 mm [$\delta(r\cdot\phi) \times \delta r$] is shown in fig. 12b. The pad pitch in azimuth is 6.7 mm. The two pads at the sector edge of each pad row have 1/2 this pitch. A K sector has 9 pad rows and a total of 909 pads, a W sector has 12 pad rows and 1182 pads, and an M sector has 12 pad rows and 1326 pads, giving a grand total of 41004 pads for the whole TPC.

Between these pad rows there are long, circular 'trigger' pads from which ALEPH's second-level trigger is derived. The trigger pads are 6.3 mm in r and subtend 15° in ϕ, except for the outer 5 trigger pad rows (see fig. 12b), which are segmented again to reduce electronic noise. There are 32 trigger pads per sector.

The pads are milled onto a copper-clad glass-fibre-reinforced epoxy sheet which is glued to the drift-volume side of the Al sandwich. The pads are connected to the preamplifiers via wires passing through the Al sandwich structure. The preamplifiers are grouped in modules of 16 on boards which plug into the back of the sector. The pad positions have a tolerance of ± 20 μm relative to the reference marks on the chamber; their overall accuracy causes a maximum of ± 30 μm error on the sagitta measurement.

4.2.3 Electronics and readout

The readout system of the TPC is based on FASTBUS. It is subdivided into independent crate clusters, each of them serving one of the 36 TPC sectors. The number of main components in each of the three sector types is given in table 5. The architecture of the TPC readout system is shown in fig. 15, and the main properties of the electronics are summarized in table 6.

The pad and wire amplifiers on the sectors are mounted on printed boards in groups of 16. The preamplifier is a charge-integrating circuit with a decay-time constant of 2 μs, followed by symmetric cable drivers (see fig. 16). Pulses of typically ± 10 mV are transmitted on a twisted-pair cable to a pulse-shaping amplifier and a flash analog-to-digital converter (FADC). Sixty-four channels are mounted on a FASTBUS module (TPD: time projection digitizer), with buffers for 4 events. The 8-bit FADC (Thomson TS 8328P) digitizes the analog signal with an 11.4 MHz clock. To equalize the responses from the different channels (pedestal, gain, and linearity) the reference voltages of the FADC are controlled by four 6-bit digital-to-analog converters that are attached to the reference ladder at the 0%, 25%, 50%, and 100% taps. This 'electronic calibration' is done with a remotely controllable pulse-generator installed on each sector. The generator pulses the field wires. The signals induced on the pads and wires (inverted polarity) are received and transmitted in the same way as signals from particles. The generator is controlled by a special FASTBUS module, the STPC. The calibration program is running on a time-projection processor (TPP), a FASTBUS master designed using a Motorola 68020 chip. It has control over the STPC and calculates from the response of the channels the settings of the tap-points, which are needed to equalize and linearize the responses.

The readout of the TPDs is controlled by a TPP. A TPP controls several FASTBUS crates with TPDs, see table 5. Its tasks are: readout of TPDs and data formatting; reduction of wire data; monitoring of data and data transfer, error recording and error recovery; calibration and testing of the TPC electronics.

The data flow generated by the TPPs is transferred to an Event Builder (EB). The EB (also based on the Motorola 68020) is connected to the TPPs via a FASTBUS cable segment. The 36 TPPs of each end-cap are read out by one EB, whilst a third EB collects the data from these two end-cap EBs.

The tasks of the EB are to

- handle service requests from the TPPs, and do readout and formatting;
- monitor the evolution of data-taking;

For the purpose of calibration and checking, test pulses can be injected into the readout system under the control of the TPP. Such tests may consist of

- pulsing the field wires;
- pulsing the inputs of the preamplifiers via individual capacitors;
- pulsing all shaping amplifiers of a TPD.

The main characteristics of electronics and readout are summarized in table 6.

4.2.4 Gating

The operation of a TPC in a continuously sensitive mode is made difficult by the presence of space charges in the drift region [6]. These are positive ions produced in the Townsend avalanches near the sense wires, which then migrate towards the central high-voltage electrode. They can alter the drift field and cause track distortions. The ALEPH TPC therefore contains a gating wire grid (see figs. 13 and 14). This extra wire grid is installed between the shielding grid and the drift region (fig. 17). The gating grid is either in the 'open' state or the 'closed' state. In the open state (fig. 17a), the potential V_g ($\simeq -67$ V) is placed on the gate wires so that the gate is transparent to the passage of drifting charged particles. In the closed state (fig. 17b), the potentials $V_g \pm \Delta V_g$ are placed on alternate wires of the grid, so that the resulting dipole fields render the gate opaque to the passage of charged particles. A ΔV_g of $\approx$ 40 V suffices to block the passage of the positive ions [7] while, because of the magnetic field, a much bigger ΔV is required to also block the incoming electrons (see fig. 18). By using a ΔV_g of 150 V the closed gate becomes also quite opaque to electrons.

Switching between the closed and open state of the gate is done synchronously with the bunch crossing (BX). About 3 μs before the BX, the gate is opened to allow electrons to drift into the amplification region. Normally the gate is then closed when the first-level trigger is negative (about 5.5 μs after the BX). Only when the first-level trigger is positive is the gate held open for the maximum 45 μs drift time of the electrons in the TPC.

It has been shown [7–9] that even though this synchronous mode of operation leaves the gate open roughly 33% of the time, positive ions are still unable to penetrate into the drift volume. The gate remains effective because the positive ions do not drift very far during one 'open' period and can still be neutralized at the gating grid, after following a zigzag path during a succession of gating cycles.

4.2.5 Laser system for field calibration

The purpose of this system is to provide information on the distortion of particle tracks and to measure the vector of the drift velocity in the TPC. Laser tracks can be created repeatedly in the same place. Averaging over many shots thus effectively eliminates statistical fluctuations on the measurement and allows a detailed study of systematic effects. Thirty straight ionization tracks are created in the TPC by firing two ultraviolet (UV) lasers. The tracks are arranged to originate approximately from the interaction point. The measured curvature of these tracks is used to correct the sagitta of particle tracks; the drift velocity is determined from the reconstructed polar angles, the differences of which are known to 0.02°.

Tests have shown that it was always possible to produce these ionization tracks in the gas without especially adding any of the molecular vapours that are known [10] to make the ionization possible. We therefore rely on the contamination that is present in the gas provided.

The layout of the laser system is shown in fig. 19. Two lasers are situated in a stable position on a platform above the magnet. The lasers are frequency-quadrupled Nd-yag lasers emitting at 266 nm with an energy of 4 mJ per 5 ns pulse. The polarization is controlled by a half-wave plate. This element is mounted directly on the laser frame, together with a telescope that is used to create a waist

of the beam in the chamber in order to obtain a high yield and narrow beam. In the chamber, the transverse r.m.s. width of the beam is of the order of 1 mm.

The beam path from the top of ALEPH into the TPC (fig. 19) has a length of about 10 m. Before the beam reaches the splitter ring through one of the notches in the HCAL, it is deflected through 90° three times. It travels down to the splitter ring in tubes that have an inner diameter of 5 cm, but from there on, the aperture is reduced to roughly 15 mm. To maintain the path through these narrow openings the beam is actively steered onto precise sensors. This is achieved by one actuator for each half of the TPC, which adjusts under computer control all four degrees of freedom that define the position in space of a narrow light beam.

The laser beam then enters the splitter ring surrounding the vacuum pipe of ALEPH at a radius between 35 and 40 cm. The beam is split twice on its path inside the ring to create three axial rays of equal intensity at a radius of 36.8 cm. Each of these rays passes four semitransparent mirrors and one pentaprism that directs a fraction of the light towards the TPC volume, thus creating ionization tracks at polar angles of 18°, 30°, 39°, 67°, and 90°.

Figure 20 shows the distributing elements as they are glued on the inner field cage of the TPC. The double mirrors consist of two dielectric surfaces held between two ceramic plates. The first mirror is semitransparent and deflects a partial ray onto the second mirror, which finally directs the beam into the volume of the TPC. Likewise, the first reflecting surface of the pentaprism is partly transparent, with a wedge glued onto it, so that 2% of the incident light continues to travel in the axial direction. This beam is monitored by a position-sensitive diode incorporated into the splitter ring on the opposite end-plate. This diode is used for active steering of the beam.

Figure 21 shows an (rϕ) projection of ionization tracks due to the laser beams at six different ϕ angles.

4.2.6 Performance and tests

The performance of the ALEPH TPC as a track-measuring device has been studied extensively in a test model with 90 cm diameter and 130 cm drift length (TPC 90) [11]. It had a solenoidal magnetic field of up to 1.2 T and used the same type of wire chambers as in ALEPH.

a) The rϕ spatial resolution

The rϕ spatial resolution depends on several factors, such as the magnetic field and the angles of the track segment with respect to wires and pads. The resolution can be expressed as

$$\sigma^2 = \sigma_0^2 + \sigma_d^2 + \sigma_\alpha^2(\mathrm{tg}\,\alpha - \mathrm{tg}\,\psi)^2 \cos^2\alpha + \sigma_\beta^2 \mathrm{tg}^2\beta\,, \tag{2}$$

where the angles α, β, and ψ are shown in fig. 22 and the non-relevant $\cos\beta$ dependence has been neglected.

The angle β is zero for a high-momentum track coming from the origin (main vertex); α, the angle between the track and the wire, ranges from $-30°$ to 30° in the inner sectors and from $-15°$ to 15° in the outer ones; ψ is the Lorentz angle, whose tangent is proportional to the magnetic field. In our standard gas mixture, at a magnetic field of 1.5 T, ψ is 32° [12, 13].

The contribution due to diffusion, σ_d, is

$$\sigma_d^2 = \frac{2\ell D(0)}{vN_e} \frac{1}{1+\omega^2\tau^2} \approx \frac{(6\,\mathrm{mm})^2}{1+\omega^2\tau^2} \frac{\ell\,(\mathrm{m})}{N_e}\,, \tag{3}$$

where D(0) is the transverse single-electron diffusion coefficient at magnetic field zero, ℓ is the drift length in metres, N_e is the total number of electrons in the track segment, v is the drift velocity, and

$\omega\tau$ is a known function of the magnetic field [14]. Typical values of σ_d are: $\sigma_d^2 = (350\ \mu m)^2\ \ell$ (m) at B = 0 and $\sigma_d^2 = (50\ \mu m)^2\ \ell$ (m) at B = 1.5 T.

The contribution of the so-called 'angular wire effect' is

$$\sigma_\alpha^2 = \frac{d^2}{12 N_{eff}} \approx \frac{(1.15\ mm)^2}{N_{eff}}\ , \tag{4}$$

where d is the distance between two sense wires and N_{eff} is an effective number of electrons taking into account the effects of Landau fluctuations.

The value of σ_α has been measured in TPC 90 at 1.2 T and also at 1.5 T [13]. Typical expected values at a magnetic field B = 1.5 T are $\sigma_\alpha = 219\ \mu m$ at $\ell = 0.04$ m and $\sigma_\alpha = 126\ \mu m$ at $\ell = 2$ m.

The contribution of the so-called 'angular pad effect', σ_β, is large since it is proportional to the length h of the pad. However, it is important only for track segments that are not parallel to the radius of the TPC, i.e. low-momentum tracks:

$$\sigma_\beta^2 = \frac{h^2}{12\ N_{eff}} \approx \frac{(8.66\ mm)^2}{N_{eff}}\ . \tag{5}$$

In TPC 90, the measured value is $\sigma_\beta = 2.5$ mm, for the same pad geometry.

The value of σ_0 includes the contributions due to electronic noise, digitization, and errors in the calibration. We have measured $\sigma_0 \leqslant 80\ \mu m$.

Table 7 quotes the values of σ from eq. (1) for a high-momentum track ($\tan\beta = 0$) for different values of ℓ and α. The contribution of the angular pad effect ($\tan\beta \neq 0$) is 25 μm for 20 GeV/c and 280 μm for 2 GeV/c.

b) Momentum resolution

The error of the transverse momentum of a track with 21 measured TPC coordinates is given by the formula

$$\frac{\Delta p}{p} \approx 10^{-3} p\ (GeV/c) \left(\frac{\langle\sigma\rangle}{150\ \mu m}\right) \left(\frac{1.5\ T}{B}\right) \oplus 0.003\ , \tag{6}$$

where p is the transverse momentum and $\langle\sigma\rangle$ is the average error on each coordinate. The last term is the contribution of the multiple scattering in the gas of the chamber, which has to be added in quadrature ($\oplus$).

Since the error on the measurement of the polar angle is small, the relative error on the momentum coincides with the relative error on the transverse momentum. Owing to the angular pad effect, $\langle\sigma\rangle$ increases at low momenta and there is a deterioration of the resolution.

In spite of the fact that the spatial resolution of a single measurement depends on α, the momentum resolution as a function of the azimuthal angle is roughly constant ($\pm 20\%$) because of a compensation of the α dependence from the inner to the outer sectors. The effect of the dead regions between the sectors is also modest. It is important only when the track crosses the boundary between two inner sectors. In that case the measured track length is halved and the momentum resolution is worse by a factor of about 4. This happens in a ϕ region of about 2.3° for each of the six boundaries, about 4% of the full azimuthal angle in total.

The error of the transverse momentum depends on the polar angle, since a track at large $|\cos\theta|$ is measured with less points and with a smaller lever arm. The effect of polar angle can be expressed as a function of $\cos\theta$ which multiplies the above expression, i.e.

$$\frac{\Delta p}{p}(p, B, \sigma, \cos\theta) = \frac{\Delta p}{p}(p, B, \sigma) \times f(\cos\theta)\,, \qquad (7)$$

where the function f depends on how many pad rows have measured the track and is shown in fig. 23, assuming that the momentum is measured only with TPC coordinates.

c) Spatial resolution in z

The resolution in z has been measured in TPC 90 as a function of the drift length from the straightness of reconstructed cosmic-ray trajectories in the r–z plane (parallel to the magnetic fields).

The drift-time measurement has a systematic contribution from the transit time of the electronics, the different length of the cables, and the shaping time of the electronics. These effects largely dominate the z-resolution, which does not show an important dependence on diffusion. Using the pad information, we have found $\sigma_z \approx 1$ mm for a track with a polar angle around 90°. This is worse by about a factor of 2 for tracks at polar angles around 20° or 160° where the signal on the long pads is very long in time.

The z-coordinate is also measured using the wires. This can be done when there is no confusion due to another track intersecting that particular wire at almost the same time. The space resolution achieved with each wire measurement is about 2.0 mm, weakly depending on the polar angle (see table 8).

d) Systematic effects on the track reconstruction

The space measurements made with each sector are converted to the global TPC coordinate system, using the position of each sector which is known with sufficient precision not to deteriorate the momentum resolution.

Electric and magnetic field inhomogeneities displace the trajectories of the drifting electrons, causing systematic errors on the reconstructed track. Global non-linear distortions that add to the momentum resolution are corrected by measuring the deviation from straightness of the 30 reconstructed laser beam tracks of the calibration system. The remaining systematic error on the sagitta should be small compared with the statistical contribution.

Linear distortions, such as those coming from the unknown small angle between the axes of the electric and the magnetic field, are measured with cosmic muons within the alignment procedure between TPC and ITC. These linear distortions do not influence the momentum resolution when it is measured only with TPC coordinates.

e) Two-track confusion

Two tracks are confused if they are close in both the rϕ and the z dimensions. Since the typical total width of the signal of a radial track parallel to the end-plate is about 1.5 cm in rϕ and 2 cm in z, two tracks are separated if they are more distant than the quoted distance in at least one dimension. Even if they are closer, the information can often be recovered by using specific algorithms.

f) dE/dx resolution

A dE/dx resolution of 9% has been measured in TPC 90 with an average radial track length of 40 cm. This value can be extrapolated to a track length of 140 cm giving a dE/dx resolution of less than 5% corresponding to the full TPC. The actual resolution can be obtained from Z^0 decays measured in the first three months of operation: fig. 24a shows dE/dx (truncated mean from more than 250 wires) plotted against the momentum p (GeV) of tracks from Z^0 decays. The lines are those expected for electrons, pions, kaons and protons. Figure 24b shows dE/dx distributions for pions

from hadronic Z^0 decays (left) and for electrons from Bhabha scattering at 45 GeV/c beam momentum. The resolution of the Bhabha peak is 4.5%.

The main properties of the TPC performance are summarized in table 8. The performance of the TPC can be judged from the invariant mass distribution of V^0 decays in these events, shown in fig. 25. The K^0 mass peak seen there has a resolution of $\sigma = 4$ MeV. The momentum resolution obtained, from the TPC alone, in this initial phase is $\Delta p/p^2 = 0.0015\ \mathrm{GeV}^{-1}$, as shown in fig. 26 from tracks with positive and negative charge. If the ITC information is used in addition, this figure is expected to decrease to $0.0010\ \mathrm{GeV}^{-1}$.

5. ELECTROMAGNETIC CALORIMETER

5.1 Overall description

The ALEPH electromagnetic (e.m.) calorimeter (ECAL) is a lead/wire-chamber sampling device of 22 radiation lengths (X_0) nominal thickness. The total energy and the position of the e.m. showers are measured using small (approximately $30 \times 30\ \mathrm{mm}^2$) cathode pads. The cathode pads are connected internally to form 'towers' pointing to the interaction point. Each tower is read out in three sections in depth ('storeys'), corresponding to the first 4, the middle 9, and the last 9 radiation lengths.

The calorimeter is a highly granular hermetic detector (3.9π sr covered by 73,728 towers), with cracks representing 2% of the barrel and 6% of the end-cap surfaces. It provides an e.m. energy resolution $\Delta E/E$ of $18\%/\sqrt{E}$ and operates within the ALEPH solenoidal magnetic field at 1.5 T. Construction methods have assured a tower-to-tower uniformity within 1.6% (r.m.s.). The mechanics and electronics of the barrel modules and end-cap petals have been designed to be as identical as possible.

5.2 Mechanical construction

The e.m. calorimeter is arranged as a barrel surrounding the TPC, closed at both ends with end-caps, as shown in fig. 27. The two types of subdetector elements — 'barrel' and 'end-cap' — are divided into modules, each subtending 30° in azimuthal angle ϕ, the end-cap modules having a 15° rotation with respect to the barrel modules. The entire e.m. calorimeter is rotated by -32.7 mrad ($-1.875°$) with respect to the hadron calorimeter in order to avoid overlapping of crack regions. The construction of the barrel and end-cap subdetectors differs somewhat owing to their geometries and differing stress loads. Thus their mechanical aspects are treated separately in subsections 5.2.1 and 5.2.2. The general aspects of readout geometry are as follows.

- The barrel region is organized in twelve 10.4 t modules. There are 4096 (32×128) towers per module, making a total of 49,152 towers in the barrel. Read out in three 'storeys', there are 12,288 channels for each module (147,456 for the entire barrel). Since the geometry is 'projective', some of these channels are not (or are only partly) equipped.
- The end-cap regions are each organized into twelve 2.6 t modules. There are 1024 towers per module, 24,576 for both end-caps. Read out in three 'storeys', there are 3072 channels for each module (73,728 for both end-caps).

The e.m. calorimeter is a sandwich of 45 lead/proportional wire-chamber layers. The wire chambers are made of open-sided aluminium extrusions. Ionization from an e.m. shower developed in the lead sheets is amplified in avalanches around 25 μm diameter gold-plated tungsten wires. The signals are read out capacitively via the extrusions' open faces with cathode pads placed behind a highly resistive graphite-coated Mylar 'window'. The structure of a typical single layer of the calorimeter is shown in fig. 28. (Details of layer composition differ between end-cap and barrel modules, see below.) The pads from consecutive layers are connected to form towers pointing at the

intersection region. They are summed independently in three depths ('storeys'), corresponding to the first 'stack' ($\simeq 4X_0 = 10$ layers of 2 mm lead sampling), the second 'stack' ($\simeq 9X_0 = 23$ layers of 2 mm lead sampling), and the third 'stack' ($\simeq 9X_0 = 12$ layers of 4 mm lead sampling). The capacitance of a tower storey varies with position; typically it is about 2 nF. The average radiation length in stacks 1 and 2 is between 2.0 and 2.4 cm, and in stack 3 it is 1.3 or 1.4 cm.

The cross-section of a tower as viewed along its axis is roughly 30.4 × 30.4 mm^2 at the front face of the calorimeter. The segmentation is thus 0.94° in azimuthal angle $\Delta\phi$ and 0.93° × $\sin\theta$ in polar angle $\Delta\theta$ for the barrel.

5.2.1 Barrel modules

The mechanical design of the barrel modules was optimized to satisfy three basic requirements: i) uniform spacing of anode wires from the readout pads and extrusion walls, in order to ensure uniform pad response; ii) good gas tightness; and iii) minimum 'dead' areas between adjacent modules' sensitive regions. The essential mechanical elements are shown in fig. 29. The calorimeter stack has 45 layers, with each anode wire plane having 195 to 233 sense wires which run parallel to the z-axis of ALEPH and thus parallel to the main component of the magnetic field.

The wires lie in the channels of the aluminium extrusions. The channels have inner dimensions of 3.2 mm × 4.5 mm, the rib thickness is 0.5 mm, and the base is 0.6 mm thick (overall thickness is thus 3.8 mm). The 'free' wire length between circuit-board inner edges is 4630 mm for all anode planes. The wires are strung with a tension of 65 g and supported and positioned every 450 mm by a plastic spacer. This introduces a 6 mm wide local dead zone. Therefore, for each wire layer, the positions of the spacers are varied systematically to avoid coherent effects on the energy deposition of showers.

Each of the 45 cathode planes in one module is cut in a rectangular pattern into pads. The width of the pad rows is the same in ϕ (32 rows), but it increases from the centre outwards in θ in order to have the transverse width of the towers match the shower size. There are 184,320 pads in each barrel module (45 × 32 × 128); within one tower, the first 10, the middle 23, and the last 9 layers are connected, resulting in 12,288 readout channels.

5.2.2 End-cap modules

The design criteria were the same as for the barrel modules. Figure 30 shows the components of each petal module. The wire layers contain 210 sense wires on a 5 mm pitch. The wires run parallel to the right-hand side of the petal, viewed from the front with the narrow end uppermost. The wires, with a maximum length of 1.7 m, are supported by a plastic spacer every 350 mm. Cathode-pad sizes are given by the tower structure of the calorimeter. There is a maximum of 50 pad rows in θ in any layer of the petal. Each pad row is divided into equal ϕ segments across the full 30° angle of the petal. The pad arrangement is given in table 9.

5.3 Gas system

The e.m. calorimeter is operated with a mixture of Xe (80%) and CO_2 (20%). The high-Z gas is chosen to minimize the contribution of path-length fluctuations to the energy resolution, which are due to δ-rays propagating perpendicular to the shower direction, along the sense wires in one tube. Gas gain in the tubes depends on the gas mixture, the absence of impurities, and the gas density. The gas system keeps the Xe content in the mixture at 80 ± 1% and purifies the recycled gas. The gas pressure is kept constant at about 60 mbar above atmospheric pressure. Pressure and temperature are monitored in each module. In addition, each module contains a small single-wire chamber (3.5 × 3.5 × 20 mm^3), equipped with a ^{55}Fe source. The charge collected on the wire, initiated by the 6 keV X-rays, is used to monitor the gas gain.

5.4 Electronics

5.4.1 Overview

The main characteristic of the ECAL electronics is the large number of analog channels to be read, 221,184 pad channels and 1620 wire channels (see table 10).

Every physical pad tower in the calorimeter is divided in depth into 3 storeys, each connected to an independent electronic channel. Conversely all wires in a wire plane are readout together on a single channel. This explains the large factor between the number of channels of each type: a barrel module contains 12,288 pad channels but only 45 wire planes.

Since the number of cables between the detector and the electronics, as well as the number of ADCs and readout crates had to be kept at a manageable level, it has been necessary to multiplex the pad channels at the front end by 32 and again by 8 before the ADC.

5.4.2 Analog chains

a) Pads

Each pad tower with a capacitance of about 2 nF is directly connected to an integrated BIFET operational amplifier of reasonably low noise (20 nV/$\sqrt{\text{Hz}}$), which integrates the charge on a 200 pF feedback capacitor (see fig. 31). It is followed by a sample-and-hold circuit and a 32-channel multiplexer. This multiplexer is built using CMOS analog switches. The unit first forms an analog sum of the 32 channels for trigger purposes. When the sample-and-hold circuit has finished integration, the 32 charges are sequentially transmitted to the cable drivers. Two drivers with a gain of 1 and 8, respectively, are used for each group of 32 channels. In this way, a dynamic range of 2^{16} is obtained from the 12-bit ADCs connected to each multiplexed readout channel.

b) Wires

Because of the higher capacitance of about 10 nF per wire plane and the much smaller number of channels, a more conventional design with better noise performance was chosen. Here a common base transistor is followed by a differential cable driver. At the other end of the 30 m long cable, the signal is amplified and integrated. Again there are two outputs with a gain of 1 and 8, respectively. The channels are then also multiplexed in groups of 32. For trigger purposes, the sums of even- and odd-numbered planes are formed at this stage.

c) ADC

Each twisted-pair cable sequentially carries the charges from 32 channels to one input of an 8-fold multiplexer. This is followed by a 12-bit ADC (AM 6112) working in the successive approximation mode. This ADC sequentially digitizes the analog signals from each of the 256 channels connected to it. The total operation time is 3.7 ms including the settling time after switching channels between conversions.

Twelve ADC chips are mounted on a single-width FASTBUS module. After completion of all conversions, this module performs a zero suppression by comparing the results for each channel with thresholds preloaded in its memory. The unit then generates the address of each channel fired and the corresponding digitized pulse height.

The complete sequence of sampling, multiplexing, converting, and resetting the front end is controlled by a microprogrammed sequencer, housed in a FASTBUS module and linked to the front end boxes and the ADC modules.

d) Tests and calibration

Each wire chain can be tested and calibrated by injecting test pulses at the detector level. For the pad chains, owing to the number of channels involved, test pulses can only be injected after the

front-end multiplexer. The gain of the first part of the chain (integrating amplifiers + multiplexer) depends only on the ratio of two capacitors, selected to be 1.000 ± 0.005 during fabrication.

For test purposes, it is possible to inject pulses on each wire plane of the detector and to measure the response of each pad channel. This allows a check of the connections between pads and amplifier and of the proper operation of each amplifier. It is not possible to calibrate the complete pad chain in this way since the ratio of wire and pad capacitances varies over a module owing to the slight mechanical non-uniformity. On the other hand, this method is used for barrel modules to measure the distance between pad and wire—from which the wire position in the cell is deduced—and thus to determine the wire gain and the module gain maps for pads and wires. Such a procedure is precluded for the end-caps because of stray capacitances.

5.4.3 Digital readout

a) Readout controllers

After zero suppression in the ADC, the data are read out by a Readout Controller (ROC). This module is a FASTBUS master in the crate and is mainly based on a fast bit slice processor. Each ROC reads 17 (barrel) or 27 (end-cap) ADCs and performs the pedestal subtraction and gain correction on their data. It then reorders the data and formats them before they are read by the Event Builder (EB) on its slave cable port (see fig. 32).

b) Event builders

A single EB for the whole ECAL reads out the data from the ROCs and reorders them. It then sends the events to the main ALEPH Event Builder through its cable port. For monitoring purposes, events can also be sent to the ECAL VAX via an EVI and an optical link (see fig. 32).

c) Error handling

Errors detected by the ROCs (e.g. FASTBUS errors in the ROC crate, protocol errors in the trigger signals) are reported to the EB. The EB detects in addition FASTBUS errors in its link to the ROCs and protocol errors in this transmission. It reports all errors to the data acquisition VAX.

5.4.4 Precision

The overall measurement precision is given in table 11. The total energy per module (sum of 45 wire planes) can be measured with a 10 MeV dispersion. This gives the possibility of triggering at the 200 MeV level. For the pads, the single-channel noise is not a good measure of the detector performance since about 100 channels have usually to be added to cover the extension of a typical shower. Instead the correlated noise between channels, which is due to low frequency pick-up, is the dominant factor. For example, the sum of 96 channels is measured with a typical dispersion of 100 MeV, to be compared with 60 MeV expected in the absence of correlation.

5.5 Performance

5.5.1 Spatial and angular resolution

The e.m. calorimeter was designed to have the best possible granularity in order to simplify the identification of electrons inside hadronic jets and to facilitate the measurement of photon energies in a background of hadrons. This granularity varies between 17×17 (mrad)^2 at $\theta = 90°$ in the barrel and 9×10 (mrad)^2 at $\theta = 40°$ in the end-cap. The centre of gravity of a shower is reconstructed from the four leading towers

$$\theta = \frac{\Sigma_{i=1}^{4} E_i \theta_i}{\Sigma_{i=1}^{4} E_i}, \qquad \phi = \frac{\Sigma_{i=1}^{4} E_i \phi_i}{\Sigma_{i=1}^{4} E_i},$$

where E_i is the energy deposit in tower number i of which the centre coordinates are θ_i and ϕ_i. Figure 33 shows data taken in a test beam with 10 GeV electrons. The data are represented as two-dimensional plots: $\theta - \theta_0$ versus θ_0, and $\phi - \phi_0$ versus ϕ_0; θ_0 and ϕ_0 correspond to hit coordinates of the incident particles. The 'S shapes' that are observed arise from the fact that the transverse dimensions of the tower are close to the e.m. shower size.

This effect can be suppressed by correcting the centre-of-gravity coordinates θ and ϕ with periodical functions of θ_0 and ϕ_0:

$$\theta_c = \theta + c_1 \sin [2\pi\theta_0 + d_1 \sin 2\pi\theta_0] ,$$

$$\phi_c = \phi + c_2 \sin [2\pi\phi_0 + d_2 \sin 2\pi\phi_0] .$$

The constants c_i and d_i are obtained from fits to electron test data at various angles θ and ϕ and energies E. They are found to be almost independent of θ, ϕ, and E:

$$c = c_1 = c_2 = (9.3 \pm 0.7) \times 10^{-2} \text{ tower units}$$

$$d = d_1 = d_2 = (0.45 \pm 0.15) \text{ rad} .$$

This correction reduces the width of the distributions in $\theta - \theta_0$ and $\phi - \phi_0$ by a factor of 2. The corrected distributions are shown in fig. 34 for 10 GeV electrons. The standard variations of Gaussian fits are given by:

$$\Delta\theta = \Delta\phi = a + b/\sqrt{E} , \tag{8}$$

where

$$a = (2.0 \pm 0.2) \times 10^{-2} \qquad \text{(in tower units)} ,$$

$$b = (17.6 \pm 0.9) \times 10^{-2} \text{ GeV}^{1/2} \qquad \text{(in tower units)} .$$

The energy dependence is shown in fig. 35 for data with 10, 25, and 50 GeV electrons. In this energy range, the angular resolution for e.m. showers is below 1×1 (mrad)^2 over the whole detector.

5.5.2 Energy resolution

The energy resolution was measured for barrel modules at 10, 25, and 50 GeV and for end-cap modules at eight energies between 5 and 70 GeV at an operating voltage of 1340 V. For the barrel modules, the energy resolution for the wires is consistent with (fig. 36)

$$\Delta E/E = a + b/\sqrt{E} , \tag{9}$$

with a small constant term

$$a = (0.3 \pm 0.1)\%$$

and a slope

$$b = (16.5 \pm 0.3)\% \text{ GeV}^{1/2} .$$

For the end-cap modules, the data yield a = 0.45% and b = (17.0 ± 0.5)% $GeV^{1/2}$ for wire readout, and a = 0.33% and b = (19.2 ± 0.5)% $GeV^{1/2}$ for pad-cluster readout (fig. 37).

5.5.3 Linearity of response

The response E_m of the e.m. calorimeter increases approximately linearly with the energy of the incident electron, E, between 10 and 70 GeV energy. There is a small deviation from linearity which can be parametrized by the formula

$$E_m/E = 1 - \alpha E .$$

Test measurements then show values of $\alpha = (9.0 \pm 0.7) \times 10^{-4}$ GeV^{-1}, for angles of incidence between $\theta = 90°$ and 50°, at the nominal voltage of 1340 V. The observed non-linearity is the sum of a saturation effect (α_1) and a leakage effect (α_2): $\alpha = \alpha_1 + \alpha_2$. Assuming α_1 to be proportional to the gas gain, from measurements with different gains and different angles one obtains $\alpha_1 = (7.8 \pm 0.6) \times 10^{-4}$ GeV^{-1}. Space-charge saturation is the dominating effect. The gas gain G varies with the high voltage V, according to the power law $G \propto V^{16.2 \pm 0.1}$.

5.5.4 Pion–electron separation

This separation has been measured with a barrel module at 5 and 10 GeV particle energy. Energy responses for electrons and pions of 10 GeV are shown in fig. 38. Defining a pulse-height window with > 99% efficiency for electrons in fig. 38a, the fraction of pions simulating electrons is (1.5 ± 0.3)%, while most of the pions have much lower energy deposition. This pion rejection is improved by using the calorimeter segmentation. If only the energy in the four towers adjacent to the impact point of the particle with momentum p is summed (E_4), the ratio E_4/p shown in fig. 39 allows a sharper discrimination: for the cut $E_4/p > 0.75$, only (0.8 ± 0.2)% of the pion sample can fake electrons, while the electron efficiency remains above 99%.

Additional cuts are based on the longitudinal shape of e.m. showers, and on the comparison between barycentre reconstruction, as described above, and track-hit coordinates within spatial resolutions.

The final pion contamination for an electron efficiency larger than 95% is

$$\epsilon_\pi = (1.1 \pm 0.5) \times 10^{-3} \text{ at } 10 \text{ GeV} ,$$

$$\epsilon_\pi < 3 \times 10^{-3} \text{ at } 95\% \text{ confidence level at } 5 \text{ GeV} .$$

The test beam studies [15, 16] have also been used to reconstruct energy-independent estimators of the quality of electron identification based upon the compactness ratio E_4/p defined above (R2) and the longitudinal shower shape (R3). These two estimators are formulated to be normally distributed dimensionless quantities centred at zero. The first, R2, measures the deviation of the compactness of the shower from the expected transverse shape reconstructed in the calorimeter storeys:

$$R_2 = \frac{(E_4/p)_{measured} - (E_4/p)_{expected}}{\delta(E_4/p)} .$$

The second, R3, performs the same function for the longitudinal shower shape and is formed from the first and second moments of the longitudinal energy depositions measured in the three stacks. Applied to hadronic Z^0 events in the data, a plot of R2 as a function of R3 (fig. 40) shows electrons (above 2 GeV) clearly separated from other charged particles. This illustrates the power of the fine

granularity in ECAL, combined with the good spatial track resolution of the TPC, to identify electrons embedded in high-multiplicity jets.

The response of the ECAL to muons and pions (the latter in combination with the hadron calorimeter) have been reported earlier [15, 16].

5.5.5 Uniformity of response

The mechanical tolerances achieved and their expected influence on the variation in response from one wire layer are as follows:

	$\Delta g/g$ (%)	
	Pads	Wires
i) Vertical wire position: $\pm 30\ \mu m$	± 0.8	∓ 1.2
ii) Cell height (extrusion): $\pm 10\ \mu m$	± 1	
iii) Wire radius ($g \propto r^4$): $\pm 0.25\ \mu m$ in diameter	± 4 (locally)	
iv) Lead thickness: $\pm 50\ \mu m$ (if systematic in all layers)	± 2	

The global uniformity of response was tested with 20 GeV and 7 GeV electron beams for two barrel and four end-cap modules. The barrel modules were tested over a uniform grid of 4×4 towers, yielding about 220 points; the end-cap modules were scanned to cover 8 values of θ and 4 of ϕ with addditional measurements across the centre, yielding results for 40 points. The r.m.s. deviation of the mean responses over these areas lies between 1.0% and 1.7% for pads and between 1.6% and 1.9% for wires. Similar r.m.s. deviations between 1.0% and 2.1% have been found in tests with cosmic muons [17].

5.6 Energy calibration

Energy depositions in ECAL are measured from charges collected in the front-end electronic circuits attached to the individual pad storeys and wire layers of the modules. The relationship between energy deposited and charge collected can only be determined experimentally. The purposes of the energy calibration procedure are to determine this relationship absolutely for each detector element, to monitor variations with time, and to correct malfunctioning channels. The procedure described below refers specifically to the determination of e.m. energy depositions from primary electrons and photons. Different calibration constants apply to energies deposited by muons or hadrons.

The methods of calibration and monitoring subdivide as follows:

a) Absolute calibration from direct measurements with electrons of known energy.
b) Relative calibration both between modules (intercalibration) and between channels within modules (uniformity mapping). The secondary sources employed are radioactive gas and cosmic rays.
c) Short/medium-term drift monitoring using ^{55}Fe test cells (platines).

The relative accuracy of calibration between modules depends on

i) the details of mechanical construction;
ii) amplification (or gain) in the Xe + CO_2 gas layers;
iii) electronic gains of the analogue readout chain, including the front-end circuits and the digitization system.

5.6.1 Absolute calibration and ^{55}Fe test cell monitoring

Direct measurements of the response to electrons (and photons) of known energy between 2 and 70 GeV in the ALEPH test beam have been made with two barrel and four petal modules. These data

formed the primary source of absolute calibration for all 36 modules before LEP started. The analysis was restricted to fiducial regions away from edges and the overlapping corner, namely $45° < \theta < 135°$ for the barrel modules and $20° < \theta < 35°$ for the petals. The Xe + CO_2 gas-gain conditions were continuously monitored with intercalibrated ^{55}Fe test cells operating from the same high-voltage supply and setting as that for the anode wire planes.

Approximately 10 × 10 pad towers (300 channels) surrounding the electron beam impact point and all 45 wire layers were read out per event, using a charge integration time of 6 μs. In-burst pedestals from the same channels were sampled by a random trigger. Running mean values of the last 10 pedestals were used for subtraction from the measured summed tower response. Mean energies were determined by fitting the observed pedestal-subtracted spectra with a Gaussian, cutting at 2σ and re-fitting.

The calibration of the pad response to electrons is calculated from the average response to electrons within the defined fiducial regions using the following linear relationship:

$$E = \left(\frac{1}{C_M}\right) \sum_{k=1}^{3} \sum_{j} F_{jk} s_k (R_{jk} - P_{jk}) , \tag{10}$$

where

E is the nominal electron beam energy (in GeV);

C_M is the calibration constant of the module (in pC/GeV);

F_{jk} is the electronic gain (in fC per count) of the j^{th} storey in stack k;

s_k is the relative depth (in radiation lengths) of a wire layer in stack k ($s_1 : s_2 : s_3 = 1.0 : 1.0 : 1.935$);

R_{jk} and P_{jk} are the corresponding individual measured response and pedestal values (counts);

The F_{jk} factors are determined by injecting test charges into the summing amplifiers that serve groups of 32 channels in the pad readout.

The modules were calibrated under slightly different gas-gain conditions. Compensation for this difference was made using the intercalibrated ^{55}Fe test cells that monitor the mean charge collected from 6 keV X-rays absorbed in the same gas. The dependence of gas gain on density (i.e. on the ratio of the pressure to the temperature p/T) follows an inverse power law given by $(p/T)^{-\alpha}$. The exponent α has been determined experimentally at the working gas gain as a function of instantaneous variation in gas pressure at constant temperature. The results are:

$$\alpha(p/T)_e = -5.30 \pm 0.05 \text{ (stat.)} ,$$

$$\alpha(p/T)_F = -6.84 \pm 0.06 \text{ (stat.)} ,$$

$$\alpha_e/\alpha_F = 0.77 \pm 0.01 ,$$

where e signifies the electron beam and F the ^{55}Fe test cell dependences. Similar measurements of the power law gain dependence on the common high voltage applied to the test cell and the anode layers give the corresponding indices:

$$\beta(HV)_e = 16.2 \pm 0.05 \text{ (stat.)} ,$$

$$\beta(HV)_F = 17.6 \pm 0.01 \text{ (stat.)} ,$$

$$\beta_e/\beta_F = 0.92 .$$

Applying these corrections to the data gave the comparative electron calibration constants shown, for a barrel and petal module, in table 12 scaled to the ^{55}Fe test-cell gain of the barrel. The ratio of the pad calibration constants C_M between the barrel and end-cap modules is larger than unity, as was expected from the calculated sampling ratios between their passive and active layers.

5.6.2 Relative calibration between modules

Before LEP started, the principal method of intercalibration between modules was the measurement of response to the radioactive gas ^{83}Kr that had been introduced into the Xe/CO_2 gas system temporarily. The technique allows the wire response to be calibrated. The wire spectrum from each layer shows a clear peak at 9.4 keV and a higher-energy plateau extending to 40 keV (fig. 41), produced by internal-conversion electrons in the gas. The corresponding pad signal shows a broad peak for those disintegrations in the gas depositing at least 20 keV on the wire.

The anode spectra are recorded: i) for each wire layer (45 spectra), and ii) combined in layers 1–10, 11–33, and 34–45, corresponding to stacks 1, 2, and 3. These latter three spectra are subdivided into 4 × 4 tower regions using the pad signal for location (180 regions per petal; 750 regions per barrel). The upper part of each spectrum is analysed to determine the height of the plateau and the slope of the steeply falling edge, from which the ^{83}Kr calibration parameter or 'value' is determined as the half-height point down the falling edge. This point corresponds to a deposited energy of about 35 keV.

The ^{83}Kr parameters were determined, for the two modules calibrated during the period of electron test-beam running before the start-up of LEP, and are listed in table 12. They are equal, within errors, after correcting for operational differences of gas gain and high voltage. This result confirms that the difference in calibration between these modules, for electrons, arise from the variation in sampling ratios quoted above.

The ^{83}Kr radioactive gas technique has also been used to check the uniformity of response over the surface of a module. Using the wire spectra subdivided into 4 × 4 tower regions, it has been established that an excellent correlation exists with similarly obtained electron scan data (see fig. 42).

c) Time drift of gas gain

Owing to absorption of the Xe/CO_2 gas in the graphite layers of the modules, there is a gradual fall in gas density (p/T). An experimental fit to the evolution in time t gives

$$(p/T) = (p/T)_0 \, [1 - 0.147 \, (1 - e^{-t/\tau})] \, ,$$

where $\tau = 44.1$ days.

Over a LEP fill-period of ~ 6 hours, the time drift is rather small ($\leqslant 0.6\%$) for modules filled with gas for more than one week. Furthermore, the gain drifts can be followed accurately with the test cells for deviations of up to 10% in gain. In practice, the gain drifts are corrected by injecting small quantities of fresh gas ($\approx$ 1 mb per day and module). Tests have shown that gain stability to $\pm 1\%$ can be achieved over a 10-day interval.

d) Operation of the whole calorimeter in LEP

Following final installation of all 36 modules, the ^{83}Kr radioactive gas technique was employed to determine the operating conditions required to equalize the summed energy response from the wires of each module. The energy scale was set using the modules calibrated earlier in the test beam measurement.

This initial energy calibration was subsequently checked as soon as a sufficiently large sample of electrons from wide-angle e^+e^- Bhabha events over the Z^0 resonance had been recorded in each

module. Combining all these data, it was found that the energy spread for these electrons (E_{mean} = 45.6 GeV) was $\pm 5.5\%$, compared with a Monte Carlo prediction of $\pm 3.0\%$. This additional uncertainty is attributed mainly to systematic discrepancies in setting the relative calibrations, and as such contributes to the constant term a in eq. (9). The same Bhabha events were used to fine-tune the relative calibration constants with the result that the energy resolutions ($\pm \Delta E/E$) found for new data are now consistent with (i) $1.6\% + 17\%/\sqrt{E}$ for wires and (ii) $1.7\% + 19\%/\sqrt{E}$ for the pads.

5.7 Summary

The essential parameters of the e.m. calorimeter are summarized in table 13.

6. HADRON CALORIMETER AND MUON DETECTOR

The main support of the ALEPH apparatus is a large iron structure which serves both as the passive part of the hadron calorimeter and as the return yoke of the magnet. The iron is split into layers between which are placed the active or readout parts of the calorimeter consisting of limited streamer tubes. Outside this calorimeter structure are two additional double layers of streamer tubes, well separated so as to give both the position and direction of muons which penetrate the iron.

6.1 Mechanical design

The way in which the hadron calorimeter is subdivided into a central barrel and two end-caps and how this structure fits around the superconducting coil and e.m. calorimeter is shown in fig. 43.

6.1.1 The barrel

The barrel is dodecagonal in shape with each of its twelve modules split into two parts which are mirror images of each other. One such half module is shown in fig. 44. In depth the modules comprise 22 iron slabs, 5 cm thick, plus an outer slab of 10 cm. Spacers formed of iron bars are welded along the edges of the slabs so as to maintain the 22 mm gaps between them. Although these are necessary for the rigidity of the structure, they do reduce the space available for the streamer tubes. However this reduction is limited to a loss of only 3.4% of the cover in azimuthal angle. The first layer of streamer tubes is placed in front of the first iron slab and is kept in position by a thin aluminium sheet (5 mm) fixed in front of it. Subsequent layers of tubes are placed in each of the 22 gaps between the iron slabs.

The total thickness of iron is 1.2 m, corresponding to 7.16 interaction lengths for a hadron passing in a direction perpendicular to the slabs. The barrel modules are 7.24 m in length, but as can be seen from fig. 42 some of the iron is cut away at each end to allow cables from the inner subdetectors to pass through. In the topmost module of the structure there is an extra hole to accommodate the piping associated with the superconducting solenoid.

The streamer tubes are made of extruded plastic (PVC). Each tube has a base sheet with nine fins perpendicular to it forming eight long cells. The internal size of a cell is 9×9 mm^2 and the wall thickness 1 mm. The inner surfaces of each cell are painted with graphite and a 100 μm wire is positioned on its axis. The wires are soldered to cards at each end; one card distributes the high voltage but the other just provides mechanical support, there being no direct signal readout from the wires. Along the length of a cell the wire position is maintained by plastic supports placed at intervals of 0.5 m.

Signals are induced on electrodes on both sides of the eight-cell unit. The open side of the cells faces copper pads which are etched on Vetronite sheet with an earth plane on its reverse side. Twisted-pair cables, one grounded and one connected to the pad, carry away the induced signals. These are summed from pads in different layers so as to form signals from projective towers which

subtend an azimuthal angle of 3.7° at the interaction point. Thus each half module of the barrel is 4 towers wide in azimuth. Every tower also has the same width in polar angle and this is ensured by making the lengths of the pads proportional to $1/[\cos^2(90° - \theta)]$. Some 2688 towers are fully contained in the barrel while 768 are in the overlap region between barrel and end-cap. In general, the pattern of towers matches that of the e.m. calorimeter with about 14 of its towers covered by one tower of the hadron calorimeter. The distribution of towers is illustrated in fig. 45.

On the other side of the eight-cell unit, aluminium strips, one per cell, are positioned parallel to the wires. These are used to derive standard logic signals whenever the particular cell fires. This digital readout provides a two-dimensional picture of the hadronic shower and is also vital to the process of identifying muons.

Because the barrel modules are trapezoidal in cross-section and the eight-cell units have a fixed width, it is not possible to completely cover the layers with an integer number of units. To overcome this, passive spacers are inserted between units in such a way as to spread the sensitive regions within each layer without allowing the passive parts to line up along possible muon paths.

The streamer tube units are approximately 7 m long and as access is possible at both ends, gas and high tension are brought in at one end and the strip readout taken at the other. The need to accommodate electronics for this latter and also the presence of cables from the inner subdetectors means that the length of the tubes has to be varied slightly.

6.1.2 The end-caps

The end-caps each consist of six petals, and an example is shown in fig. 46. The narrow end of the petal has 22 slabs of iron, 5 cm thick, plus a 10 cm slab on the outside; but at the broad end, where the petal fits with the barrel, the overall number of slabs is reduced to 16. In order to withstand the large magnetic forces that pull the end-caps inside the magnet, and to maintain the 22 mm spacing between slabs, five iron bars are welded into each gap. This reduces by 6% the area of the petal that can be covered with streamer tubes.

Each layer of tubes has to be fitted into the four sections between the iron spacer rods. A section holds five plastic boxes with a pair of eight-cell units in each. The length of the boxes ranges from 0.4 m to 4.5 m to fit the petal shape. Only the outer edge of the petal can be accessed and so all gas pipes, and the high tension and signal cables are grouped at that end of the tubes. In each end-cap, the orientation of the tubes is horizontal for the four petals that have an edge in the horizontal plane and at 60° to the horizontal for the other two.

At the narrow end of the petal there are 22 layers of tubes and at the broad end 15. Where the barrel and end-cap overlap, the tower structure is continued across both, but because the petal layers are subdivided by the iron bar spacers some pads may be split between two sections. When this occurs the signals from the two parts are collected separately but subsequently added into the same tower sum. The equal width of the towers in polar angle is sustained throughout the petal, but the width in azimuthal angle changes on approaching the narrow end. At a polar angle of 34° the width in azimuth changes by a factor of 2 from 3.7° to 7.5°. At a polar angle of 18° it is doubled again to 15°. In total there are 2100 towers in the end-caps, of which 768 are shared with the barrel.

6.1.3 The muon chambers

The two double layers of streamer tubes which form the muon chambers are installed outside the iron. The disposition of these follows the layout of the hadron calorimeter barrel and end-cap sections, but in addition there are so-called middle-angle chambers placed over the outer edges of the petals thereby covering the region of overlap between end-cap and barrel. The position and the azimuthal distribution of all three types of chambers, barrel, end-cap and middle-angle, are shown in fig. 47.

The muon chambers do not contribute to the measurement of hadronic shower energy but are simply used as tracking devices with two coordinates read out from each layer of tubes by means of strip electrodes parallel and perpendicular to the wires. The former are 4 mm wide with 10 mm pitch while, in order to obtain a signal of suitable strength, the latter are 10 mm wide on a 12 mm pitch; the two members of a double layer are offset with respect to each other by half a pitch in both directions to ensure good efficiency and spatial resolution. The separation between the two double layers is 0.5 m for the barrel and middle-angle chambers and 0.4 m for the end-cap. This enables track directions to be measured with an accuracy of 10–15 mrad.

6.2 Operation

In this section, the various aspects of the calorimeter operation from the limited streamer tubes and their gas system, through the readout electronics to the data-acquisition system, are discussed.

6.2.1 The limited streamer tubes and gas system

Streamer or Iarocci [18] tubes are similar in construction to proportional counters, having a gas-filled tubular cathode with a fine anode wire along its axis, but they operate in a slightly higher voltage regime. An incident charged particle produces a local avalanche around the central wire, the size of which is independent of the amount of primary ionization created by the incoming particle. The standard gas mixture for such tubes is argon (30%) + isobutane (70%) but for underground experiments such a high hydrocarbon content is deemed unsafe and so ternary mixtures obtained by adding CO_2 have been tried. Two that have been tested for the ALEPH hadron calorimeter and muon chambers are Ar + CO_2 + isobutane and Ar + CO_2 + n-pentane. A systematic study [19] of the influence of gas composition on the efficiency, the distribution of streamer sizes, and the stability of operation has been carried out. However, the freedom of choice is severely restricted by safety regulations to those mixtures with at most a 30% hydrocarbon content and to gas systems which do not use the hydrocarbon in liquid form. The latter restriction eliminates the use of the mixture containing n-pentane.

For stable and reproducible operation the first requirement is a wide high-voltage plateau throughout which the process of streamer formation is fully efficient. For fixed hydrocarbon content the width of the plateau can be effectively controlled by adjusting the ratio Ar/CO_2 — the best values lying in the range 20–40%. Taking account of these restrictions, the gas mixture chosen for the hadron calorimeter and muon chambers consisted of Ar + CO_2 + isobutane in the proportions 13% + 57% + 30% for which the length of the high-voltage plateau is more than 500 V and after-pulses contribute less than 10% to the streamer count. The operating voltage is 4250 V and the energy resolution of $90\%/\sqrt{E}$ is only slightly worse than that attainable with the standard gas mixtures.

The total gas volume of the combined hadron calorimeter and muon chambers is 54 m^3, and this volume is exchanged every two to three days. This implies a flow of about 0.4 m^3/h, which is achieved with a control system capable of delivering up to twice that rate. The flow rates of the component gases are monitored to an accuracy of $\pm 1\%$ full scale and a reproducibility of $\pm 0.2\%$ with mass flowmeters. The total fluctuation in the charge per streamer due to flow variations within these limits is expected to be less than 4%.

Additional standard ALEPH streamer tubes are incorporated in the gas circuits adjacent to the control units, and at the entrance and exit of each module, in order to monitor charge spectra and singles rate plateaux and thereby follow gas-mixture variations. This information can then be used to correct drifts in the detector calibration.

Gas storage, mixing, and venting is done at the surface and a single pipe carries the mixture down to the input manifold in the underground experimental zone. As well as feeding the distribution system, the manifold has a line for gas mixture monitoring and a bypass to the return

manifold. The distribution system fans out in a tree-like structure; ultimately, the flow through each branch is equalized by means of needle valves. Flow rates and pressures are carefully monitored and the detection of any leakage or overpressure generates an alarm.

6.2.2 The electronics

The hadron calorimeter is the source of three different types of signals; those from the pads, which are used to measure the energy deposited in the calorimeter; those from the strips, which provide the pattern of the fired tubes in the event; and those from the wires, which give the energy deposited in single planes and are used for triggering.

The formation of a streamer avalanche in one of the tubes induces a positive pulse on the pad electrode facing the open side of the appropriate tube plane. A typical pad pulse has a peak of 5 mV into a 50 Ω load, a rise-time of 50 ns, and a fall-time of about 200 ns. Signals from pads in the same projective tower are summed electronically in so-called mixer boxes, four per calorimeter module, mounted on the detector. The summed signals are then transported via twisted pair cables to the counting room barracks where they are fed into FASTBUS ADC units.

An overview of the pad electronics is shown in fig. 48. The pad signals for each tower are summed in two halves via resistances mounted on the basic mother board of the mixer unit. These summed signals are then fed via hybrid amplifiers and matched into the long cables to the counting room through a patch panel. At the input to the ADCs in the counting room a paddle card correctly terminates the cable and attenuates the signal to within the ADC range which is automatically selectable at either 200 pC or 1600 pC full scale. For the overall system a typical pedestal distribution displays a fluctuation of 3 pC, which can be compared with the 280 pC signal given by a muon at normal incidence to the module.

The formation of a streamer avalanche also induces a positive pulse on the strip electrode situated on the opposite side of the tube plane from the pads. The characteristics of this signal depend upon the strip length; a typical pulse has 6 mV amplitude, 10 ns rise-time, and about 50 ns fall-time. This pulse is converted into a 1 μs long digital signal by a hybrid amplifier-discriminator, the effective input threshold of which can be lowered to 2 mV. This digital signal is latched into one bit of a shift register. The shift registers from up to 256 channels are chained together and, in order to speed up the readout, the information from 24 shift register chains is transferred in parallel to an ALEPH strip readout scanner (ASTROS) situated in a FASTBUS rack in the counting room. An overview of the digital readout system is shown in fig. 49. The splitter board in this figure acts as an interface between the scanner module and the 24 shift register chains, fanning out the ASTROS control signals, the discriminator threshold level, and the low voltage supply. There is also the facility of setting a mask pattern which enables the selection of specific shift register chains. The ASTROS modules are controlled by the Hadron Calorimeter Processor (HCP), and in normal data acquisition the processor initiates a load sequence in which the shift register information is transferred to the ASTROS for scanning and formatting before being moved to the HCP buffer. The ASTROS can also test the front-end electronics by loading into and reading back from the shift register chains, cyclic 24-bit patterns.

The third signal induced by the formation of the streamer avalanche is that on the wire itself and this can be picked up by appropriate capacitive coupling. The wires of each eight tubes in a plane are connected in parallel so it is not possible to obtain signals from individual wires. The treatment of these signals is inextricably linked with the high-voltage system and in fact the distribution boxes mounted on the detector, as well as fanning out the high voltage, also sum the wire signals from all the eightfold tubes in a plane, discriminate these with respect to a remotely set threshold, and enable the pulsing of the wires in a selected plane for test purposes.

6.2.3 The data acquisition

The layout of the hadron calorimeter data-acquisition system is shown in fig. 50. The system comprises four coupled pairs of FASTBUS crates, one for each end-cap and two for the barrel, plus a single FASTBUS crate containing the main hadron calorimeter data acquisition control units, the Event Builder (EB) and the Trigger Supervisor (TS). The individual pairs of crates are controlled by an HCP, which is also capable of operating in stand-alone mode. The operational mode of the HCP is selected by setting its control status registers. By this means it is possible to determine whether the sequence of acquisition is started by software, as is the case for pedestal measurement or wire pulsing through the HV boxes for example, or started by the early gated beam crossing pulse (EGBX) which comes from the TS, as in normal data taking.

6.3 Performance

In this section we deal with some aspects of the performance of the hadron calorimeter including a discussion of its calibration. Details of the results of beam tests on prototype modules of the barrel and end-caps have been published elsewhere [20].

6.3.1 The analog signals

After pedestal subtraction the signals from the towers are summed to give the total charge collected in association with an incident particle. Such charge distributions for 20 GeV pions and muons are shown in fig. 51. These results come from test-beam measurements, and also shown in the figure are the charge response and resolution as a function of energy for pions. The gas used in this case was Ar + CO_2 + n-pentane, but as mentioned above the resolution obtained for the ternary mixture containing isobutane is only slightly worse. The calibration factor is (155 ± 2) pC/GeV. The angle of incidence of the test-beam particles was 30° to the normal and this leads to a slight decrease in the resolution, which is due to the effective increase in the thickness of iron traversed and the consequent poorer sampling of the shower. Comparison with test-beam measurements on electrons produced a value for the visible energy ratio for electron to pion of 1.33 ± 0.04.

The rise-time of the pad signal is about 50 ns and, although signals from individual streamers arrive at different times, this spread is small and the large number of streamers involved means that the time response of the calorimeter to high-energy hadrons is fast with an event-to-event fluctuation of only a few nanoseconds. Thus the calorimeter signals are well suited for triggering the experiment on hadrons and muons and this is discussed below in the section on the trigger.

6.3.2 The digital signals

Typical patterns of fired tubes produced by the strip digital readout of the calorimeter for single pions, muons, and electrons of 10 GeV energy are shown in fig. 52. As can be seen the different cases are quite distinctive. For planes which are hit the average number of strips fired for an orthogonally traversing muon is 1.6. This is due partly to δ-ray production and partly to the strip on one tube picking up the signal from an adjacent tube. The average total number of hits per muon varies from 32 to 40 for angles of incidence ranging from normal to 40° to normal. At low energy pion showers give 5.5 ± 0.8 hits per GeV and, if the energy is lower than about 5 GeV, then measuring the energy by counting the number of hits gives a better resolution than using the analog signal.

6.3.3 Calibration

There are two aspects to the calibration of the hadron calorimeter. One has to do with equalizing the response of all towers and the other involves the overall calibration constant, in pC/GeV, and its monitoring during data taking.

Under the first is included correction for the various insensitive regions which arise because of spacers and the gaps through which cables pass. Also included are the two effects which depend upon the angle of incidence of the particle. One is that the effective thickness of iron increases with angle as the particle direction moves away from normal incidence and the resulting coarser sampling leads to an undermeasurement of the energy. The second angular effect is due to the increased number of streamers per plane as the obliquely incident particle passes through more tubes in each layer. These effects have been studied in a test beam with both pions and muons, and for different angles and configurations, including the region of overlap between the barrel and end-cap.

The tower-by-tower correction factors have been determined using the full simulation of the ALEPH detector in the Monte Carlo program GALEPH and their values checked against the test-beam measurements. Satisfactory agreement has been obtained and the full set of factors installed in the HCP memory so that raw data are corrected to uniform response before being sent to the reconstruction program JULIA.

Studies in the test beam have shown that the total charge collected per muon does not depend upon energy, provided that full penetration of the module is ensured ($p_\mu > 5$ GeV/c). For normal incidence a muon produces 21 streamers on an average and a signal equivalent to a pion of 2.7 GeV energy. Thus for example, on an average, 10 GeV pions produce 78 streamers. In the underground experimental zone a cosmic-ray muon rate of 1 Hz gives a continuously available source for use in dedicated calibration runs of the calorimeter.

During the data-taking runs, variations in the calibration factor due to changes in the gas composition or ambient temperature and pressure are monitored with control tubes installed in the gas lines of each module, two in front and two behind. A collimated strontium source produces electrons which pass through the first tube into the second. Signals from the second are used as trigger in collecting the pulse-height spectrum of the first. An extensive comparative study using a test beam and cosmic-ray muons has indicated that the stability of the control tubes is sufficient to hold the calorimeter calibration to better than 2%.

As a summary to this section, the main parameters of the hadron calorimeter and the muon detector are listed in table 14.

7. LUMINOSITY MONITORS

7.1 Design considerations

The luminosity is determined from the rate of Bhabha events at small scattering angles. In this kinematic region, the interference between γ and Z^0 is almost negligible and the cross-section is well known from QED. The differential cross-section for small scattering angles θ is, in lowest order of α

$$\frac{d\sigma}{d\Omega} = \frac{4\alpha^2}{E^2}\frac{(\hbar c)^2}{\theta^4}$$

where E is the electron energy.

The luminosity monitor is designed for a systematic uncertainty of about 2%, so that the error in the annihilation cross-section will not be dominated by the uncertainty of the luminosity. Such a precision can be obtained with detectors in which the scattered electron and positron are measured in coincidence on both sides of the interaction region. A precise measurement of angles, especially of polar angles, is necessary since the Bhabha cross-section is a steep function of the scattering angle. A good determination of the energy of the electron and positron is needed for their identification and for background rejection. These measurements are done in two instruments: the luminosity calorimeter (LCAL) and the luminosity tracker, also called the Small Angle Tracking Device (SATR). A combination of one tracker and one calorimeter, representing one half of the main

luminosity monitor (fig. 53) is situated on each side of the interaction point, roughly at $z = +2.7$ m and $z = -2.7$ m. For polar angles between 55 and 90 mrad the measured electrons or positrons first go through the tracker, which is an arrangement of drift tubes, then into the calorimeter, a sandwich structure of lead and proportional tubes very similar to that of ECAL.

The tracking device accepts electrons and positrons with polar angles between 40 and 90 mrad, LCAL those between 45 and 155 mrad. They overlap between 45 and 90 mrad.

At a luminosity of 10^{31} cm^{-2} s^{-1}, the luminosity calorimeter counts Bhabhas at a rate of 0.3 Hz, similar to the total rate of resonant Z^0's in the ALEPH detector.

In order to provide a fast relative luminosity measurement, we have installed a Bhabha Calorimeter (BCAL) at very small angles (fig. 54). It counts Bhabhas at a rate 20 times higher than the main luminosity monitor, and consists of a system of four small calorimeters located pairwise—at $z = +7.7$ m and -7.7 m, behind the low-β quadrupoles—having a minimum detection angle of 5 mrad.

7.2. The small-angle tracking device (SATR)

7.2.1 Mechanics

The complete tracking device consists of thirty-six half planes of drift-tube chambers which are arranged in four quarter detectors, two quarters to be mounted on each side of the interaction point. One half plane is made of four 45° sectors, each of which contains fourteen drift tubes (fig. 55). The nine planes of one quarter detector are rotated by 15° with respect to one another to avoid dead zones. Because of the 45° degree modularity of the sectors, there are three sets of planes with different wire orientation. Planes within one set (i.e. numbers 1, 4, 7; 2, 5, 8; and 3, 6, 9) have the same position in azimuth.

The individual drift cells forming one 45° sector are made from brass tubes with a square cross-section of 9.95×9.95 mm^2 outer dimension and a wall thickness of 300 μm. The positioning of the 25 μm anode wire is guaranteed by notches cut in precison epoxy supports.

The amount of material in front of the luminosity monitor varies between 14% and 7.3% of a radiation length in the angular range from 40 to 90 mrad.

7.2.2 Electronics

The anode signals are amplified and then digitized in a 10-bit TDC with a precision of 1 ns. Because of space limitations for preamplifiers at the detector, some pairs of wires are ORed into one preamplifier. For the 2016 wires, there are 1152 readout channels, each equipped with a TDC. The digitized information is read out through buffer cards into an event builder (EB). The readout from the event builder follows, as for the other subdetectors.

7.2.3 Performance

The detector is operated with a gas mixture of Ar(90%) + CO_2(10%) and 1% isopropanol. The spatial resolution of the single drift cell was found to be (320 ± 20) μm, which leads to an r.m.s. error of the track polar angle of about 0.08 mrad. Accordingly, the azimuthal resolution of the entire chamber was found to be about 13 mrad. The latter values correspond to an r.m.s. of the fitted track position of 200 μm in the radial direction and 2 mm in azimuth. The overall reconstruction efficiency was determined to be 99%.

The final alignment of SATR is done with the Bhabha events. An uncertainty in the inner radius of the SATR acceptance of 0.1 mm results in a 0.25% error in the luminosity.

The main parameters of SATR are given in table 15.

7.3 The luminosity calorimeter (LCAL)

The luminosity calorimeter is a lead/wire-chamber sampling device of 24.6 radiation lengths nominal thickness. It is placed around the beam pipe on both sides (upstream and downstream) of the interaction region; the first sampling layers are at $z = +266.8$ cm and $z = -266.8$ cm from the nominal interaction point. The sensitive area is shown in fig. 56.

The total energy and the position of the e.m. showers are measured using small ($\sim 30 \times 30$ mm^2) cathode pads. The cathode pads are connected internally to form 'towers' pointing to the interaction point. Each tower is read out in three sections in depth ('storeys') corresponding to the first $4.77X_0$, the middle $10.6X_0$, and the last $9.25X_0$. There is a total of 38 sampling layers: 9 in the first storey, 20 in the second, and 9 in the third. The lead sampling thickness is 2.8 mm in storeys 1 and 2, and 5.6 mm in storey 3.

7.3.1 Mechanical design

The LCAL is made up of four semicylindrical modules, with a hole for the beam pipe. The outer radius is 52 cm and the inner radius is 10 cm. The length of a module is 45 cm. On each side of the vertex, a pair of modules occupies the region between the beam pipe and the end-cap of ECAL. The mechanics and the electronics of LCAL have been designed in such a way that they are nearly identical to those of ECAL. The differences are mainly those dictated by the geometry and the available space.

The sampling layers are accurately positioned by two bronze dowels, 40 mm in diameter, passing through precision holes in the layers and supported by the front-plate and end-plate. The difference between the diameter of the hole and that of the dowel is 80 μm.

7.3.2 Wire layers

Each layer has 112 gold-plated tungsten wires, 25 μm in diameter and with a 5 mm pitch. The wires run parallel to the ALEPH y-axis, nearly vertically. Wires of a length less than 200 mm have been omitted from the construction. The wires lie in grooves in an Al extrusion. The positioning of the wires is controlled by 3 mm wide Noryl wire supports running orthogonally to the wires.

7.3.3 Cathode layers

Each lead layer is a laminate of lead, plastic, graphite, and 1.0 mm thick printed-circuit board.

The cathode pad pattern is like that of a chess-board, with square pads varying in size from 28.6×28.6 mm^2 in layer 1 to 31.8×31.8 mm^2 in layer 38. The edges of the pads are parallel and orthogonal to the wires.

For reasons of economy, the pad boards are made in multiples of 5, 6, or 7. The pad boards in layers 1 to 6 are identical, and so are those in layers 7 to 13, 14 to 20, 21 to 27, 28 to 32, 33 to 38. This gives an overlap region in the borders between towers, with an average maximum size of about ± 2 mm, which is small compared with the width of the showers.

The error on the relative positions of the cathode pads inside a layer is 120 μm. The expansion due to an increase in temperature of 2 °C, contributes 25 μm to this error. The positioning of the detector layers is fixed by means of steering pins that go through precision holes drilled in the printed-circuit board and the lead sheets. The holes in the lead sheets are positioned accurately with respect to the precision dowels that carry the stack. The position of the supporting holes for the dowels in the front-plate and end-plate is given by reference marks on the plates. In this way the average x and z positions of the pads will be known with an accuracy of 140 μm with respect to the centre of a pair of modules. The survey, together with the construction accuracy, determines the overall position of a pair of modules with a precision of 0.25 mm in each direction.

7.3.4 Signal readout

In addition to the analog signals from each tower storey, an analog signal is available from each wire plane (38 planes per module). These signals are used in testing and calibrating the modules, but can also be used in the analysis. The total number of cathode channels read out is 4608. These are multiplexed at two levels: i) at the front-end amplifiers placed in boxes on the calorimeter modules, where summing amplifiers sequentially read out 32 front-end Sample and Hold amplifiers; ii) at the FASTBUS analog-to-digital converters (MUX-ADC) where each group of eight input signals are multiplexed together. FASTBUS sequencer cards give the necessary switching sequences for both operations. A double-gain system is used ($\times 1$ and $\times 8$ signals sent from the front-end sums) in order to obtain a 16-bit dynamic range from 12-bit successive approximation ADCs. A zero suppression at 10 counts is performed at the MUX-ADC level. Calibration-constant corrections are performed by the readout controller (ALEPH EB). The electronics system is almost identical to the one used in ECAL as described in section 5.4.

7.3.5 Gas system

The calorimeter operates at approximately 60 mbar above atmospheric pressure with a Xe (80%) + CO_2 (20%) gas mixture. The gas circulates in a closed loop for each module (at constant volume and pressure, hence constant density) in order to maintain constant gas amplification. LCAL is supplied from the ECAL gas system which is discussed in section 5.3.

7.3.6 Energy calibration

The calibration system for the detector is similar to that used for ECAL. The calibration factors used are as follows:

- A calibration factor which translates ADC counts in GeV, and which depends on time and on the module number. It is determined from test-beam data and updated using selected e^+e^- events. Typical values for the calibration factor are 4.8 MeV per count for storeys 1 and 2, 9.6 MeV for storey 3, and 0.3 MeV per count for wire planes. The precision is limited by statistics and is estimated to be better than 2% for each run. The calibration factor is applied on-line and corrected off-line. In addition, the gas gain fluctuations are monitored by a ^{55}Fe test cell mounted on each module as described in subsection 5.6.1. This factor is applied off-line.
- An electronic gain factor depending on channel number resides as a table in the EB and is only used on-line.
- A pedestal depending on the channel number and the time. It is updated dayly and resides as a table in the EB.

7.3.7 Summary

The main characteristics of LCAL are listed in table 16.

7.4 The very small angle luminosity monitor BCAL

The main goal of BCAL is to provide an on-line monitoring of the relative LEP luminosity, so that it is available to the persons on shift. The measurement is achieved by a system of four calorimeters (described below), which detect very small angle Bhabha events with an expected rate of 5 Hz at 10^{31} cm^{-2} s^{-1} luminosity, 20 times higher than that of the main luminosity monitor. A statistical precision of 5% can thus be achieved in 1.3 min of monitoring time at the above luminosity.

The four monitors that make up BCAL are located on each side of the beam pipe in the (x-y) plane (fig. 54) and on each side of the interaction point (fig. 57). The beam pipe is elliptical in the

region from 7.66 m to 7.91 m in z, so as to place the monitors as close as possible to the beam line. The active area of the counters starts at 6.5 cm from the beam.

The superconducting (mini-beta) quadrupoles located in the region 3.7 m $< z <$ 5.7 m defocus Bhabha electrons and positrons going towards the monitors from the interaction point, so that the effective minimum production angle seen by the monitors is $\theta_{prod} = 5.1$ mrad. On the other hand, beam-pipe elements before the monitor region define a window in such a way that the maximum acceptance angle in the x–z plane is $\theta_{prod} \approx 12$ mrad. In the x-direction this translates into an acceptance which is less than 2 cm wide.

7.4.1 Design

Each of the four counters consists of a sampling calorimeter made of tungsten converter sheets interspersed with sampling layers made of plastic scintillator and a plane of vertical silicon strips, as described below. The overall shape of the calorimeter is that of a rectangular box, 3 cm × 5 cm × 14 cm. The first tungsten layer is 4 radiation lengths thick (the radiation length for tungsten used in BCAL is 3.8 mm); this thickness is needed to protect the sampling layers from the high flux of synchrotron radiation photons. The next nine tungsten layers are each 2 radiation lengths thick. The ten sampling planes are made of 3 mm thick scintillators read in pairs by small 1 cm diameter photomultiplier tubes. A plane of vertical silicon strips (40 strips: 5 cm long, 0.5 mm pitch, and 300 μm thick) is located after the first 8 radiation lengths. Finally, a thick plate of tungsten, 6 radiation lengths, protects the sampling planes from synchrotron radiation photons entering the back of the calorimeter.

The main properties of BCAL are summarized in table 17.

7.5 Acceptances

A comparison of the geometrical acceptance of the three luminosity monitors is given in table 18, and a two-dimensional representation is shown in fig. 58.

8. THE TRIGGER SYSTEM

8.1 The trigger scheme

The ALEPH trigger system is designed to accept all genuine e^+e^- interactions. Given the luminosity of LEP and the corresponding event rate, no specific type of physics events needs to be selected—the trigger must only reduce the background to a manageable level, i.e. the frequency of triggers must be small enough to be acceptable for gating the TPC and to cause only minimal dead-time in the data acquisition.

The trigger scheme has to be rather flexible, since the properties and the rate of the background are not well known *a priori*. As experience shows, background conditions are unstable during fills and may vary with changes of parameters in the LEP storage ring. The main background for the trigger comes from beam-gas interactions and off-momentum beam particles hitting the edges of collimators or the vacuum chamber at, or in the vicinity of, the detector.

Signals from different ALEPH detector components allow for a variety of triggers which together cover all possible types of events. The basic philosophy for the design of the individual triggers was to be sensitive to single particles or single jets.

The ALEPH trigger system is based on three levels of refinement:

1. the Level-1 trigger, with a decision within about 5 μs (compared to 22 μs between two beam crossings),
2. the Level-2 trigger,with a decision within about 50 μs,
3. the Level-3 trigger, which is applied only after the readout.

The overall requirement for the trigger system is not to exceed the rate acceptable for data writing, i.e. 1–2 Hz. The Level-1 trigger initiates the event digitization. To keep the space-charge effects in the TPC small, the trigger rate should be at most a few hundred hertz. The Level-2 trigger refines the Level-1 track triggers and checks for the presence of charged-particle trajectories in the TPC originating from the vertex region. In case the Level-1 decision cannot be confirmed, the readout process is stopped and cleared. The maximum trigger rate allowed for Level 2 is about 10 Hz. The Level-3 trigger, which has access to the information from all detector components, identifies genuine e^+e^- interactions, separates them from background triggers, and validates them for recording on the storage medium.

As we will describe below, the excellent running conditions of the LEP machine from the start-up have led to Level-1 trigger rates of the order of 0.5 Hz at luminosities of 10^{30} cm^{-2} s^{-1}.

8.2 The Level-1 trigger

Four detector components play a major role in the trigger scheme: ITC, TPC, ECAL, HCAL. They cover the same solid angle of almost 4π. In the case of ECAL and HCAL, signals from the wires and from the pads, forming projective towers, are available.

The signal sources are grouped into 60 logical trigger segments for the HCAL and ECAL, as indicated in fig. 59, where the limits of the projective segments are shown on the outer surface of the hadron calorimeter. The subdivision follows closely the structure of the electromagnetic and hadronic calorimeters. In particular, the barrel section retains the subdivision into 12 segments of 30° in azimuth. The end-caps of both calorimeters are divided into 6 segments of 60°. The subdivision in polar angle is slightly more complex, because the size of segments decreases towards the incoming beams. A particular region is the junction of barrel and end-cap. In order to obtain the segmentation, signals from different modules have to be mixed. This can be seen from fig. 59, where the segment limits in polar angle are indicated.

In addition LCAL tower signals are used to trigger on forward Bhabha events in order to monitor the e^+e^- collision rate. These signals are grouped into 24 trigger segments.

The trigger electronics (fig. 60) sums the multitude of analog signals arriving from the calorimeters to obtain segment signals. Each of these sums is sent to four discriminators with remotely adjustable thresholds, so as to yield four YES/NO signals per trigger segment. The resulting digital signals are ordered into arrays of 60 bits. They are then fanned out to be available for the formation of physics triggers. In addition, a total energy signal is formed as well as energy signals for the central part (the barrel) and the two end-caps separately.

The analog sums at the discriminator inputs are digitized in ADCs and are read out together with all digital signals from the discriminators to monitor the performance and the efficiency of the subsequent physics trigger.

The layout of the various detector components provides different granularities to be used for triggering, i.e. segment, module, and total-energy signals. For the formation of physics triggers, the following source signals from the different detector components can be used:

- HCAL towers: 60 segments;
- HCAL wires: 24 direct module signals; or mapped onto 60 segments;
- ECAL towers: 60 segments;
- ECAL wires: 36 direct module signals; or mapped onto 60 segments;
- ITC pattern: track candidates in 60 ϕ segments;
- TPC pattern: track candidates in 60 θ-ϕ segments;
- LCAL towers: 2 × 12 overlapping segments.

A particular physics trigger (up to 32 can be defined) is obtained by establishing the trigger condition first in each segment and then ORing the segments. All these triggers are finally ORed to deliver a global Level-1 YES/NO decision.

8.3 The Level-2 trigger

The second-level trigger is based on hard-wired processors which look for tracks in the TPC from the beam intersection region [21]. As the lower transverse momentum limit set by the ITC in the first-level track trigger is 1 GeV/c, and as these tracks are essentially straight in the r–z plane in the TPC, the processors look for tracks in that plane. Tracks found by the second-level processors set bits in the 60-bit segment mask, and the second-level track trigger decision is made by replacing the ITC mask with the TPC mask.

Signals for the second-level trigger are provided by 1152 special pads situated between the rows of standard pads. There are eight trigger-pad rows in the inner zone and eleven in the outer zone where each trigger pad is 6 mm wide and covers an arc of 15° in ϕ. Signals from the trigger pads are amplified and shaped, using the standard TPC devices, before discrimination. The measured pad hit efficiency is greater than 99% and the timing jitter is equivalent to less than 4 mm r.m.s. in z.

The timing constraints on the second-level trigger are governed by the TPC drift time and the ECAL clearing time, which total 61 μs. For the case where the second level rejects a trigger, the experiment has to be ready to accept the third bunch crossing after the trigger, i.e. at 67 μs. The second-level decision to reject a trigger must therefore be made and broadcast to all parts of the experiment within about 6 μs of the end of the TPC drift time. To achieve this, the data are processed as they arrive during the drift-time period.

Twenty-four processors are used to search independently for tracks in six ϕ sectors in two radial zones of each end-plate. Processing of most events is completed before the end of drift, and a vertical track at the HV membrane is processed within 2.25 μs.

8.4 The Level-3 trigger

The third-level event selection is performed by an analysis process running within the data acquisition before the data are recorded. It acts on the complete set of digitizations of events passed through trigger levels 1 and 2.

In order to cope with the rate at which these events arrive, several copies of the process may be running in a battery of independent computers to which events are distributed in a round-robin fashion (the 'ALEPH event processor').

The event processor is located in the data-acquisition system at a place where all digitizations of an event are available. Parts of the final event reconstruction can therefore be anticipated in order to obtain sharper selection criteria as compared with the previous fast hard-wired triggers. In the design of the programs, emphasis has been put on high efficiency for pattern recognition and low CPU requirement, rather than on excellent reconstruction precision. Therefore, the need for high-level calibration of analog signals is avoided as much as possible. Reconstruction is done only for the parts of the detector showing activity to the Level-1 and Level-2 triggers; processing is stopped as soon as sufficient information on the good quality of a trigger is gathered. No effort is made (so far) to explicitly identify 'false' triggers in order to reject them, the reason being that genuine e^+e^- events may be overlaid with background signals and could be lost with an unpredictable rate.

8.5 The trigger performance

In the following, the physics triggers which were used in the 1989 runs, and the performance of the trigger will be discussed.

Annihilation events are triggered by two independent sets of Level-1 triggers:

1. Triggers based on the information from the ECAL wires and the ITC:
   a) total energy greater than 6.5 GeV in the central region (the barrel),
   b) total energy greater than 3.8 GeV in either of the two end-caps,
   c) total energy greater than 1.6 GeV in both end-caps in coincidence,
   d) ITC–ECAL coincidence, requiring a track candidate in the ITC (at least five out of eight planes fired) and an energy of at least 1.3 GeV in an ECAL module in the same azimuthal region,

with the additional coincidence requirement that the analog sums of the odd- and even-numbered wires planes both exceed half of the above-mentioned energies. This condition, together with the low electronics noise, allows to trigger on thresholds of few hundred MeV with acceptable trigger rates.

2. A trigger based on an ITC–HCAL coincidence, for penetrating particles, requiring a track candidate in the ITC and 4 out of 12 double planes of HCAL tubes in the same azimuthal region.

Luminosity (Bhabha) events are triggered also in different ways using LCAL tower signals:

1. a coincidence of 20 GeV deposited in an azimuthal segment on one side, with 16 GeV deposited on the other side, without azimuthal correlation requirement;
2. a single-arm requirement of 31 GeV deposited on either side;
3. prescaled single-arm triggers with 16 and 20 GeV thresholds to provide an estimate of the beam-related background.

In general, events were triggered by more than one trigger. Thanks to this redundancy, the trigger efficiency could be easily measured and was found to be 100% for hadronic Z^0 decays, close to 100% for leptonic Z^0 decays, and 99.7 ± 0.2% for Bhabha events.

As already mentioned, the overall trigger rate was 0.5 Hz for a typical luminosity of 10^{30} cm^{-2} s^{-1}. Despite the simple trigger requirements and the very low thresholds used, the data sample is strongly enriched in physics-related processes. In a sample of 538,472 triggers, taken at energies at, or close to, the Z^0 mass, we found about 28,592 hadronic Z^0 decays and 52,669 Bhabha events. The rest stems from beam-related muons (generated by beam–collimator interactions), beam–gas interactions, off-momentum electrons, cosmics, and finally electronic noise (mainly in the ECAL module trigger).

Additional triggers can be formed, such as:

- energy of at least about 1 GeV in an ECAL module without the coincidence requirement with the ITC (neutral electromagnetic trigger),
- trigger on HCAL towers and wires (neutral hadronic trigger),
- pure track triggers using the ITC (TPC).

Once higher luminosities are achieved, or if worse beam conditions occur, the triggers can be based on finer granularity (segments).

Under standard running conditions, 20% of Level-1 triggers are track-only triggers. Level 2 removes 75% of these, primarily beam–gas interactions, and reduces the track trigger proportion to approximately 6%.

The Level-3 trigger is tested and will be used for the 1990 runs.

9. DATA-ACQUISITION AND EVENT RECONSTRUCTION

9.1 Requirements

The modular structure of the detector requires a modular structure of the data-acquisition system and determines the way in which the various components are brought together. At the beginning of the design phase, it was decided that each subdetector group needs some autonomy, not

only during the development phase but also whilst bringing the complete detector into operation and whenever parallel activities are appropriate, for example during debugging or for calibration runs. Apart from small changes and some extensions, the system follows the guidelines given in ref. [22].

9.2 Readout architecture

The architecture adopted is a tree-like structure with a strong hierarchy (fig. 61). Following the data and/or control flow from the bunch crossing of the accelerator down to the storage device, we find the components that are listed below (figs. 61 and 62).

a) The Timing, the Trigger, and the Main Trigger Supervisor synchronize the readout electronics to the accelerator and inform the Readout Controllers (ROCs) about the availability of data. They also keep track of the proper protocol and synchronization of all controllers, and measure the dead-time of the experiment. The task of the Fan In/Out (FIO) units is to fan out timing and trigger signals to the ROCs and to combine BUSY and ACK signals from the ROCs, the logical function being programmable via look-up memories.

b) The ROCs initialize the front-end modules, read them out, format the data into standard banks, do first calibrations.

c) The EBs build a subevent at the level of each subdetector, do formatting if needed, and provide a 'spy event' to a subdetector computer.

d) The main EB (MEB) collects the pieces of an event from the various EBs, and ensures resynchronization and completeness.

e) The Event Processor, also called the 'Level-3 trigger', is a facility for refined data reduction.

f) The Main Host and subdetector computers. The main machine collects all data for storage, on-line analysis, event display, etc. It also provides the common services. The subdetector computers get the 'spy events' and perform the monitoring of the large subdetectors (TPC, ECAL, HCAL). During the stand-alone activities of these subdetectors, they are used as the 'main machine'.

g) Event Reconstruction, which is normally done 'off-line' in a computer centre. Preference was given to a solution where the event reconstruction would be done 'quasi on-line' at the experiment.

The functionality of all major system components, the protocols for data transfers, the handling of control signals, and the procedures for handling errors were defined before the components were built. A full 32-bit architecture was used throughout the complete data-acquisition chain knowing that the system would grow in the future. A single family of machines is employed.

The readout protocol devised for this system imposes a strong hierarchical control over the flow of data. Processing elements follow the principle of being a Master towards the detector and a Slave in the downstream direction, towards the main computer (fig. 61). This principle allows a missing processing element to be skipped by joining its input and output and by transferring the function to the next higher layer. It also means that there is no communication between components on the same readout level.

Another feature of this scheme is that multiple parallel data streams can be established, thus optimizing the processing and buffering to equalize the data flow. Synchronization on the detector side is achieved by connecting all ROCs to the same timing signals. On the host computer side, this is done by using an event-building stage that accepts only data belonging to the same event. Spy channels have been added to allow data handling in parallel with the main data stream.

Another key feature of the readout architecture is called 'partitioning'; this permits any subset of the data-acquisition system to be configured such that it can function independently of the rest of the system. This is achieved by allowing the selection of any combination of ROCs to take part in data-taking (fig. 62) and is implemented by programming the FIO units such that only those ROCs

contained in the partition receive the trigger signals. This partitioning scheme is presented in detail elsewhere [23].

9.3 Implementation of the architecture

Figure 63 gives an overview of the entire readout system. A number of standards have been chosen for implementing the architecture. We use almost exclusively FASTBUS for data acquisition, apart from some small amounts of CAMAC and NIM units. The VME standard is used only for some communication equipment. A sophisticated FASTBUS database is used to keep track of the detector configuration, and to define devices, segments, routing tables, broadcast trees, service request routing, and so on. It is also used to initialize the system.

For embedded processors, the 680x0 family of microprocessors was selected with one exception (bit-slice processor). They run the OS-9 operating system and have a connection to thin-wire Ethernet. The network connection was originally introduced to provide a secondary path to the processing nodes. System-wide microprocessor support and data-acquisition control has been established with a centralized OS-9 disk server, a remote log-in facility, and task-to-task communication with the host computers [24].

The last major component of the system is a VAX cluster, consisting of four BI-based machines, one VAX 8700 serving as the main data-acquisition computer and supporting most of the services, and three VAX 8200/8250 machines used by the larger subdetectors TPC, ECAL, and HCAL. These machines have their own connection to FASTBUS via an optical link [25] bridging the distance of 400 m to the first FASTBUS equipment, where a high-performance interface [26] developed for ALEPH is attached to an EB [27]. Figure 64 shows the central FASTBUS crate and its dual data path to the main VAX; one path provides the readout, the other serves as a direct general interface to the FASTBUS system. The real-time performance of the VAX 8700 has been boosted by adding the 'Event Processor', which consists of 11 real-time front-end microVAX CPU cards residing directly on one BI bus. The data from the MEB are routed under the control of one control processor directly, event by event, to one of 10 data processors. Events passing this filter are moved to the memory of the VAX 8700 for subsequent treatment and storage [28]. Some 20 VAX work stations are connected via Ethernet to the same cluster, and all machines share the disk and tape drives. Data are divided between all CPUs in the main cluster via disk-based global sections; synchronization is achieved using the distributed lock manager.

The above choices leave us with only two CPU architectures: 680x0 and VAX. The number conversion is done at the boundary between the two systems. In the case of FASTBUS, the conversion takes place inside the FASTBUS-to-VAX interface. For Ethernet, the conversion could be done on either side.

9.4 Data reduction

The reduction of the raw-data volume is achieved simultaneously with two methods: i) by decreasing the rate with the help of the trigger; ii) by compacting the data through 'zero suppression' and on-line calibration.

Starting from a bunch-crossing rate of almost 50 kHz, the Level-1 trigger will generate rates of less than 500 Hz. The decision time is less than 5 μs, which means that there is no dead-time. With each Level-1 YES decision, the data conversion in the front-end modules (ADCs, TDCs, etc.) proceeds. At the end of the TPC drift-time, a Level-2 trigger based on TPC track information is available. The decision time is 45 μs, enough to match the TPC drift-time, and short enough to miss only the next bunch crossing. With a Level-2 NO, data conversion is aborted, and the trigger is ready for the fourth bunch crossing. The Level-2 trigger leads to a trigger rate of less than 10 Hz. This frequency determines the data collection rate. The last step in rate reduction takes place in the Event

Processor, where one hopes to distinguish real physics events from background events by comparing the information from the trigger system with the event data. This last stage should bring the rate down to the rate of interesting collisions ($\sim$ 1 Hz).

Reducing the data volume per event is equally important. The first and most effective measure is the 'zero suppression'. For the bulk of the readout channels, this is done in the hardware by comparing the measured analog value with a preloaded threshold. For digital channels, the addresses of the channels hit are recorded. The next step takes place in the readout controllers, where formatting and calibrations are done. This does not necessarily reduce the amount of data, but greatly reduces the computing time needed later. It should be noted that the raw computer power embedded in the electronics is of the order of 100 Mips, and exceeds by far the power of the on-line computers. The event building does not reduce data, but data consistency checks are done.

9.5 Performance

The system was exposed to real data for the first time during the pilot run in August 1989. The LEP machine started with low luminosity, and the background conditions were much better than expected. As a result the Level-1 trigger rate ($\sim$ 1 Hz) was much lower than had been predicted. On the other hand, the average event size is about five times higher, ranging from some 30 Kbytes for random triggers to several 100 Kbytes for Z^0 events. Once all data reduction algorithms have been applied, we expect the event size to be significantly smaller.

The Level-2 trigger was tested and commissioned during the first data-taking runs and was fully operational (i.e. rejecting events) during the final running period of 1989. The Level-3 trigger has been fully commissioned under real data-taking conditions but has not yet been used to reject events. The overall performance of the system has met the design goals and, with the integration of the Level-2 and Level-3 triggers, the system is able to cope with the data rate expected at full LEP luminosity.

9.6 Event reconstruction

The event reconstruction is not done off-line in a computer centre, but by coupling a dedicated computing system, the ALEPH Event Reconstruction Facility [29] to the main data-acquisition computer through shared disks (Fig. 65). A microVAX 3600 serves as host for a Local Area VAX cluster of diskless VAX station 3100 CPUs, and controls three dual-ported RA90 1.2 Gbytes disks, where the second port is connected to the data-acquisition VAX cluster via an HSC50 controller. The disks are alternatively mounted on both systems under software control, and raw-data files written to a disk by the data-acquisition are made available to the Event Reconstruction Facility shortly after the end of the run.

A preliminary scan of the data is performed by the microVAX in order to produce an Event Directory containing the address of each event within the file, as well as constants for the reconstruction program. Contiguous subsets of events are then assigned for reconstruction in each of the VAX work stations in parallel, exploiting the fact that events are independent from one another. Each of the 12 processors runs a full operating system (VMS) and the full ALEPH reconstruction program. The event subsets are efficiently accessed by using random access to the disk over Ethernet based on the addresses in the Event Directory, a feature built into the reconstruction program and widely exploited in the off-line analysis environment as well. Custom-tuning of the operating system parameters provides relatively high input/output bandwidth over the Ethernet (500 Kbytes/s) and results in high CPU utilization efficiency (98%).

The results of the reconstruction are written by the processors to separate disk files, which are joined into a single file on the microVAX. The order of the events on output is preserved by construction. The reconstruction output files are immediately transmitted to the off-line computers

construction. The reconstruction output files are immediately transmitted to the off-line computers through a Vitalink bridge, which interconnects the Ethernet of the reconstruction system and the CERN computer center. The protocols used are TCP/IP to the CERN IBM system and the Distributed File System for the ALEPH off-line VAX cluster, both with speeds in the 70 Kbytes/s range. The reconstruction output is stored on large disk subsystems and written to magnetic cartridges for distribution to participating institutes within 24 hours of data acquisition.

10. INITIAL PERFORMANCE OF THE DETECTOR AT LEP

Detector construction has been completed in August 1989. After an initial pilot run in August, the first physics data were recorded between September and December with LEP operating between 44.5 and 47.5 GeV beam energy and at luminosities up to 4.5×10^{30} cm^{-2} s^{-1}. The trigger rates were around 1 Hz. Among the 538472 events recorded, there were 52669 small-angle Bhabha scatterings detected in the luminosity calorimeter, and 28592 hadronic Z^0 decays. Figure 66 shows one such Z^0 decay into hadrons. The performance of the apparatus was good from the early stages and this has led to first physics results in October 1989.

Acknowledgements

The construction of this large detector system was made possible by the efforts of many technical collaborators at the participating institutes and at CERN. We would like to express our appreciation to all of them. In particular, we thank the technical staff of the following laboratories and universities for constructing and implementing the different parts of the detector: for the superconducting coil and cryogenics (STIPE, CEN-Saclay, CERN); for the iron yoke, the support structure, and the gas system (CERN); for the ITC (IC London); for the TPC (CERN, Glasgow, Mainz, MPI Munich, Pisa, Trieste, Wisconsin); for the ECAL barrel detectors (Clermont-Ferrand, École Polytechnique, Marseille, LAL-Orsay, STIPE, CEN-Saclay); for the ECAL end-caps (Glasgow, Lancaster, Royal Holloway & Bedford College, RAL Chilton, Sheffield); for the LCAL (NBI Copenhagen); for the SATR (Siegen); for the BCAL (Barcelona); for the HCAL (Bari, Frascati, Pisa); for the muon chambers (Beijing, Bari, Frascati, Pisa); for the level-1 trigger (Heidelberg) and for the data acquisition system (CERN).

REFERENCES

[1] J.M. Baze et al., IEEE Trans. Magn. **34** (2) (1988).

[2] J. Le Bars et al., IEEE Trans. Magn. MAG-23 (2) (1987).

[3] L. Bauerdick, G. Petrucci and G. Stefanini, The field in the ALEPH magnet, ALEPH 88-034, Note 88-005 (1988).

[4] G.J. Barber et al., Nucl. Instrum. Methods **A279** (1989) 212.

[5] T. Barczewski et al., ALEPH 89-159, submitted to Nucl. Instrum. Methods (1989).

[6] P. Némethy et al., Nucl. Instrum. Methods **212** (1983) 273;
D.R. Nygren, Phys. Scr. **23** (1981) 584.

[7] S.R. Amendolia et al., Nucl. Instrum. Methods **A234** (1985) 47.

[8] S.R. Amendolia et al., Nucl. Instrum. Methods **A239** (1985) 192.

[9] S.R. Amendolia et al., Nucl. Instrum. Methods **A252** (1986) 403.

[10] G. Hubricht et al., Nucl. Instrum. Methods **228** (1985) 327 and **A243** (1986) 495.
C. Raine et al., Nucl. Instrum. Methods **217** (1983) 305.

[11] S.R. Amendolia et al., Nucl. Instrum. Methods **A252** (1986) 392.

[12] S.R. Amendolia et al., Nucl. Instrum. Methods **A217** (1983) 317.

[13] W. Blum et al., Nucl. Instrum. Methods **A252** (1986) 407.

[14] S.R. Amendolia et al., Nucl. Instrum. Methods **A244** (1986) 516.

[15] M. Bardadin-Otwinowska et al., Electromagnetic calorimeter response to muons and non-interacting pions, ALEPH 89-2/EMCAL 89-1 (1989).

[16] G. Bagliesi et al., Nucl. Instrum. Methods **A286** (1990) 61.

[17] B. Pignard, Thesis, Univ. Paris VII (1990).

[18] E. Iarocci, Nucl. Instrum. Methods **217** (1983) 30.

[19] G. Bagliesi et al., Nucl. Instrum. Methods **A268** (1988) 144.

[20] M.G. Catanesi et al., Nucl. Instrum. Methods **A247** (1986) 438.

[21] T. Medcalf et al., Nucl. Instrum. Methods **A277** (1989) 358.

[22] ALEPH Dataflow Group, ALEPH Data Acquisition System Hardware Functional Specifications, ALEPH DATACQ note 85-21 (1985).

[23] J.F. Renardy, IEEE Trans. Nucl. Sci. **NS-36** (1989) 1464.

[24] T. Charity, IEEE Trans. Nucl. Sci. **NS-36** (1989) 1726.

[25] R.A. McLaren et al., IEEE Trans. Nucl. Sci. **NS-36** (1989) 1449.

[26] A. Miotto, IEEE Trans. Nucl. Sci. **NS-36** (1989) 1452.

[27] A. Marchioro et al., IEEE Trans. Nucl. Sci. **NS-35** (1988) 316.

[28] B. Jost, IEEE Trans. Nucl. Sci. **NS-36** (1989) 1580.

[29] M. Delfino et al., Univ. Aut. Barcelona preprint LFAE-89-01 (April 1989), submitted to 'Computing in High-Energy Physics', Oxford, UK, 1989.

Table 1
Characteristics of the ALEPH solenoid

Inner cryostat diameter	4960 mm	
Outer cryostat diameter	5840 mm	
Overall cryostat length	7000 mm	
Main winding:		
Mean diameter	5300 mm	
Winding length	6350 mm	
Number of turns (uniformly distributed)	1532	
Compensating coils (at both ends of the solenoid)		
Two sections per coil	Section 1	Section 2
Mean diameter	5450 mm	
Axial distance of coil centre	2840 mm	3102 mm
Winding length	188 mm	188 mm
Number of turns	45	45
Total number of turns	1712	
Nominal current	5000 A	
Nominal field (with iron)	1.5 T	
Stored energy (with iron)	136 MJ	
Thickness of coil and cryostat		
Absorption length	$0.4\lambda_{abs}$	
Radiation length	$1.6X_0$	
Weight of coil and cryostats	55 t	
Refrigeration power	100 W at 4.2 K	
	2400 W at 80 K	

Table 2
Basic ITC parameters

Active length of chamber	2.00 m
Inner wall:	
Inner radius	128 mm
Thickness	2 mm
Composition	Polystyrene/aluminium foil
Radiation length	0.2%
Outer wall:	
Inner radius	285 mm
Thickness	2 mm
Composition	Carbon fibre
Radiation length	1.0%
No. of layers	8
Wires:	
960 sense wires	Gold-plated tungsten, 30 μm diameter
3840 field wires	Gold-plated aluminium, 147 μm diameter
Wire sagitta	120 μm
Gas:	
50% argon + 50% ethane or 80% argon + 20% carbon dioxide	

Table 3
Mechanical parameters of the TPC and gas properties

Dimensions:

Radius:	
R_{outer}	1.8 m
R_{inner}	0.31 m
Overall length	4.7 m
Drift length	2 × 2.2 m
Weight	3.6 t (with cables)
Gas volume	43 m^3
Radiation length:	
inner field cage	$0.023X_0$
outer field cage	$0.048X_0$
Sectors:	

Sectors	R_{min} (cm)	R_{max} (cm)	No. of pad rows	No. of trig. pad rows	No. of wires
Type K	38	91	9	8	148
Type W, M	100	170	12	11	196

Pad size	6.2 × 30 mm^2
Pitch in r-ϕ	6.7 mm
Trigger-pad size	6.8 mm × 15°
Sense-wire spacing	4 mm
Sense-wire diameter	20 μm
Field-wire diameter	127 μm
Diameter of other wires	76 μm

Gas properties:

Composition	Ar (91%) + CH_4 (9%) at STP
Drift velocity	5.2 cm/μs
Longitudinal diffusion	4 mm/$\sqrt{m}$ per single electron
Transverse diffusion (B = 15 kG)	0.8 mm/$\sqrt{m}$ per single electron
Specific ionization for m.i.p. (mean)	90 electrons per centimetre
Attenuation	< 1.5% per metre of drift length

Table 4
Characteristics of the TPC wire grids

Grid	Distance ± tolerance from pad plane (mm)	Wire spacing (mm)	Material	Diameter (mm)	Stringing tension (N)
Sense	4 ± 0.05	4[a)]	W + 3% Rh[b)]	0.020	0.5
Field	4 ± 0.05	4[a)]	Cu + 2% Be[b)]	0.127	3
Cathode	8 ± 0.05	1	Cu + 2% Be	0.076	1.2
Gating	14 ± 0.1	2	Cu + 2% Be	0.076	1.2

a) Field wires are interleaved with sense wires; distance sense–field wire = 2 mm.
b) The sense and field wires are gold-plated.

Table 5
Number of electronic components in the TPC readout system
(TPD: time projection digitizer, TPP: time projection processor)

		Sector type			Σ	12 × Σ
		K	W	M		
Pads	Pads	909	1182	1326	3417	41004
	Boards	57	74	83	214	2568
	TPDs	15	19	21	55	660
	TPPs	1	1	1	3	36
Wires	Wires	148	190	190	528	6336
	Boards	10	12	12	34	408
	TPDs	3	3	3	9	108
	TPPs	1	1	1	3	36

Table 6
Characteristics of TPC electronics

Sampling rate of digitization	11.4 MHz
Pulse width of shaped signal (FWHM)	300 ns (1 m drift)
Electronic errors for:	
calibration (channel versus channel)	gain = 1%
	time = 6 ns
rϕ-measurement (total)	$\leqslant$ 70 μm
z-measurement (total)	$\leqslant$ 0.5 mm

Table 7
Expected space resolution (μm)
from the TPC at B = 1.5 T for
a high-momentum track

ℓ	α		
(m)	$-30°$	0°	30°
0.04	80	150	230
1	95	130	180
2	105	130	170

Table 8
Performance properties of the TPC

rϕ spatial resolution: 160 μm at 0° pad crossing angle			
	400 μm at 10° pad crossing angle		
z spatial resolution at θ =	90°	45°	20°
per pad row:	0.7 mm	1.7 mm	2.3 mm
per wire:	3 mm	2 mm	2 mm

Momentum resolution $\Delta p/p^2 \approx 1.5 \times 10^{-3}$ (GeV/c)$^{-1}$

dE/dX resolution: 4.5% for 280 wires

Table 9
Arrangement of pads in a pad plane of an ECAL petal

Inclusive pad row	Number of pads across petal	ϕ angle subtended by each pad
1- 8	8	$2\pi/96$
9–24	16	$2\pi/192$
25–40	24	$2\pi/288$
41–50	32	$2\pi/384$

Table 10
Components of the ECAL electronics

	Barrel	End-caps
Number of pad channels	147456	73728
Number of wire channels	540	1080
Number of ADC modules	102	54
Number of sequencer modules	6	2
Number of readout controllers	6	2

Table 11
Measurement precision of ECAL electronics

Measurement precision/channel	Pads	Wires
Charge (fC)	40	20
Energy (MeV)	6.4	1

Table 12

ECAL calibration constants from ^{83}Kr sources and electron beam for barrel module 8 and petal 3

	Barrel 8	Petal 3	Ratio Barrel/Petal
Working conditions:			
HT (V)	1361	1365	
p (mbar)	1003	982	
T (K)	297	295	
^{55}Fe peak (counts)	148.8	150.0	
^{83}Kr parameter (fC)	2320 ± 10	2270 ± 10	
Equalized gas gain using ^{55}Fe:			
C_M pads (fC/MeV)	6.62 ± 0.1	6.31 ± 0.1	1.05 ± 0.02
C_M wires (fC/MeV)	19.09 ± 0.30	18.40 ± 0.25	1.040 ± 0.015
^{83}Kr parameter (MeV equiv.)	121.5 ± 0.8	123.4 ± 1.5	0.985 ± 0.015

Table 13

Parameters of the electromagnetic calorimeter

Description

A sampling calorimeter with alternate layers of lead and proportional tubes, located inside the superconducting magnet coil. There are 45 layers, grouped in 3 stacks. The wire chambers are made of Al-extrusion, covered with graphite-coated Mylar. Signals are derived from the cathode pads and the wires. Cathode pads are arranged in projective towers, 49152 in the barrel and 24576 in the end-caps, read out in 3 storeys.

The gas is Xe (80%) + CO_2 (20%).

Dimensions and performance

Al proportional tubes, active cross-section	3.2×4.5 mm^2	
Anode wires (gold-plated tungsten), diameter	25 μm	
Average tower solid angle	1.67×10^{-4} sr	
Operating gas pressure: mean atmospheric pressure + 50 mbar:	990 mbar	
Operating temperature, required precision	± 0.5 °C	
Energy resolution σ_E/E	0.18 GeV$^{1/2}/\sqrt{E}$	
Position resolution $\sigma_x = \sigma_y$	6.8 mm GeV$^{1/2}/\sqrt{E}$	
Granularity at $\theta = 90°$ (barrel)	17×17 (mrad)^2	
Granularity at $\theta = 45°$ (barrel)	12×12 (mrad)^2	
Granularity at $\theta = 40°$ (end-cap)	9×10 (mrad)^2	
Granularity at $\theta = 27°$ (end-cap)	10×14 (mrad)^2	
	Barrel	End-caps
Number of modules	12	12×2
Number of layers, stack 1 (2 mm Pb)	10 ($3.83X_0$)	10 ($3.46X_0$)
Number of layers, stack 2 (2 mm Pb)	23 ($8.80X_0$)	23 ($8.86X_0$)
Number of layers, stack 3 (4 mm Pb)	12 ($8.85X_0$)	12 ($8.91X_0$)
Inner radius (cm)	184.7	54
Outer radius (cm)	225.4	234.8
Thickness (cm)	40.7	56.25
Weight per module (tons)	10.4	2.6
No. of anode wires	115404	118800×2
Wire length (cm)	463.0	8–174
Measured uniformity of response over one module (%)	1.3–1.6	1–1.5
Angular coverage in θ (deg.)	40–140	13–41 139–167
Average fraction of insensitivity (% of solid angle)	2	6

Table 14

Parameters of the Hadron Calorimeter and the Muon Detector

Description

The magnet iron is instrumented with 23 layers of plastic (limited-)streamer tubes, separated by iron sheets 5 cm thick. The tubes layers are equipped with pad readout, summed in towers for a localized measurement of the total deposited energy. Each tube is also coupled capacitatively to strips parallel to the wires. It is their hit pattern that is read out. Wire information is read out plane by plane (end-caps) and two planes by two planes (barrel) and used for the trigger.

Outside of the magnet, behind the last layer (10 cm) of the HCAL, two double-layers of streamer tubes form the muon detector. Each single layer reads out two orthogonal coordinates using strips.

Dimensions and performance

Angular size of towers (larger in ϕ at small θ)	$3.7° \times 3.7°$
Number of towers	4788
Total iron depth of a tower near $\theta = 90°$, $\phi = 0°$	120 cm
Typical accuracy of energy measurement σ_E/E	$0.84\ GeV^{-1/2}/\sqrt{E}$
Typical spatial accuracy Δ for strip coordinate measurements (perpendicular to the strip direction)	0.35 cm
Total number of muon chambers	94
Distance between muon chamber double layers:	
barrel and middle-angle chambers	50cm
end-cap chambers	40 cm
Typical accuracy σ_{θ_x} of muon exit angle measurement	10 mrad
Typical misidentification probability	
to take a π for a μ	0.7%
to take a K for a μ	1.6%
Fraction of solid angle covered by the sensitive part of the muon chambers above 15°:	
inner layer	92%
outer layer	85%

Table 15
Parameters of SATR

Description

Nine layers of drift tubes made of brass. The detector is subdivided into four modules. Each module is a half-cylinder containing 504 drift cells.

Gas: 90% Ar + 10% CO_2 with an admixture of 1% isopropanol.

Dimensions:

R_{inner}	92 mm (active part $\geqslant$ 99.5 mm)
R_{outer}	300 mm (active part $\leqslant$ 256.8 mm)
Distance from IP	Δz = 2455 mm
Length	Δz = 170 mm
Cross-section of drift cells	9.95 × 9.95 mm^2
Length of drift tubes	from 76.8 mm to 192.7 mm
Total radiation length	$0.68X_0$

Readout:

Single-hit electronics, measuring drift time to 1 ns

2016 wires in total ORed into 1152 readout channels.

Performance:

Position resolution of one drift tube: $\sigma_r = (320 \pm 20)\ \mu m$

Angular resolution of the entire chamber: $\sigma_\theta = 0.08$ mrad

Overall track-reconstruction efficiency : 99%.

Table 16

Parameters of LCAL

Description:

A sampling calorimeter, comprising lead sheets and wire chambers of 38 layers, grouped in 3 stacks of 9, 20, and 9 layers. It consists of four modules placed pairwise around the beam pipe. Each module is a half-cyclinder segmented into 384 towers in projective geometry. The design follows closely the one of ECAL.

Dimensions

R_{inner}	10 cm
R_{outer}	52 cm
Distance from IP	$\Delta z = 262.5$ cm
Length	$\Delta z = 42.5$ cm
Thickness of Pb plates	2.8 mm (stacks 1 + 2), 5.6 mm (stack 3)
Tower size at front face	2.9×2.9 cm^2
Radiation length per stack	$4.8X_0$, $10.6X_0$, $9.3X_0$
Front face	aluminium, 40 mm thickness

Readout:

Three pulse-height signals for each of the 1536 towers (384 per module) and one pulse-height signal for each of the 152 wire planes (38 per module).

Performance:

Energy resolution $\sigma_E = 0.014\,E + 0.20\sqrt{E}$ (E in GeV)

Position resolution $\sigma_x = \sigma_y = 1.4$ mm.

Table 17

Parameters of BCAL

Description:

A sampling calorimeter for relative luminosity measurements. Made of 10 tungsten converter sheets interspaced with 10 layers of plastic scintillator and 1 plane of silicon strips. Organized in 4 box-shaped modules, one pair upstream, one pair downstream of IP.

Dimensions:

External dimensions of each module	$(\Delta x, \Delta y, \Delta z) = (3, 5, 14)$ cm
Distance from IP	7.8 m
Distance between active area and beam	6.5 cm

Readout:

Twenty PM pulse heights, 160 silicon strips readout with Amplex chips.

Performance:

Efficiency approx. 75% for a cut in energy at 60% of total energy.

Table 18

Acceptance parameters of the luminosity monitors

	SATR	LCAL	SATR + LCAL	BCAL*)
Polar-angle acceptance limits (mrad)	40–90	55–155	55–90	5–10
Azimuthal-angle acceptance interval (deg)	360	330	330	220
Accepted cross-section for Bhabhas near the Z^0 (μb)	0.063	0.033	0.025	0.67

*) With mini-β quadrupoles switched on.

Figure captions

Fig. 1: The ALEPH detector, perspective view.

Fig. 2: ALEPH detector, longitudinal cross-section.

Fig. 3: ALEPH detector, lateral cross-section.

Fig. 4: Main field component: B_z versus z at three radii and fixed azimuth.

Fig. 5: The radial component and the line integral of the ratio B_r/B_z.

Fig. 6: Azimuthal field component: line integral of B_ϕ/B_z along the z-axis, from z to the next TPC end-plate, at different azimuthal angles and for two radii.

Fig. 7: Cross-section through the ITC.

Fig. 8: The ITC drift cell.

Fig. 9: The measured r-ϕ resolution of the ITC.

Fig. 10: TPC overall view.

Fig. 11: TPC electrode structure.

Fig. 12: a) Overall geometry of the TPC end-plate.
b) A more detailed view of the M, W, and K sectors (see text).

Fig. 13: Mechanical details of the sector design.

Fig. 14: Schematic diagram of a sector edge, showing wire attachment, pad plane, wire grids, and potential strips.

Fig. 15: Architecture of the TPC readout system (SI = segment interconnect, EB = event builder, TPP = time projection processor, TPD = time projection digitizer, CCC = crate coupling card).

Fig. 16: Functional diagram of preamplifier and analog-to-digital conversion circuits (Time Projection Digitizer, TPD) for signals from TPC wires or anode pads.

Fig. 17: Gating grid of the TPC with electric field lines: a) gate open, b) gate closed.

Fig. 18: Transparency of the gating grid for electrons in the presence of a magnetic field, plotted as a function of ΔV_g. The transparency for ions is independent of the magnetic field and coincides with the one for electrons at B = 0.

Fig. 19: The optical path of the laser beam.

Fig. 20: The four double mirrors and the pentaprism mounted on the inner field cage; the aperture for the incident beam is 15 mm.

Fig. 21: TPC event display with ionization tracks from laser beams at six different azimuthal angles.

Fig. 22: Definition of angles between track, wire, and pad.

Fig. 23: The function f(cos θ) that determines the momentum resolution as a function of the polar angle θ.

Fig. 24: a) dE/dx versus momentum p (GeV) for tracks (electrons, pions, kaons, and protons) from Z^0 decays; b) dE/dx for pions with $0.3 < p < 0.6$ GeV/c (left) and Bhabha electrons (right) at 90 GeV c.m. energy; the resolution of the electron peak is σ/mean = 4.5%.

Fig. 25: Invariant two-pion mass in hadronic Z^0 decay events, showing a K^0 mass peak.

Fig. 26: The ratio of beam momentum p_{beam} over (charge Q $\times$ particle momentum p) measured in the TPC, for events of the type $e^+e^- \rightarrow \mu^+\mu^-$ and $e^+e^- \rightarrow e^+e^-$, at a c.m. energy of 90 GeV.

Fig. 27: Electromagnetic calorimeter (ECAL), overall view.

Fig. 28: Typical layer in the electromagnetic calorimeter stack.

Fig. 29: Barrel module of ECAL; the length of the module is 4.7 m.

Fig. 30: End-cap module of ECAL, called 'petal'; the radial dimension of the sector is 1.78 m.

Fig. 31: One channel of the analog electronics chain of the ECAL.

Fig. 32: Architecture of the ECAL pulse-height electronics readout (ADC = analog-to-digital converter, SEQ = sequencer, ROC = readout controller, SI = segment interconnect, EB = event builder, EVI = event builder-to-VAX interface).

Fig. 33: Barycentre reconstruction in θ and ϕ angles as a function of the hit coordinates θ_0 and ϕ_0.

Fig. 34: Angular resolution for 10 GeV electrons in the ECAL.

Fig. 35: Energy dependence of the angular resolution in ECAL.

Fig. 36: Energy resolution of the ECAL barrel.

Fig. 37: Energy resolution for electrons in the ECAL end-caps. The horizontal scale is in units of $(GeV)^{-1/2}$ and the vertical one in per cent.

Fig. 38: Energy response of the ECAL to 10 GeV electrons and pions.

Fig. 39: Fractional energy deposit in the four leading towers around a pion or electron track.

Fig. 40: Compactness R2 = E_4/p plotted versus longitudinal shower parameter R3 for hadronic Z^0 decays. Electrons show up as a cluster at R2 = R3 = 0.

Fig. 41: Pulse-height spectra from radioactive ^{83}Kr gas; a) from the wires, b) from the pads in ECAL.

Fig. 42: Comparison of response as a function of the polar angle θ for electrons, for radioactive gas and for cosmic muons (ECAL barrel module 8).

Fig. 43: Overall geometry of the hadron calorimeter (HCAL) surrounding the superconducting coil and the electromagnetic calorimeter.

Fig. 44: HCAL barrel module with notches.

Fig. 45: Tower geometry, a) in the polar angle, b) in the θ–ϕ plane.

Fig. 46: HCAL end-cap module.

Fig. 47: Cross-sectional view of the muon chambers and their (hardware) identification numbers: a) barrel, b) middle-angle, c) end-cap.

Fig. 48: Overview of the analog electronics for HCAL.

Fig. 49: Overview of the digital readout system for HCAL.

Fig. 50: Layout of the HCAL data acquisition system (HCP = hadron calorimeter processor, SI = segment interconnect, EB = event builder, EVI = event builder-to-VAX interface, TS = trigger supervisor).

Fig. 51: a) Charge distribution for 20 GeV pions and muons;
b) charge response and energy resolution for pions at a polar angle of 60°.

Fig. 52: Typical digital pattern of tubes hit by a 10 GeV pion (a), muon (b), and electron (c).

Fig. 53: One half of the main luminosity monitor consisting of SATR and LCAL. The outer radius of LCAL is 52 cm.

Fig. 54: One half of the small-angle luminosity monitor BCAL, each half consisting of two small calorimeters on the sides of the elliptical beam pipe.

Fig. 55: Side view of SATR, and details of the mounting of SATR on the front-plate of the luminosity calorimeter. Dimensions in mm.

Fig. 56: The sensitive area of the upper half of a module of the luminosity calorimeter LCAL. The volume extends from z = 266.8 cm to z = 302.2 cm from the interaction point.

Fig. 57: View of the ALEPH detector area showing the approximate position of the BCAL monitor.

Fig. 58: Acceptance in the θ–ϕ plane of the three ALEPH luminosity monitors. The shaded areas are the ones where the Bhabha electron track enters or leaves the monitors on the side face.

Fig. 59: An overview of the division of the ALEPH detector into trigger segments of projective geometry.

Fig. 60: The principle of the Level-1 and Level-2 trigger electronics.

Fig. 61: Basic readout architecture.

Fig. 62: General control and data flow in ALEPH.

Fig. 63: Overview of ALEPH readout.

Fig. 64: Top level readout and interface to Main VAX.

Fig. 65: Block diagram of the ALEPH Event Reconstruction Facility.

Fig. 66: A hadronic Z^0 decay in the ALEPH detector: a) x–y view, b) r–z view.

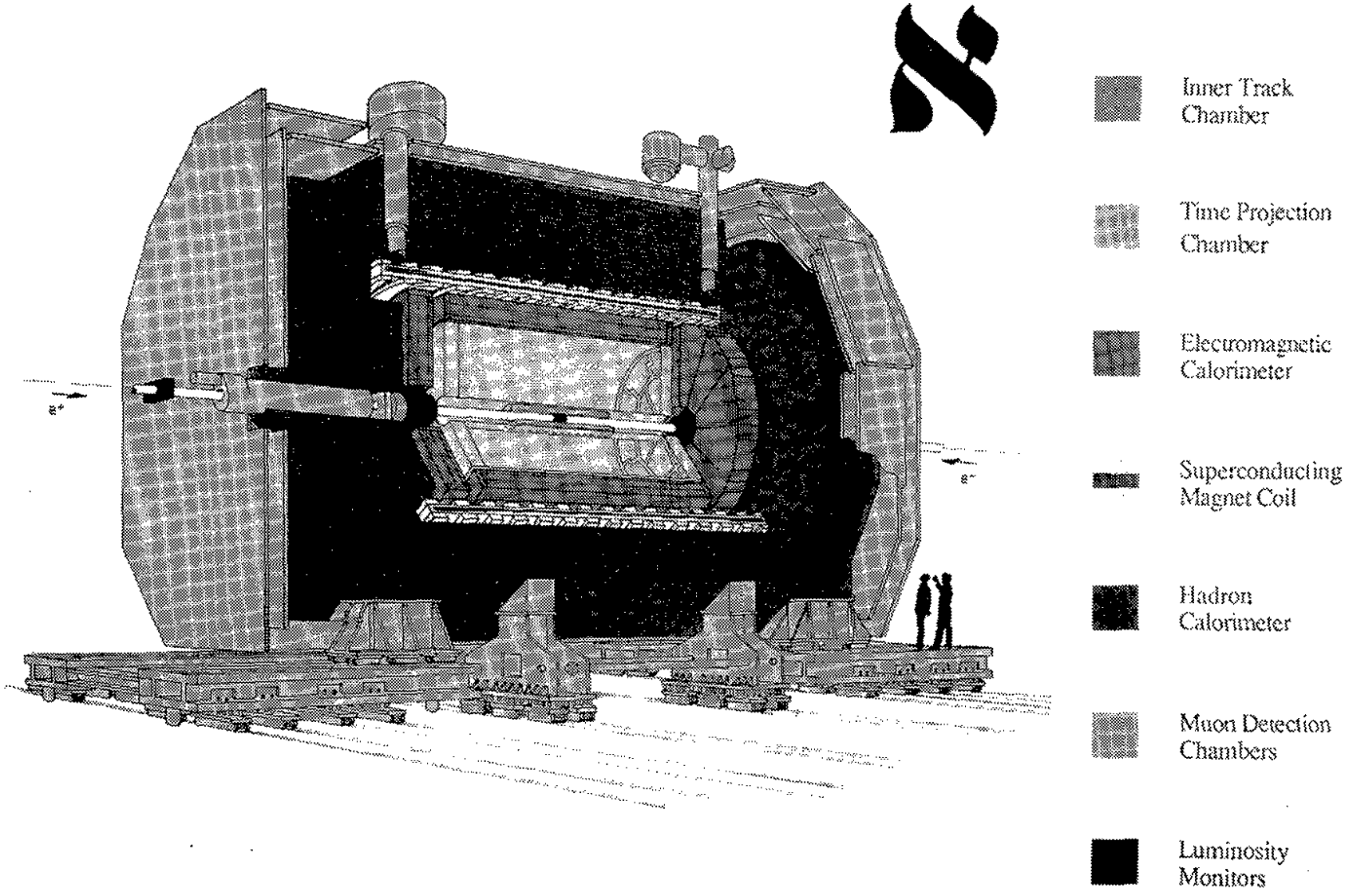
Vertex Detector
Inner Track Chamber
Time Projection Chamber
Electromagnetic Calorimeter
Superconducting Magnet Coil
Hadron Calorimeter
Muon Detection Chambers
Luminosity Monitors

Fig. 1

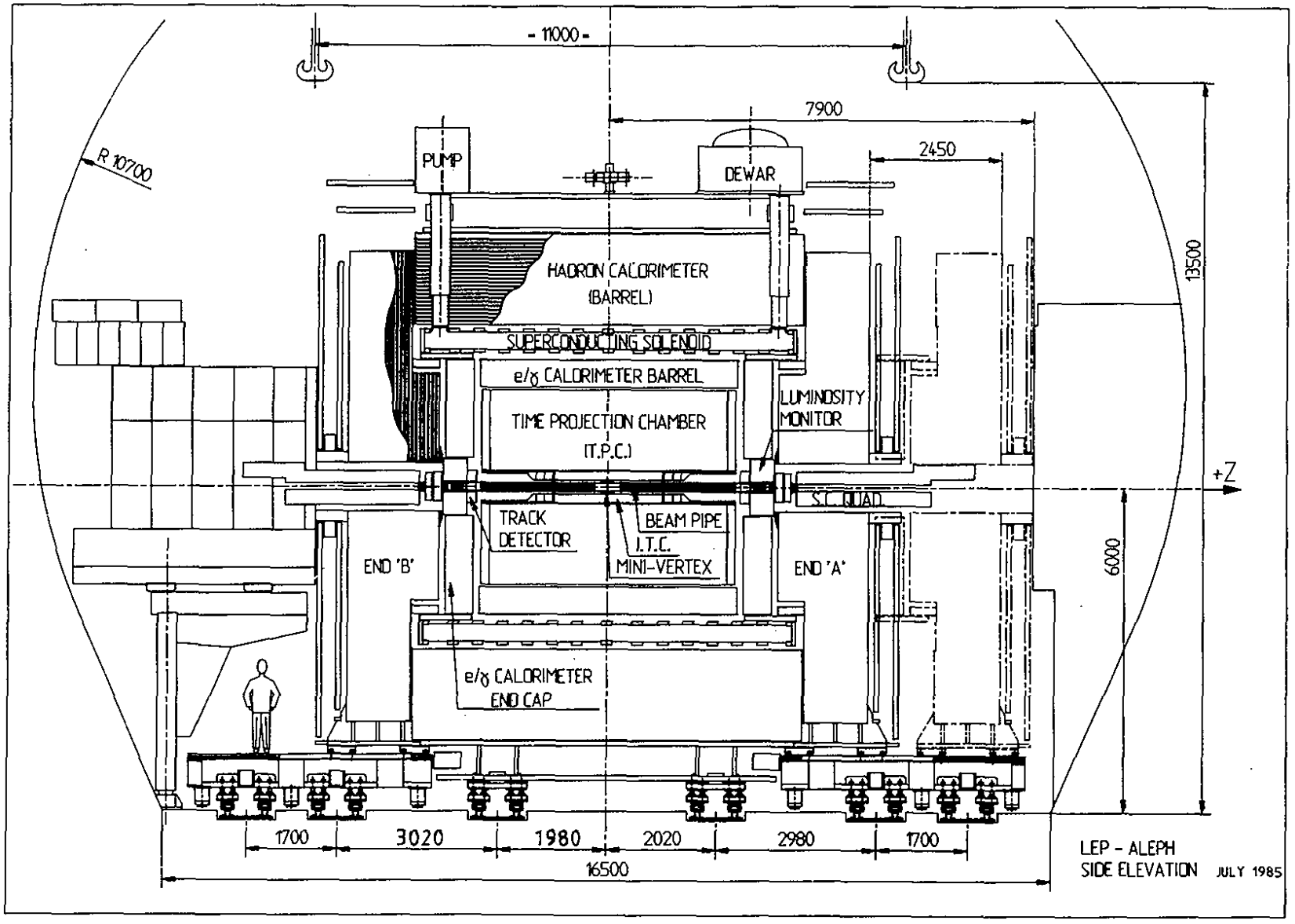
- 11000 -
7900
2450
R 10700
PUMP
DEWAR
HADRON CALORIMETER
(BARREL)
SUPERCONDUCTING SOLENOID
e/γ CALORIMETER BARREL
TIME PROJECTION CHAMBER
(T.P.C.)
LUMINOSITY
MONITOR
+Z
S.C. QUAD
TRACK
DETECTOR
BEAM PIPE
I.T.C.
MINI-VERTEX
END 'B'
END 'A'
e/γ CALORIMETER
END CAP
13500
6000
1700
3020
1980
2020
2980
1700
16500
LEP - ALEPH
SIDE ELEVATION
JULY 1985

Fig. 2

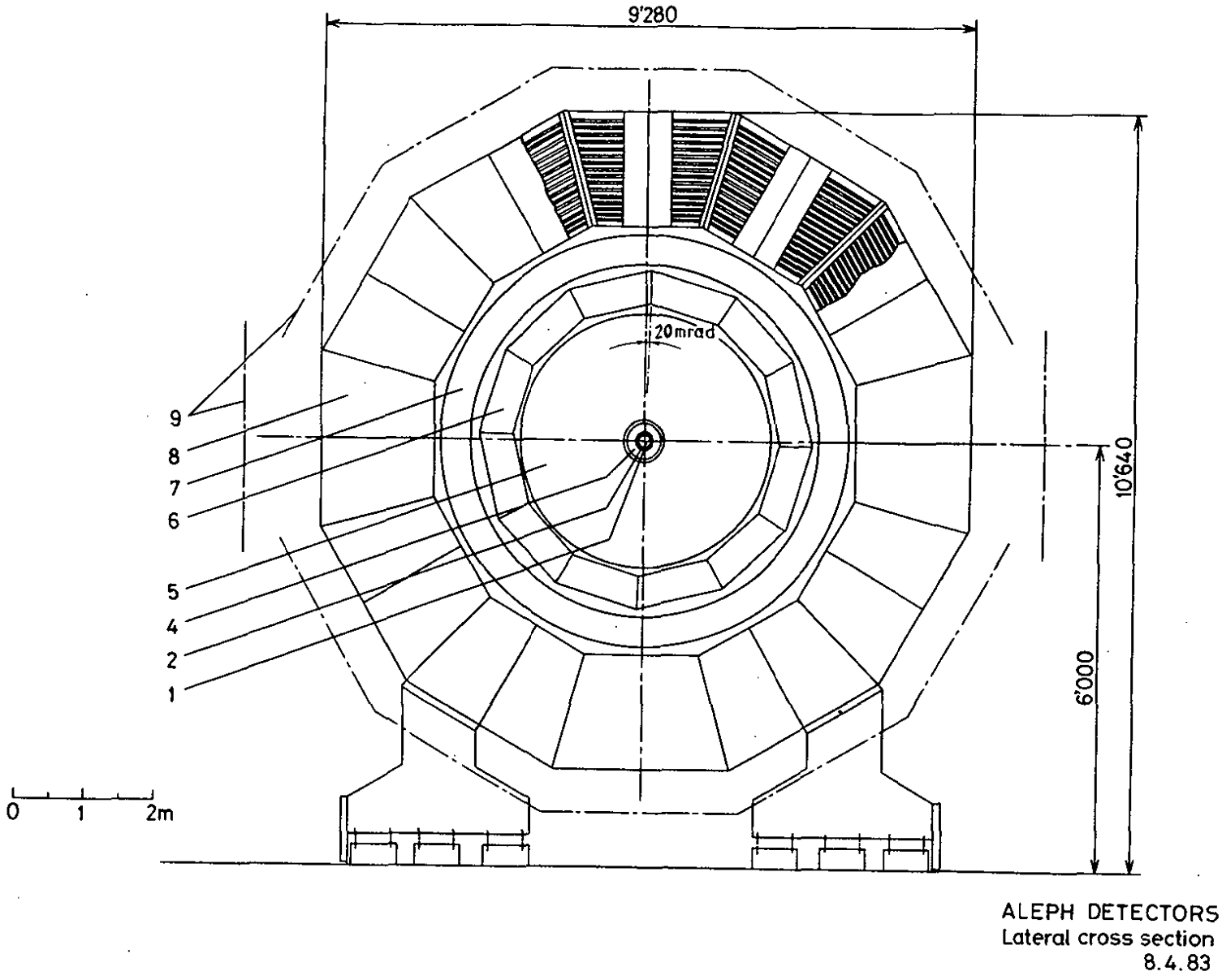
9'280
20mrad
9
8
7
6
5
4
2
1
10'640
6'000
0
1
2m
ALEPH DETECTORS
Lateral cross section
8.4.83

Fig. 3

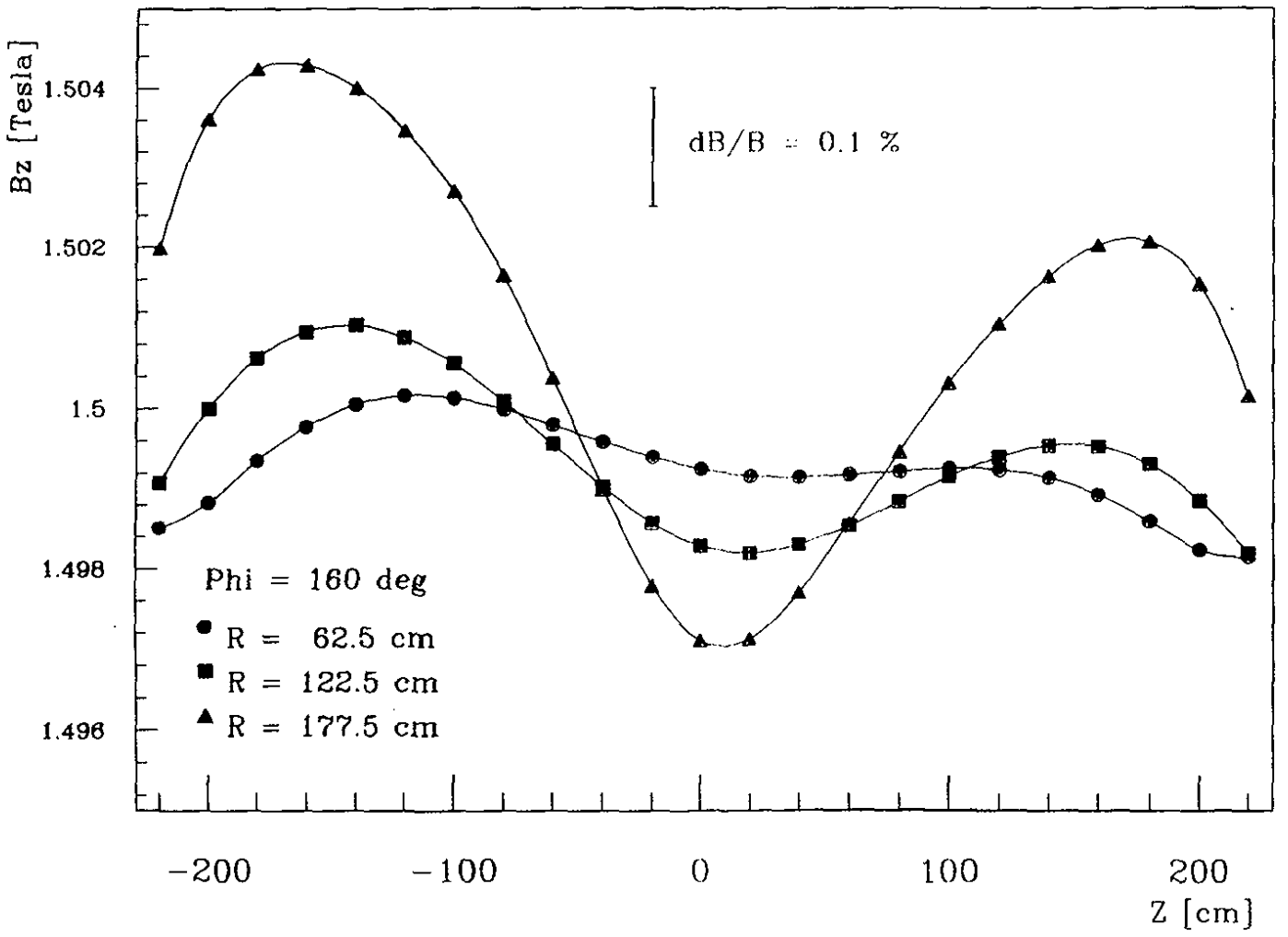
Bz [Tesla]
1.504
1.502
1.5
1.498
1.496
dB/B = 0.1 %
Phi = 160 deg
R = 62.5 cm
R = 122.5 cm
R = 177.5 cm
-200
-100
0
100
200
Z [cm]

Fig. 4

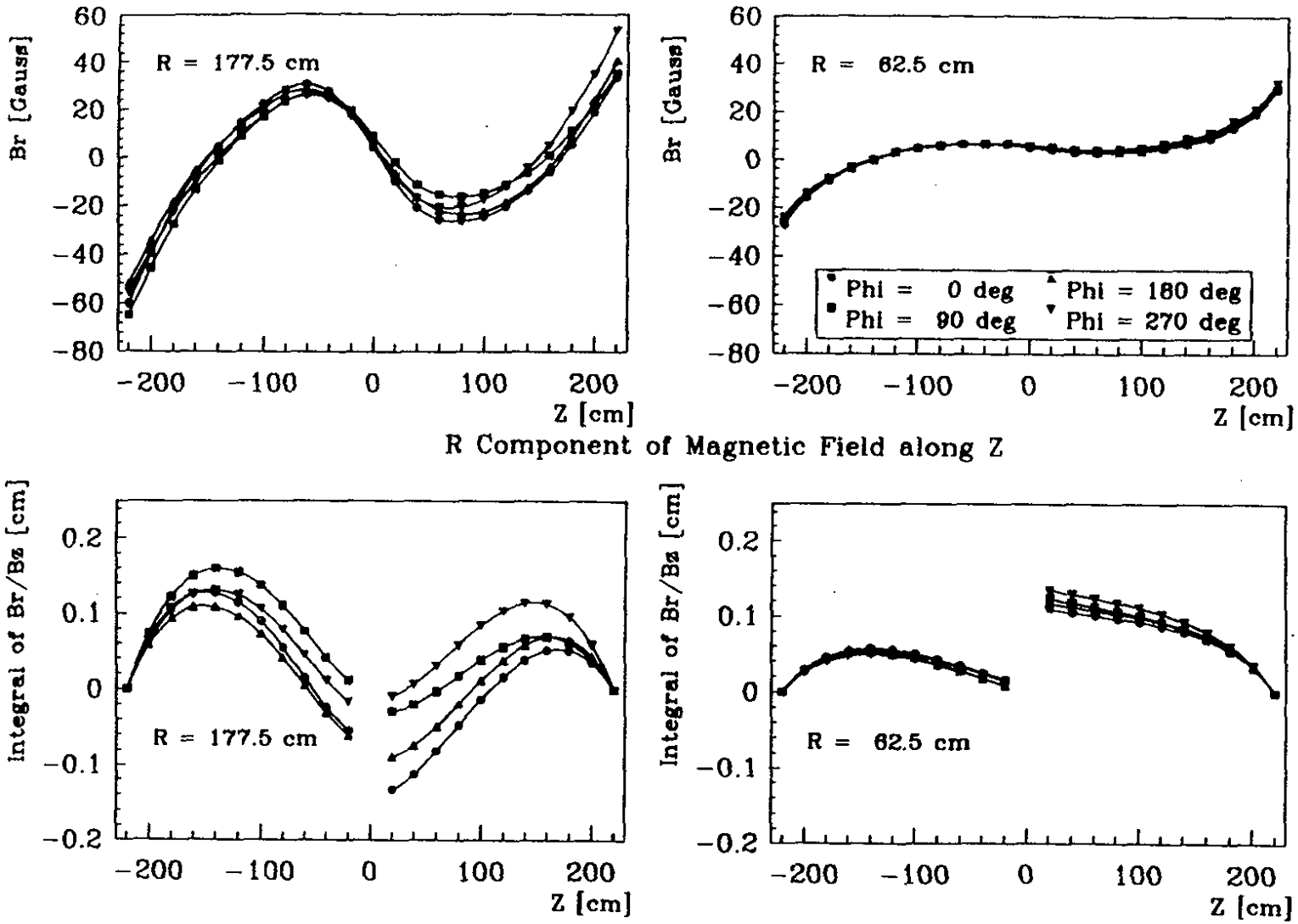
R = 177.5 cm
R = 62.5 cm
Br [Gauss]
Z [cm]
Phi = 0 deg
Phi = 90 deg
Phi = 180 deg
Phi = 270 deg
R Component of Magnetic Field along Z
Integral of Br/Bz [cm]

Fig. 5

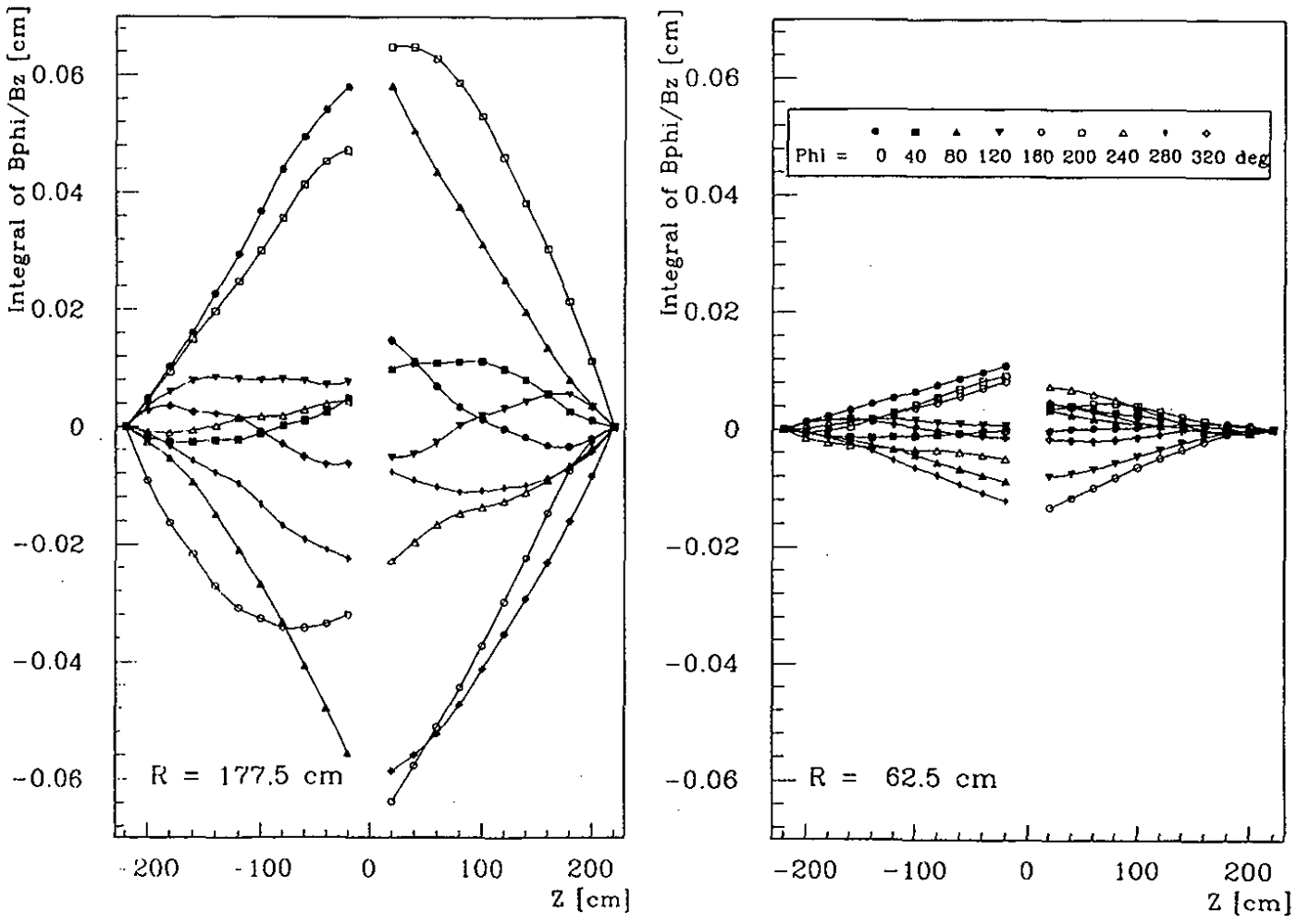
Integral of Bphi/Bz [cm]
0.06
0.04
0.02
0
-0.02
-0.04
-0.06
R = 177.5 cm
-200
-100
0
100
200
Z [cm]
Integral of Bphi/Bz [cm]
Phi = 0 40 80 120 160 200 240 280 320 deg
R = 62.5 cm
-200
-100
0
100
200
Z [cm]

Fig. 6

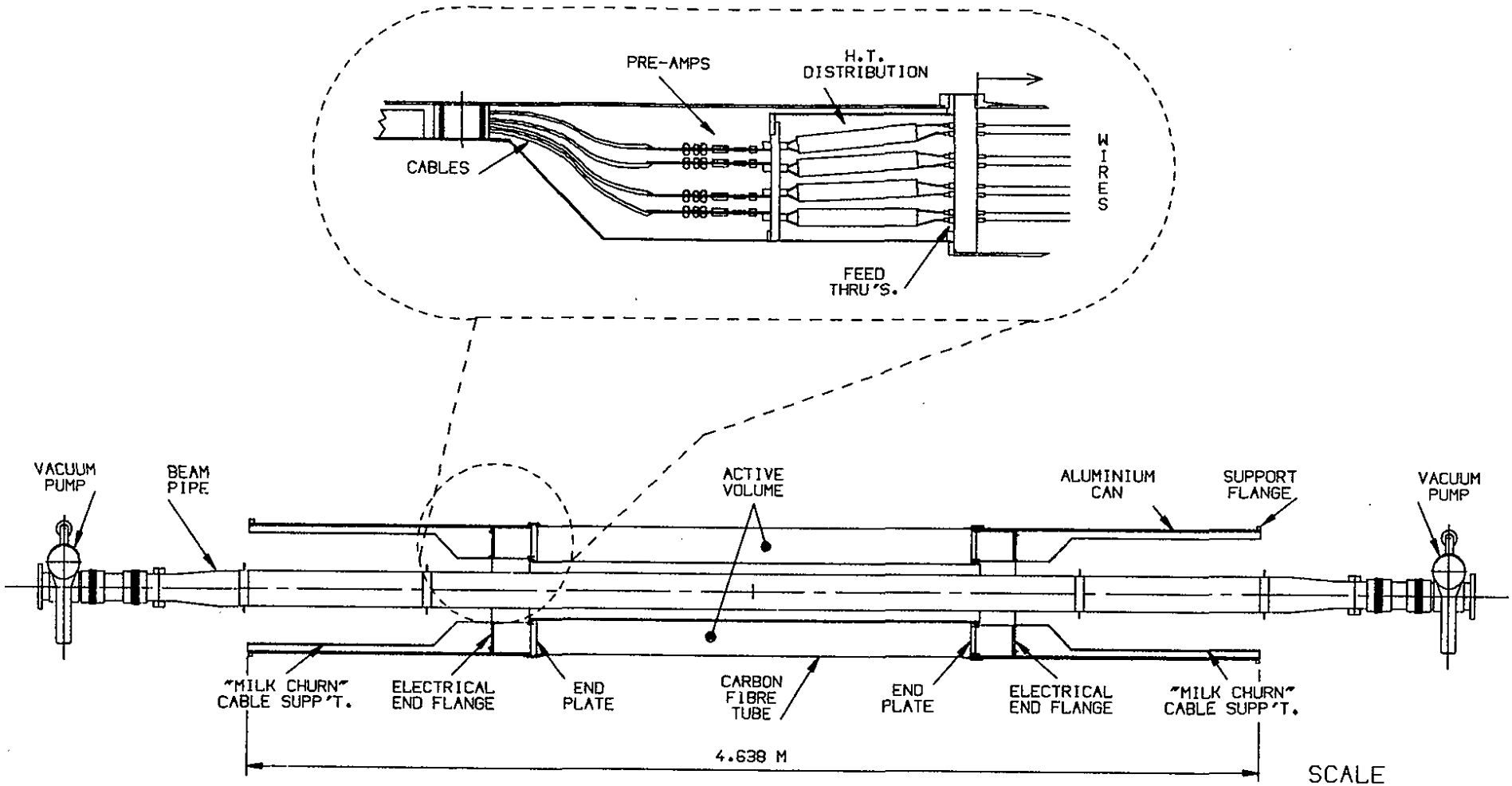
PRE-AMPS
H.T.
DISTRIBUTION
CABLES
WIRES
FEED
THRU'S.
VACUUM
PUMP
BEAM
PIPE
ACTIVE
VOLUME
ALUMINIUM
CAN
SUPPORT
FLANGE
VACUUM
PUMP
"MILK CHURN"
CABLE SUPP'T.
ELECTRICAL
END FLANGE
END
PLATE
CARBON
FIBRE
TUBE
END
PLATE
ELECTRICAL
END FLANGE
"MILK CHURN"
CABLE SUPP'T.
4.638 M
SCALE

Fig. 7

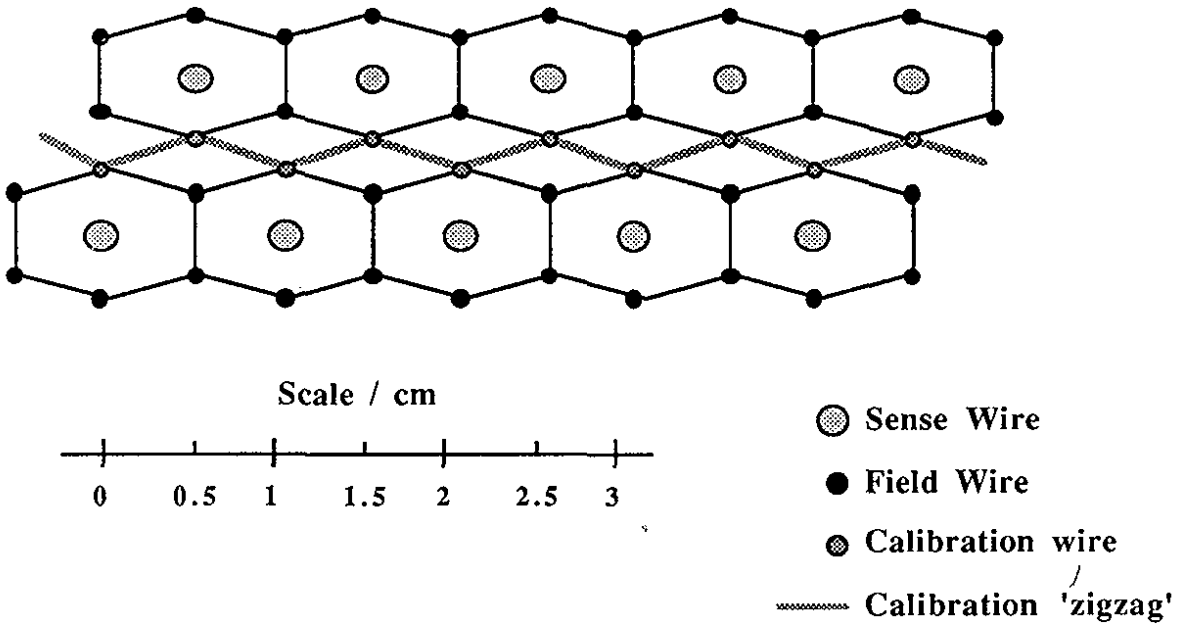
Scale / cm
0
0.5
1
1.5
2
2.5
3
Sense Wire
Field Wire
Calibration wire
Calibration 'zigzag'

Fig. 8

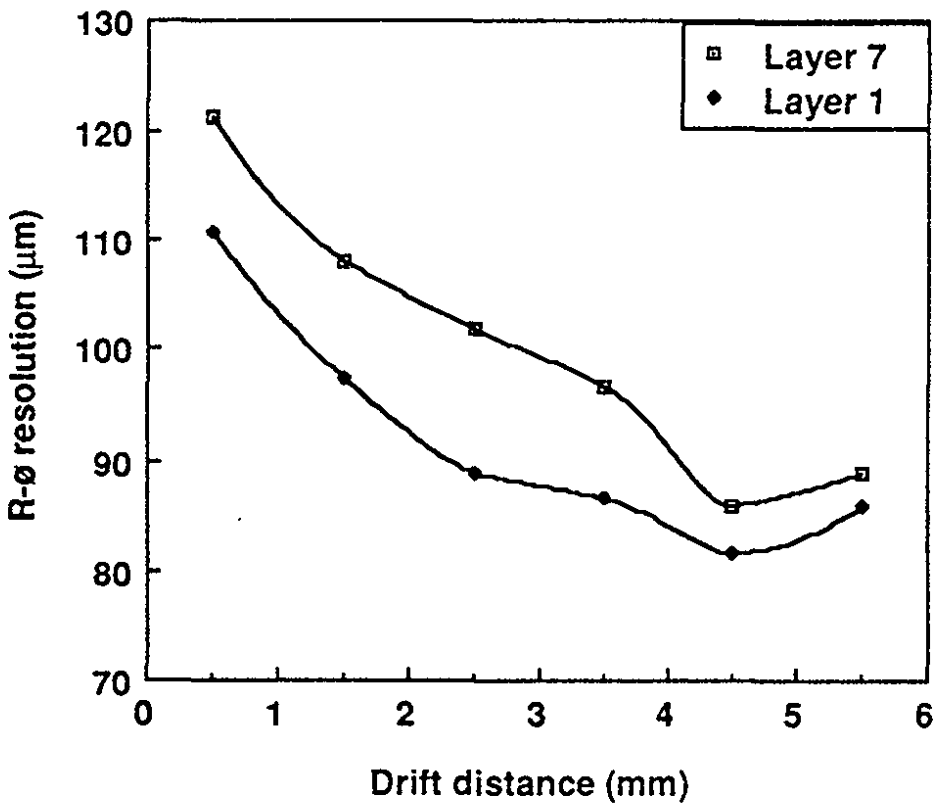
Layer 7
Layer 1
R-ø resolution (μm)
130
120
110
100
90
80
70
0
1
2
3
4
5
6
Drift distance (mm)

Fig. 9

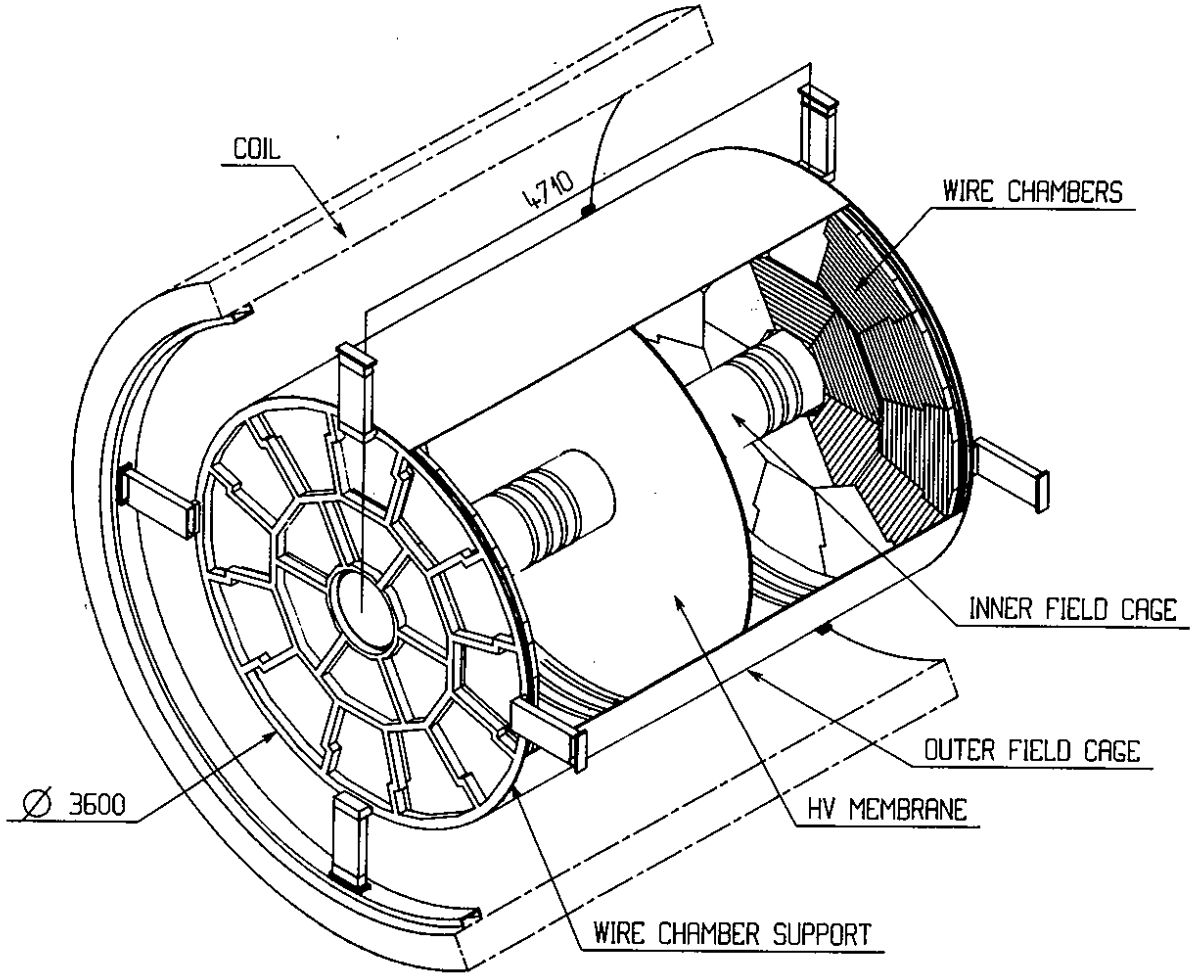
COIL
4710
WIRE CHAMBERS
INNER FIELD CAGE
OUTER FIELD CAGE
HV MEMBRANE
WIRE CHAMBER SUPPORT
∅ 3600

Fig. 10

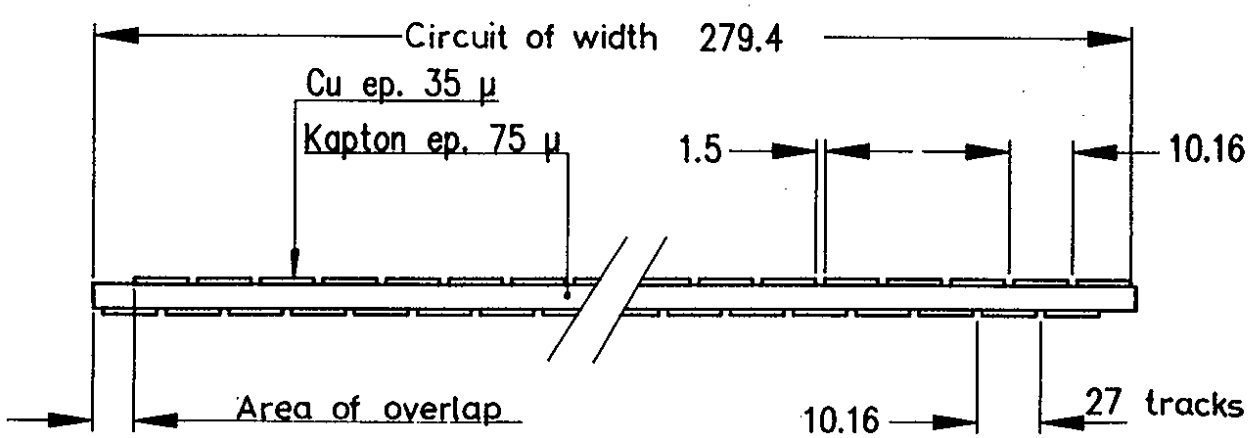
Circuit of width 279.4
Cu ep. 35 μ
Kapton ep. 75 μ
1.5
10.16
Area of overlap
10.16
27 tracks

Fig. 11

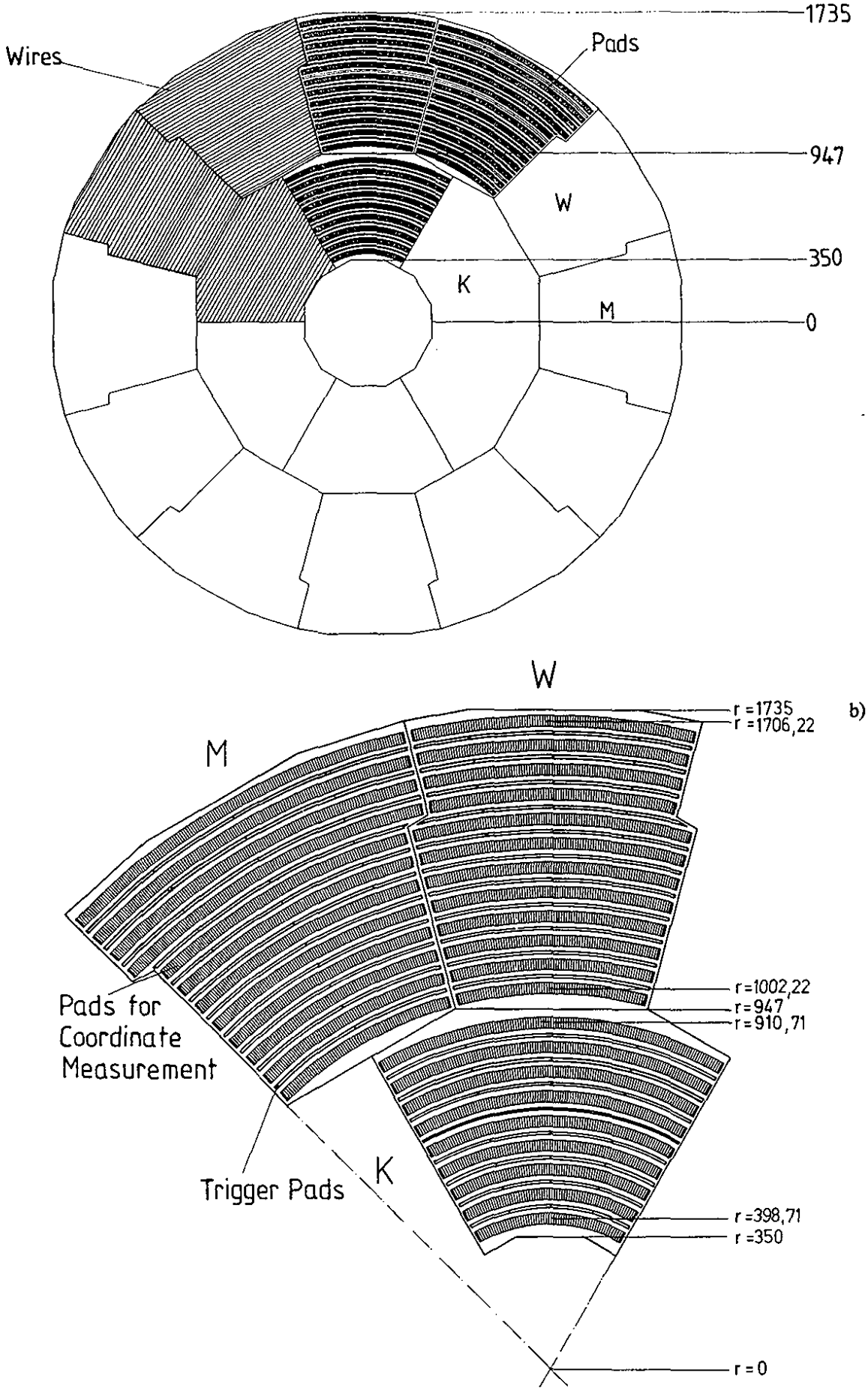
a)
1735
Wires
Pads
947
W
350
K
M
0
W
b)
r =1735
r =1706,22
M
r =1002,22
r =947
r =910,71
Pads for
Coordinate
Measurement
Trigger Pads
K
r =398,71
r =350
r = 0

Fig. 12

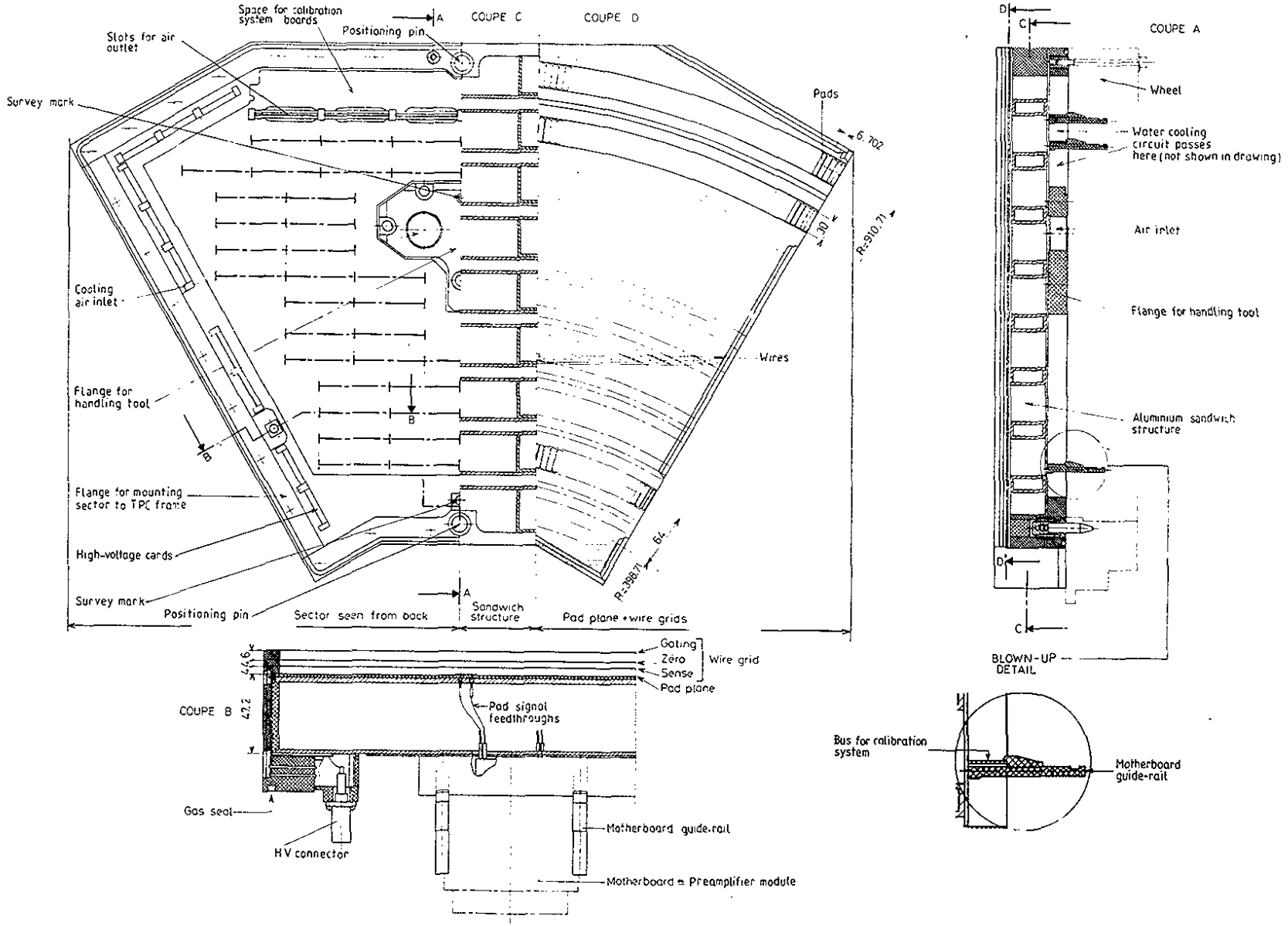
Space for calibration system boards
Slots for air outlet
Positioning pin
A
COUPE C
COUPE D
Survey mark
Pads
6.702
30
R=910.71
Cooling air inlet
Wires
Flange for handling tool
B
Flange for mounting sector to TPC frame
High-voltage cards
Survey mark
Positioning pin
Sector seen from back
Sandwich structure
Pad plane + wire grids
R=398.71
64
Gating
Zero
Sense
Wire grid
Pad plane
6.6
47.2
COUPE B
Pad signal feedthroughs
Gas seal
HV connector
Motherboard guide-rail
Motherboard + Preamplifier module
D
C
COUPE A
Wheel
Water cooling circuit passes here (not shown in drawing)
Air inlet
Flange for handling tool
Aluminium sandwich structure
D'
C
BLOWN-UP DETAIL
Bus for calibration system
Motherboard guide-rail

Fig. 13

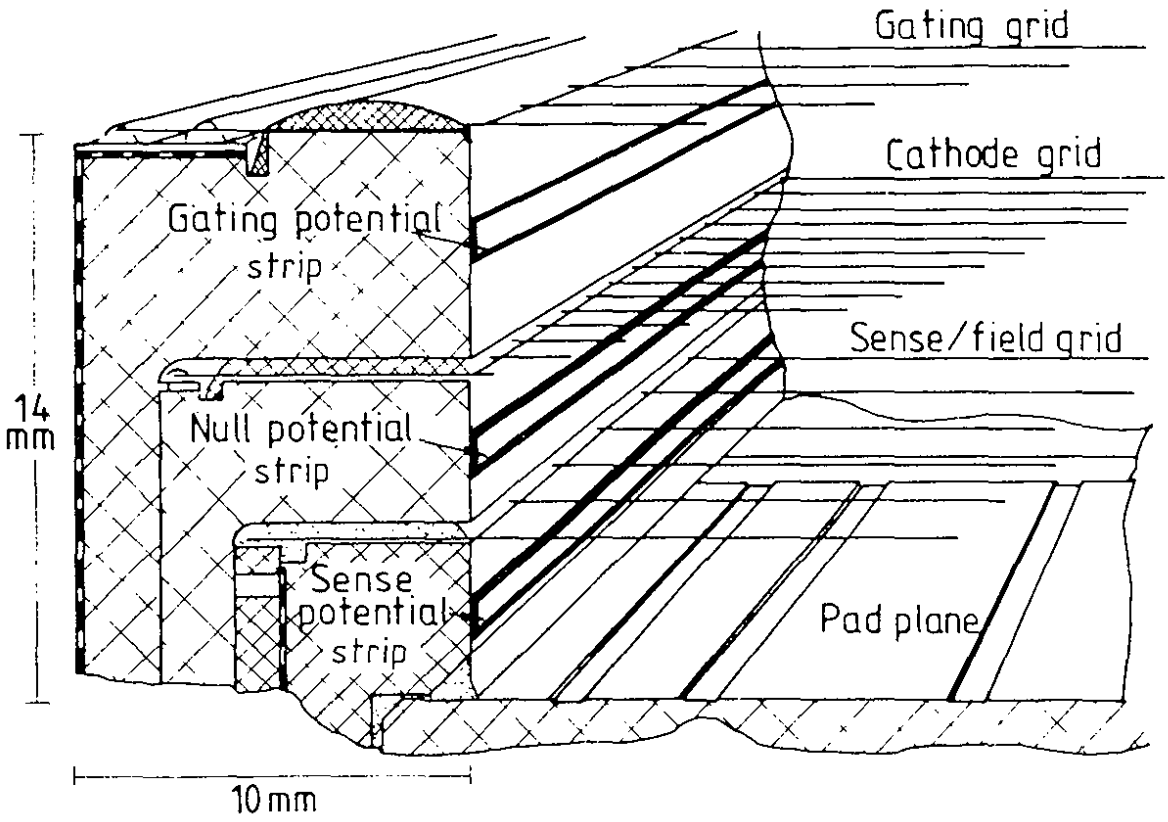
Gating grid
Cathode grid
Gating potential strip
Sense/field grid
14 mm
Null potential strip
Sense potential strip
Pad plane
10 mm

Fig. 14

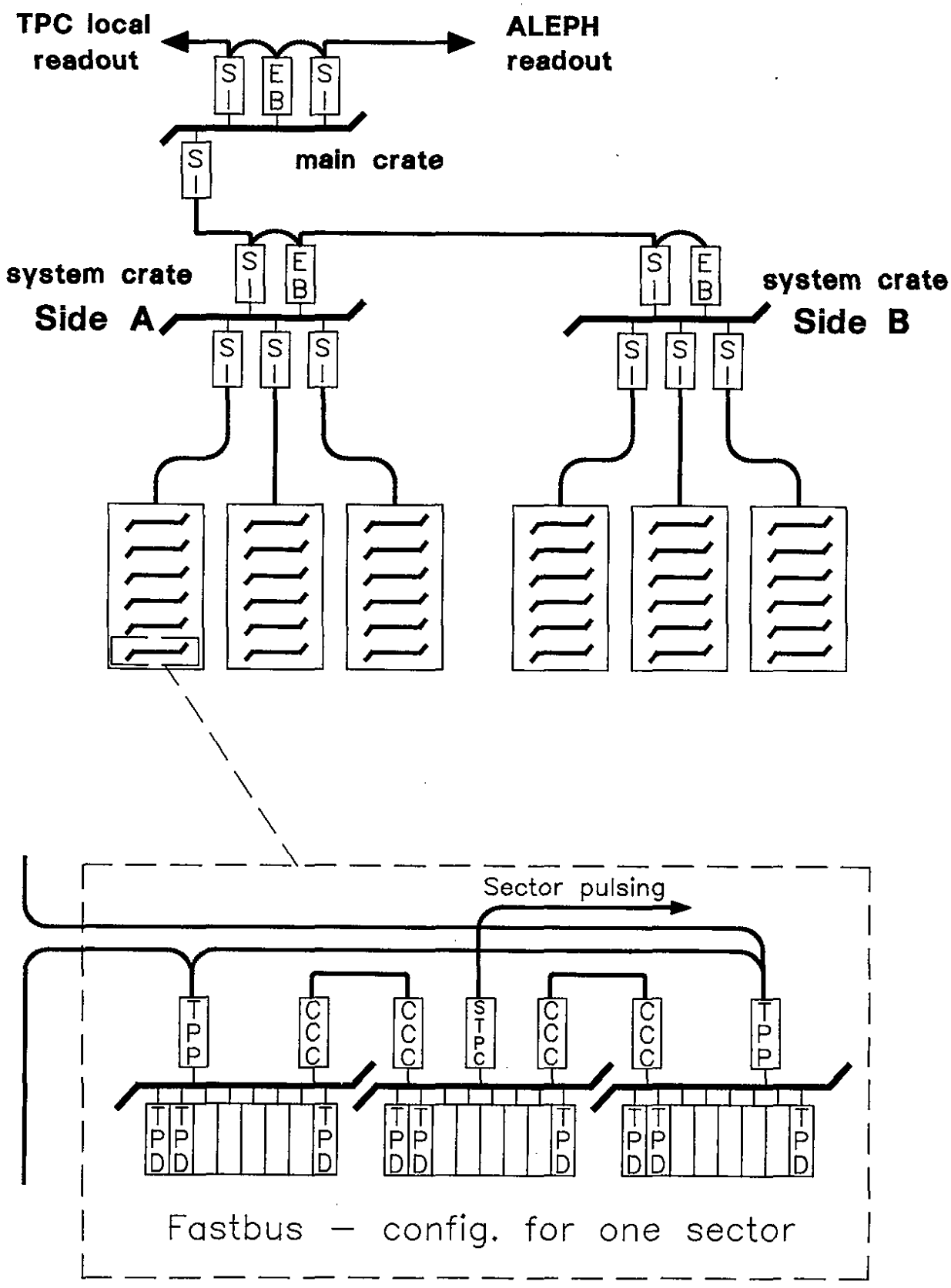
TPC local readout
ALEPH readout
S
E B
S
main crate
system crate Side A
system crate Side B
Sector pulsing
TPP
CCC
STPC
TPD
Fastbus – config. for one sector

Fig. 15

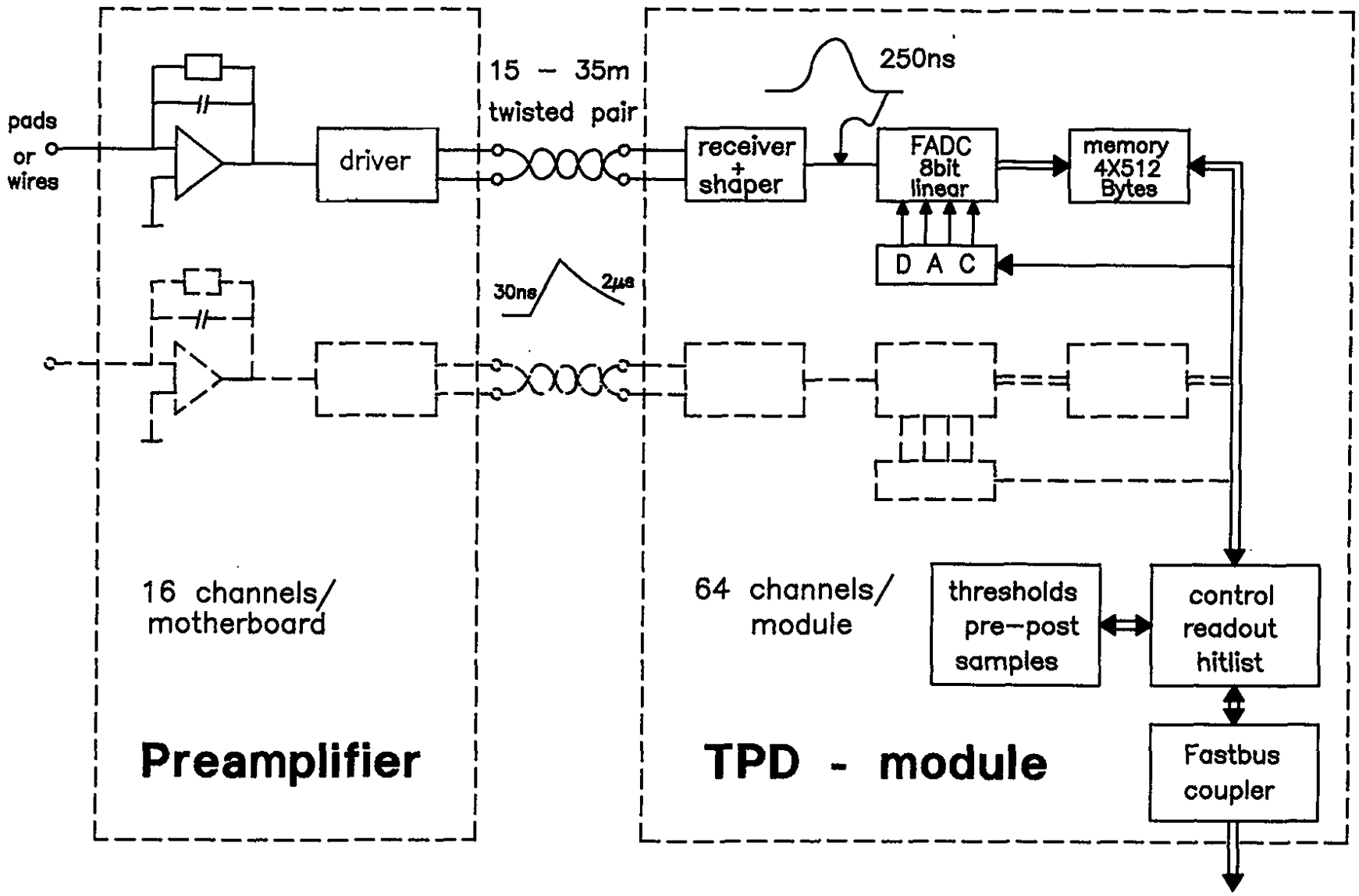
pads
or
wires
driver
15 – 35m
twisted pair
250ns
receiver
+
shaper
FADC
8bit
linear
memory
4X512
Bytes
D A C
30ns
2μs
16 channels/
motherboard
64 channels/
module
thresholds
pre–post
samples
control
readout
hitlist
Fastbus
coupler
Preamplifier
TPD - module

Fig. 16

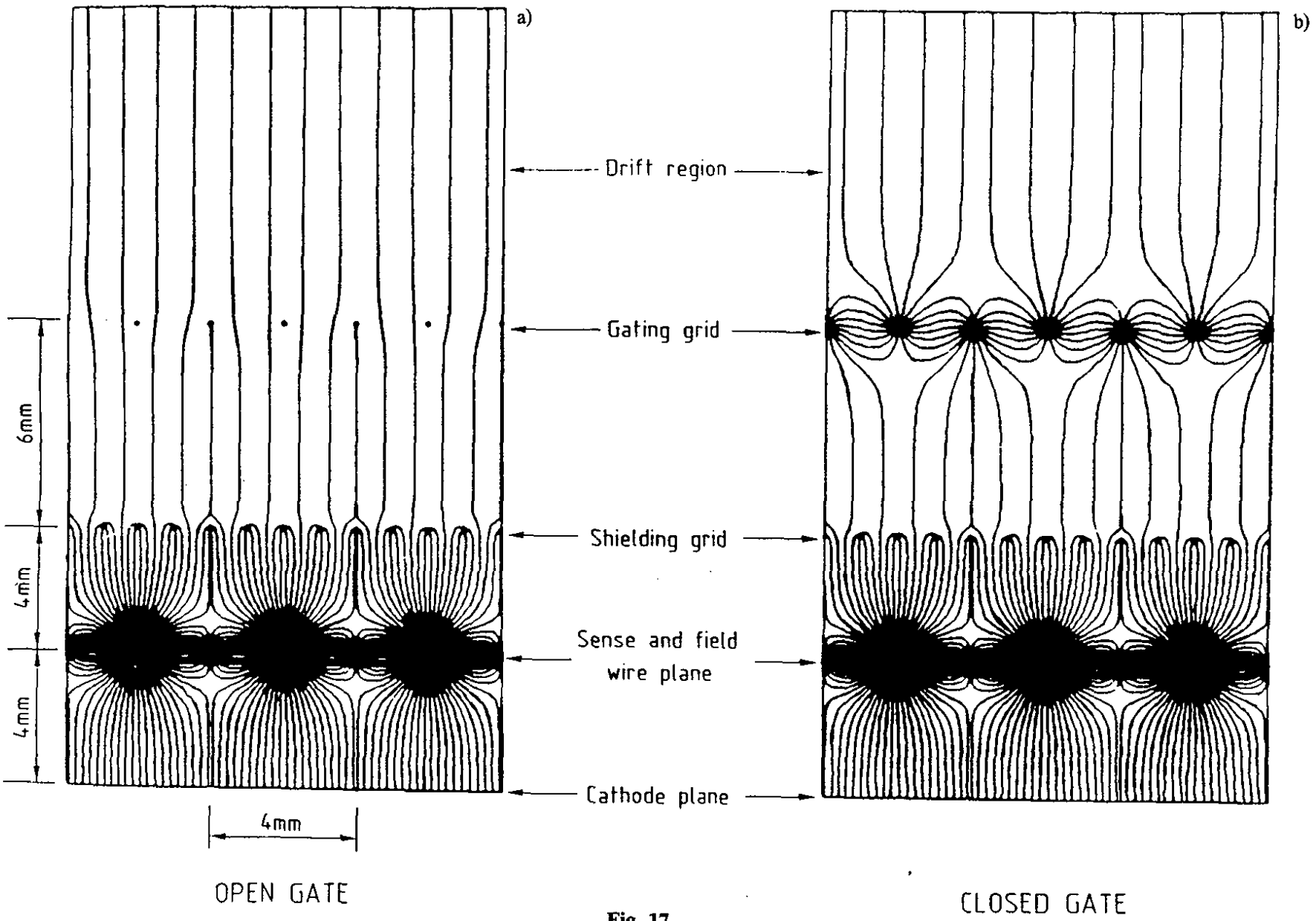
a)
b)
Drift region
Gating grid
Shielding grid
Sense and field
wire plane
Cathode plane
6mm
4mm
4mm
4mm
OPEN GATE
CLOSED GATE

Fig. 17

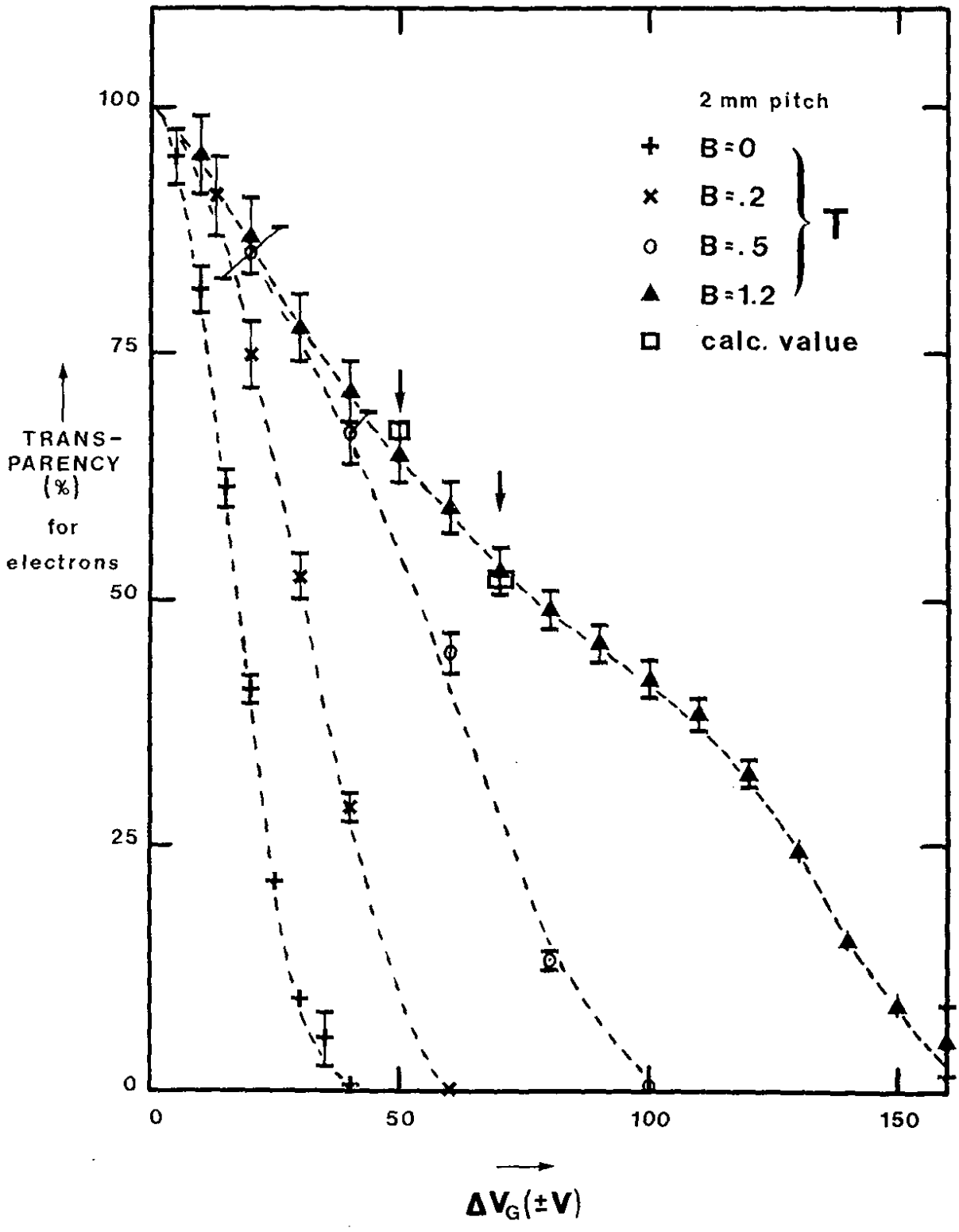
2 mm pitch
B=0
B=.2
B=.5
B=1.2
T
calc. value
TRANS-
PARENCY
(%)
for
electrons
100
75
50
25
0
0
50
100
150
ΔV_G(±V)

Fig. 18

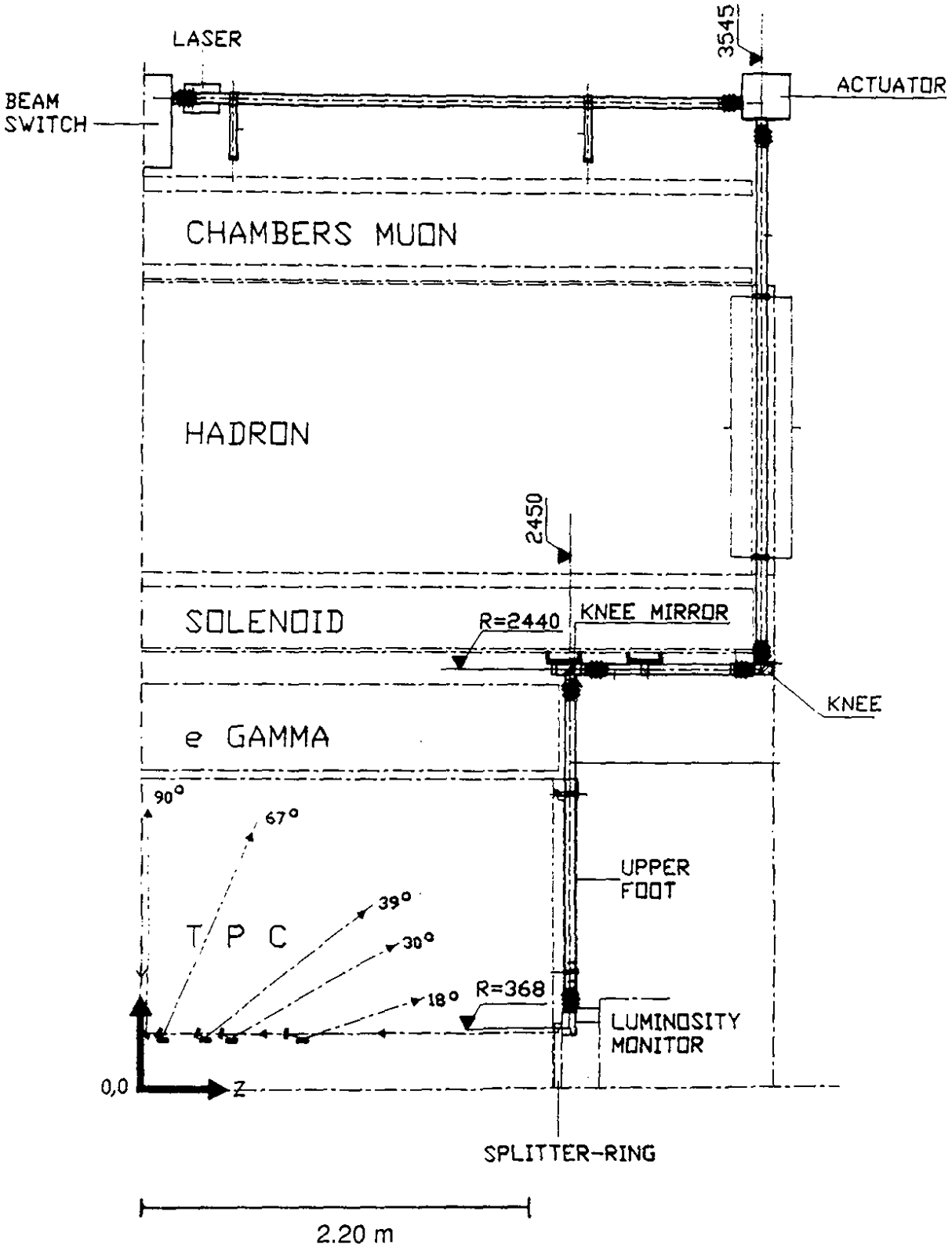
LASER
3545
BEAM
SWITCH
ACTUATOR
CHAMBERS MUON
HADRON
2450
SOLENOID
R=2440
KNEE MIRROR
KNEE
e GAMMA
90°
67°
39°
30°
18°
T P C
R=368
UPPER
FOOT
LUMINOSITY
MONITOR
0,0
Z
SPLITTER-RING
2.20 m

Fig. 19

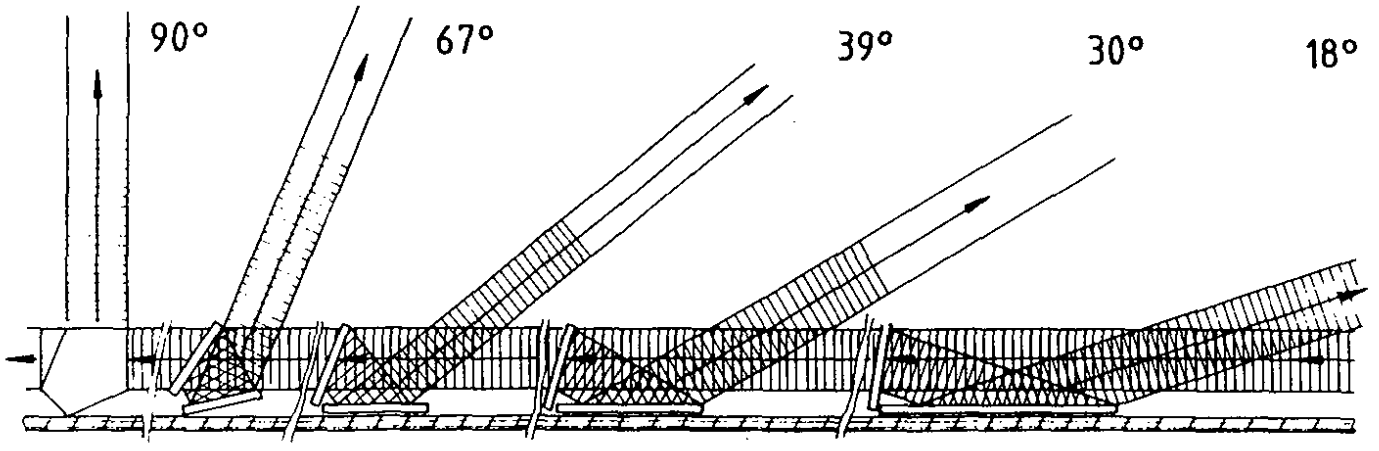

inner field cage

Fig. 20

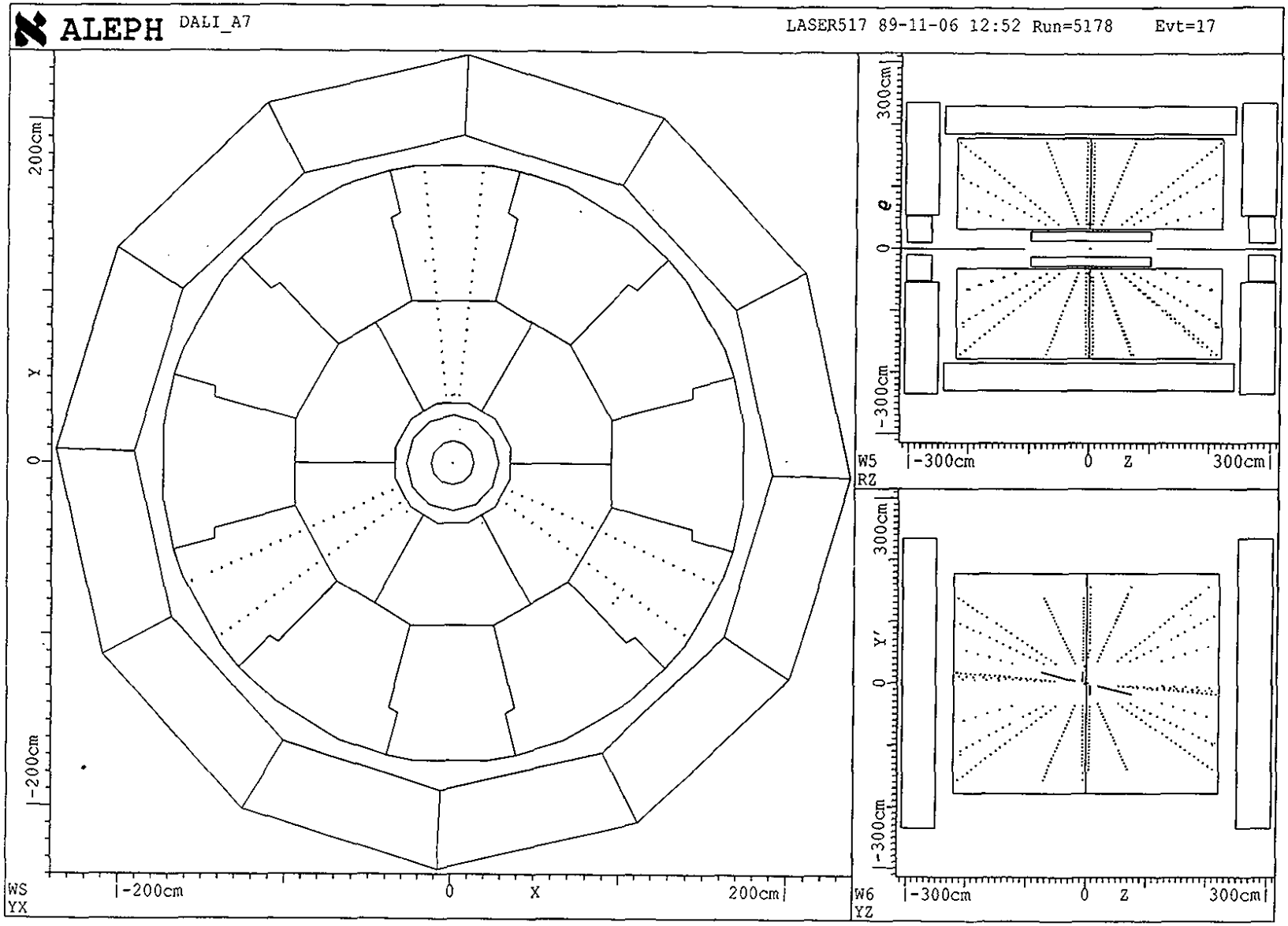
ALEPH
DALI_A7
LASER517 89-11-06 12:52 Run=5178 Evt=17
200cm
Y
0
-200cm
WS
YX
-200cm
0
X
200cm
300cm
e
0
-300cm
W5
RZ
-300cm
0
Z
300cm
300cm
Y'
0
-300cm
W6
YZ
-300cm
0
Z
300cm

Fig. 21

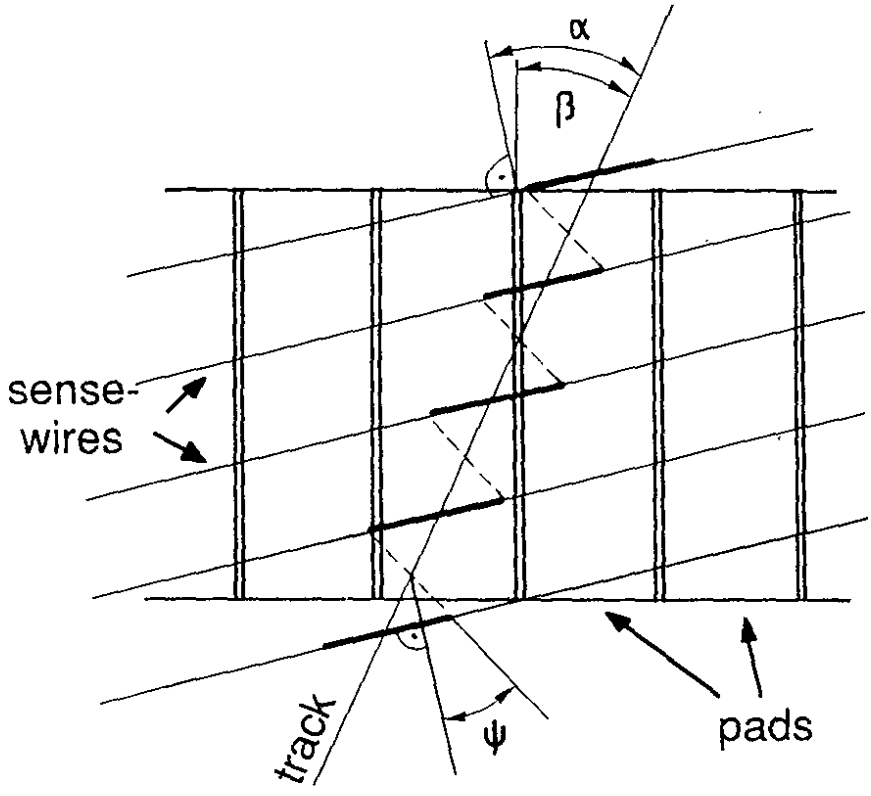

Fig. 22

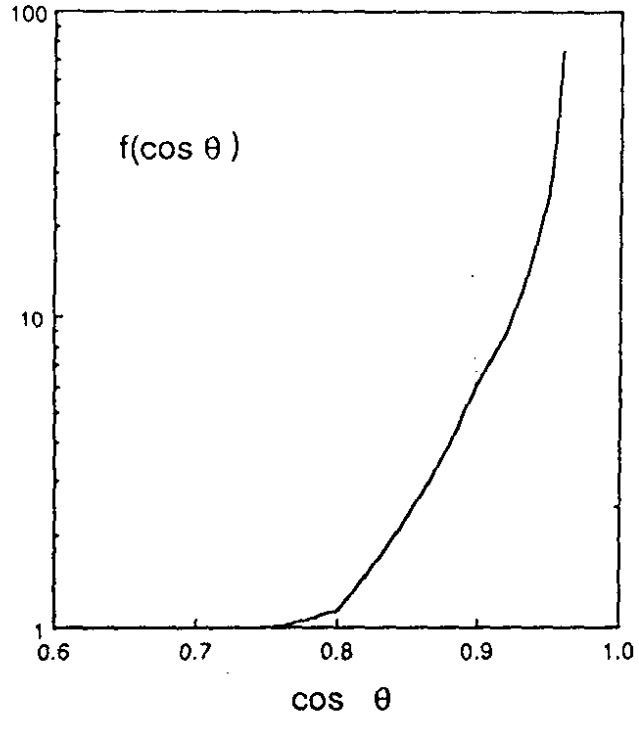

Fig. 23

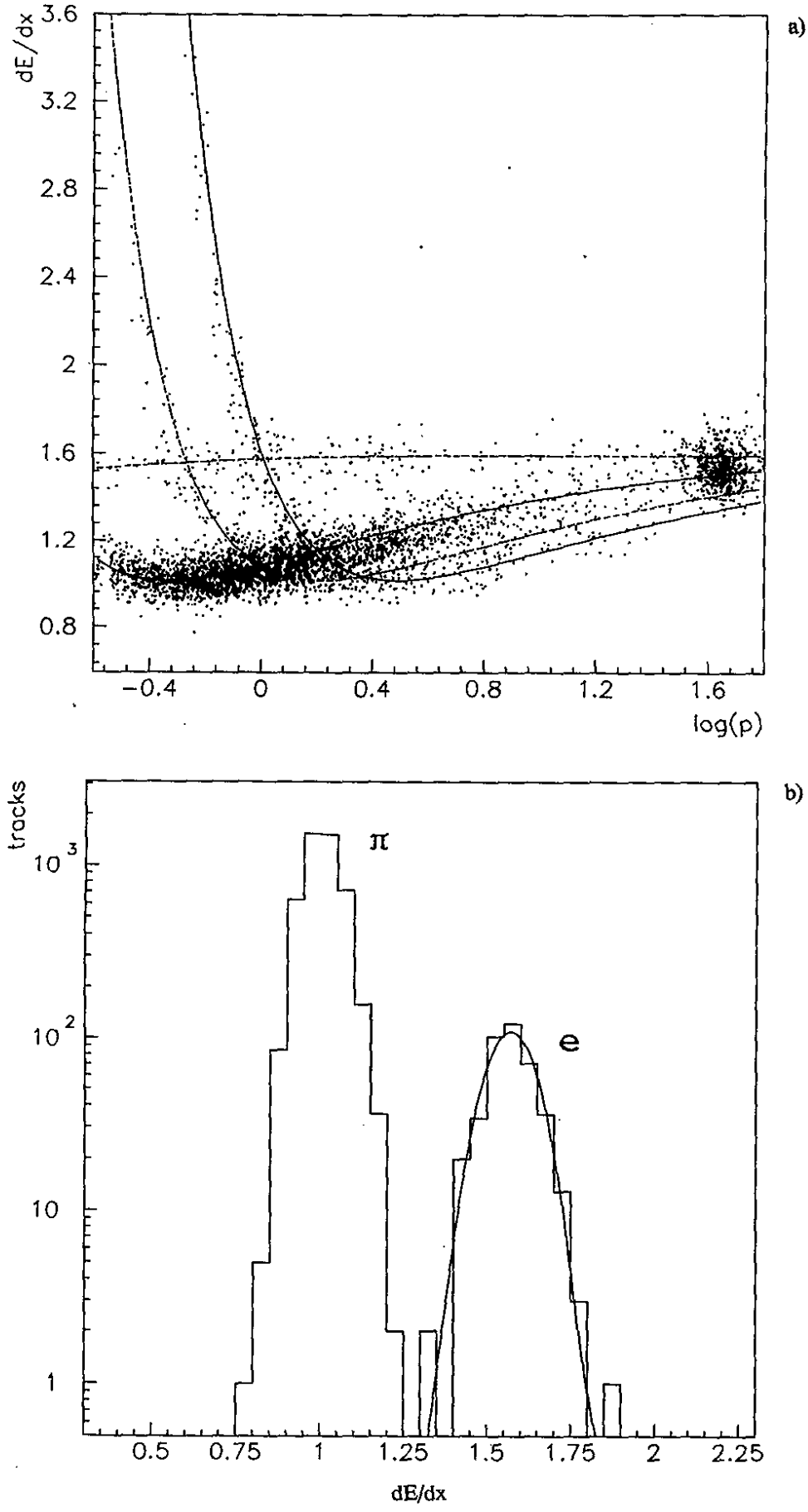
a)
dE/dx
3.6
3.2
2.8
2.4
2
1.6
1.2
0.8
−0.4
0
0.4
0.8
1.2
1.6
log(p)
b)
tracks
10^3
10^2
10
1
π
e
0.5
0.75
1
1.25
1.5
1.75
2
2.25
dE/dx

Fig. 24

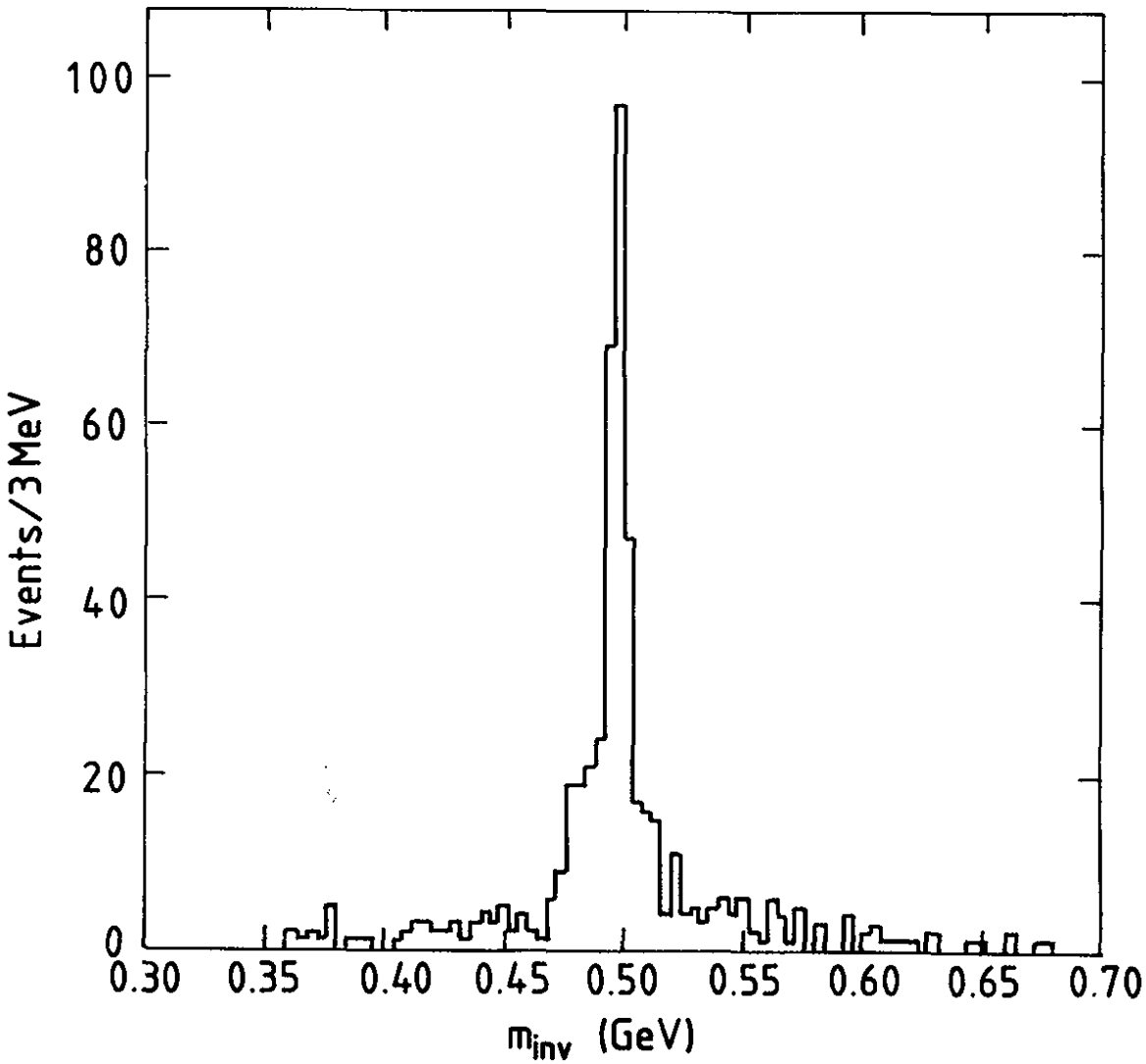
100
80
60
40
20
0
Events/3MeV
0.30
0.35
0.40
0.45
0.50
0.55
0.60
0.65
0.70
m_{inv} (GeV)

Fig. 25

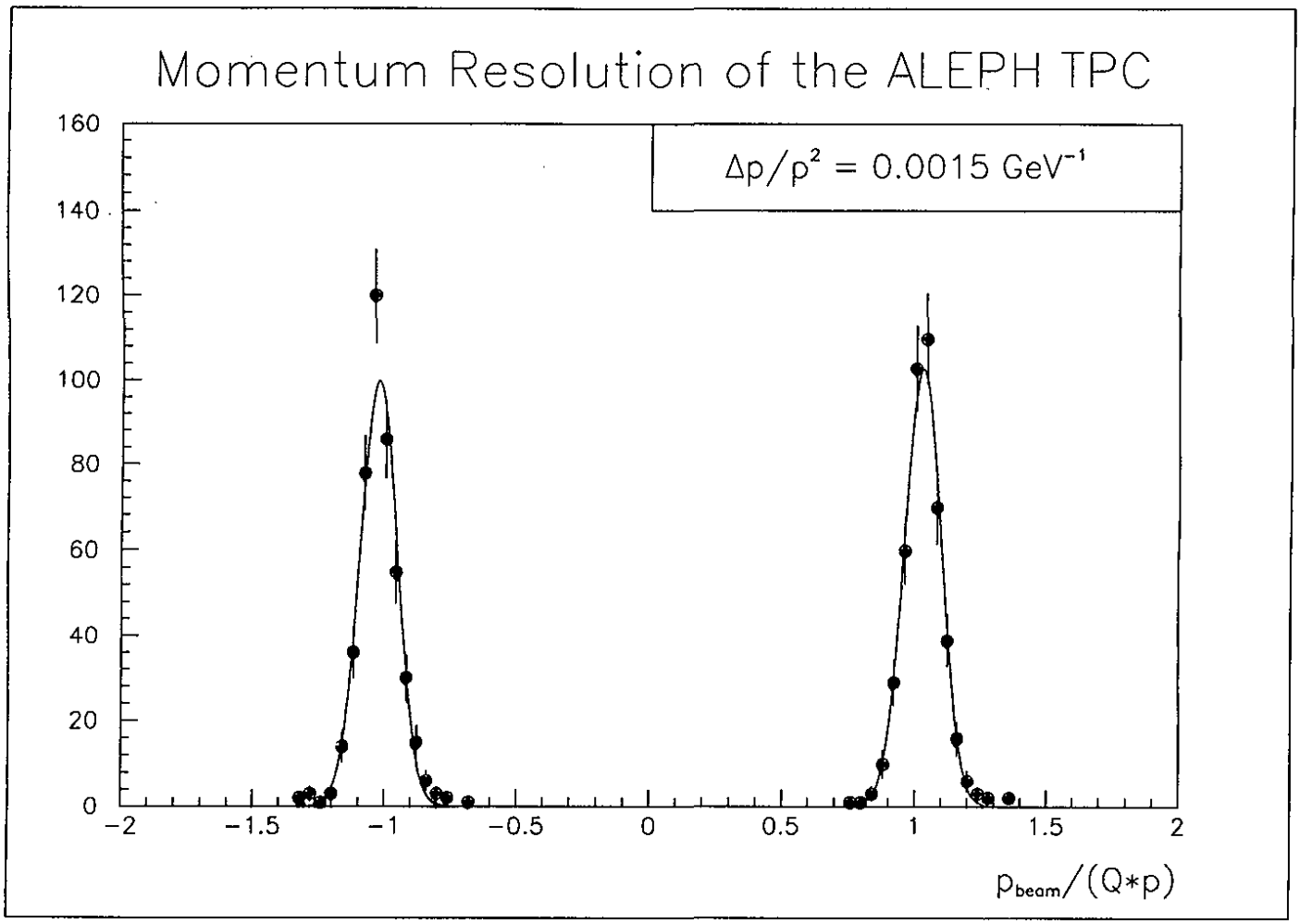
Momentum Resolution of the ALEPH TPC
$\Delta p/p^2 = 0.0015\ GeV^{-1}$
160
140
120
100
80
60
40
20
0
−2
−1.5
−1
−0.5
0
0.5
1
1.5
2
$p_{beam}/(Q*p)$

Fig. 26

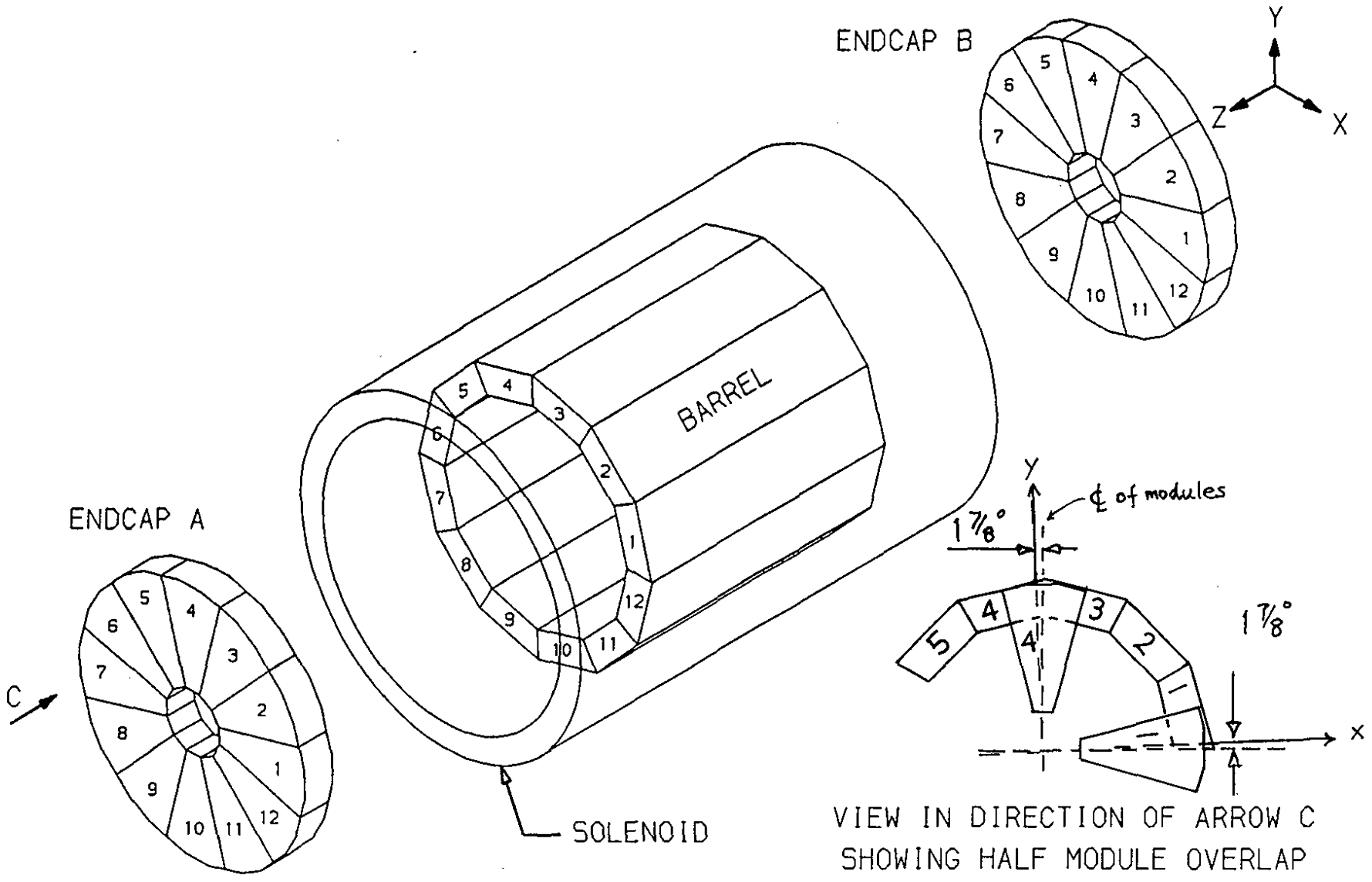
ENDCAP B
Y
Z
X
5
4
6
3
7
2
8
1
9
10
11
12
BARREL
ENDCAP A
C
SOLENOID
Y
℄ of modules
1 7/8°
1 7/8°
X
VIEW IN DIRECTION OF ARROW C
SHOWING HALF MODULE OVERLAP

Fig. 27

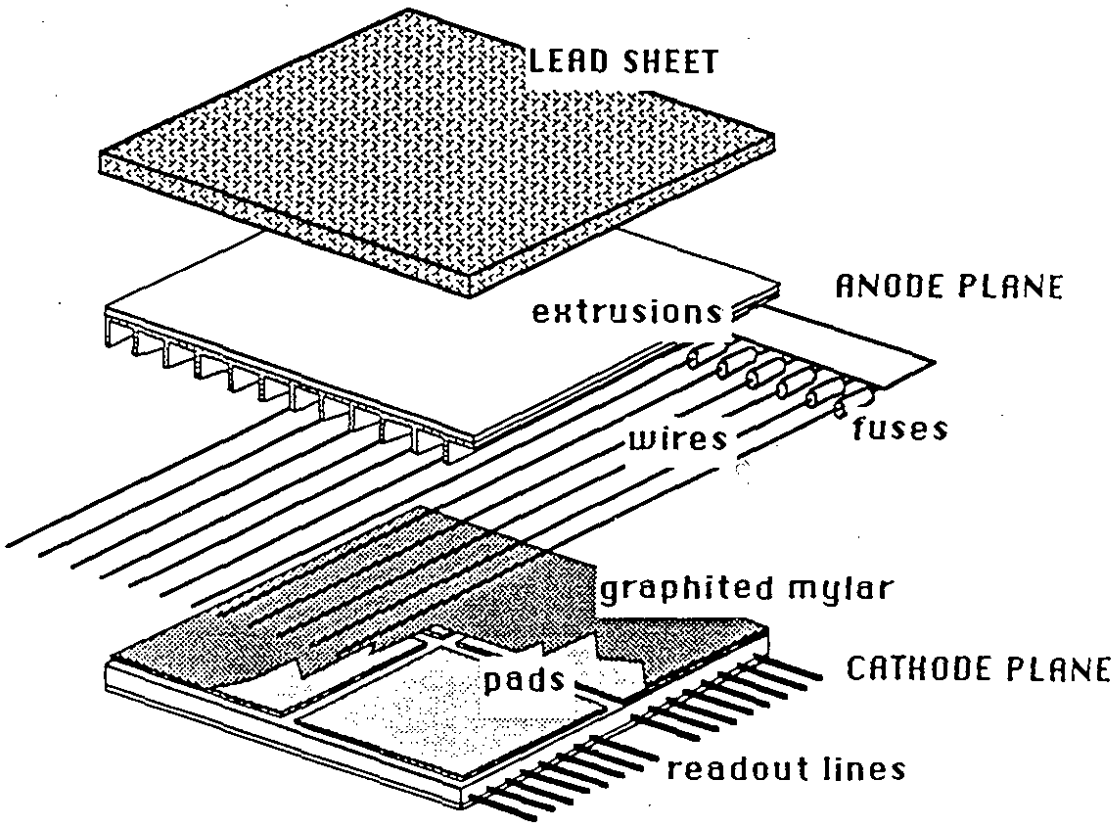
LEAD SHEET
ANODE PLANE
extrusions
wires
fuses
graphited mylar
pads
CATHODE PLANE
readout lines

Fig. 28

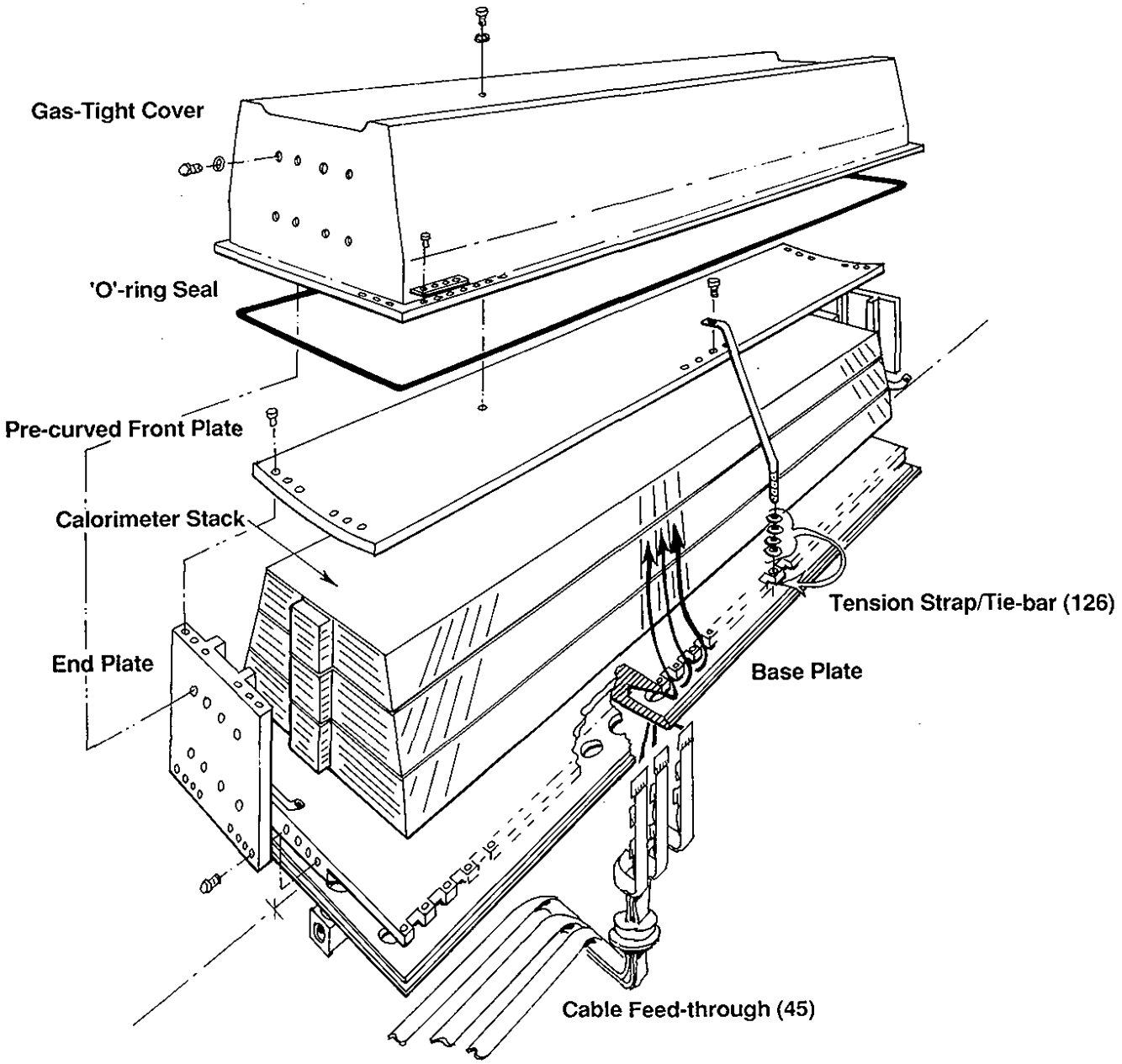
Gas-Tight Cover
'O'-ring Seal
Pre-curved Front Plate
Calorimeter Stack
End Plate
Tension Strap/Tie-bar (126)
Base Plate
Cable Feed-through (45)

Fig. 29

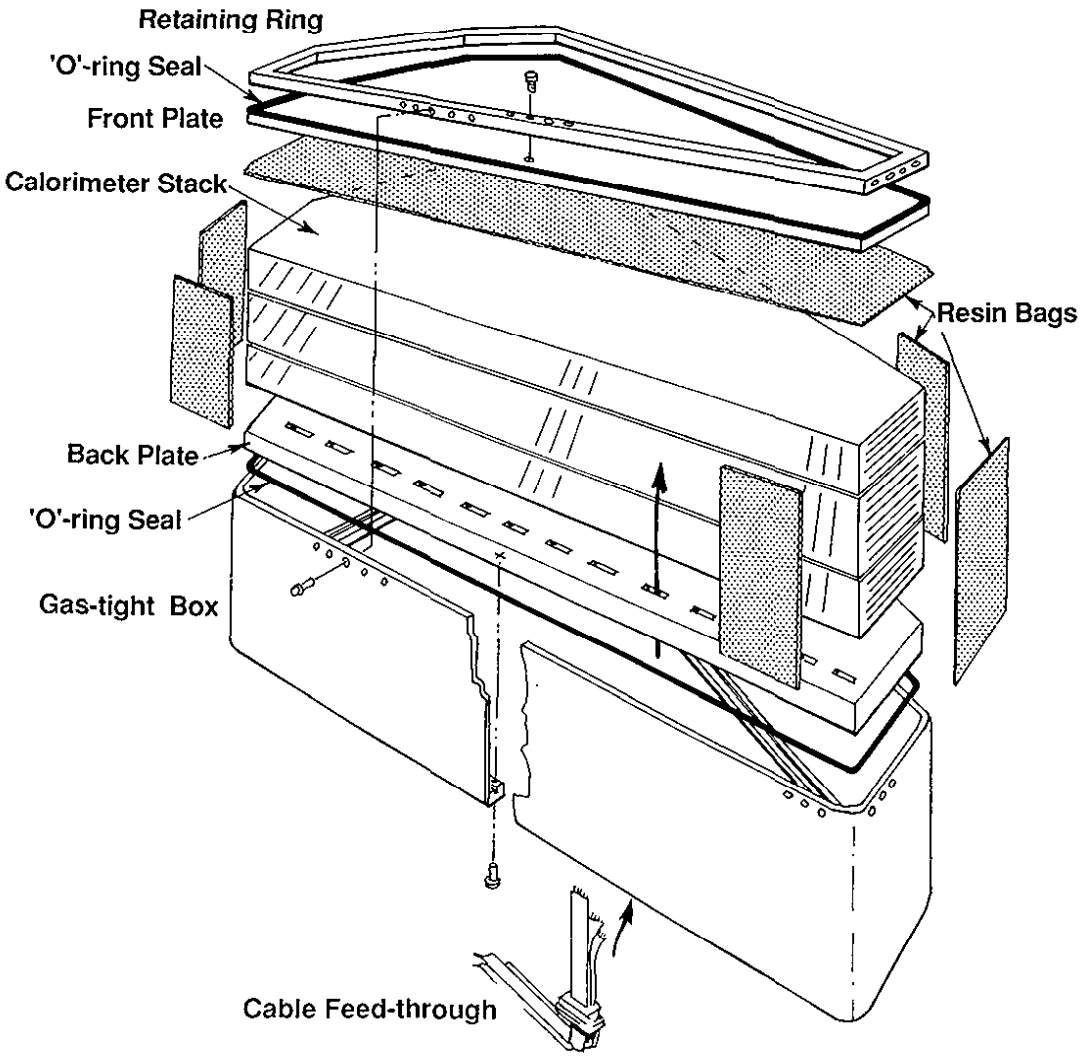
Retaining Ring
'O'-ring Seal
Front Plate
Calorimeter Stack
Resin Bags
Back Plate
'O'-ring Seal
Gas-tight Box
Cable Feed-through

Fig. 30

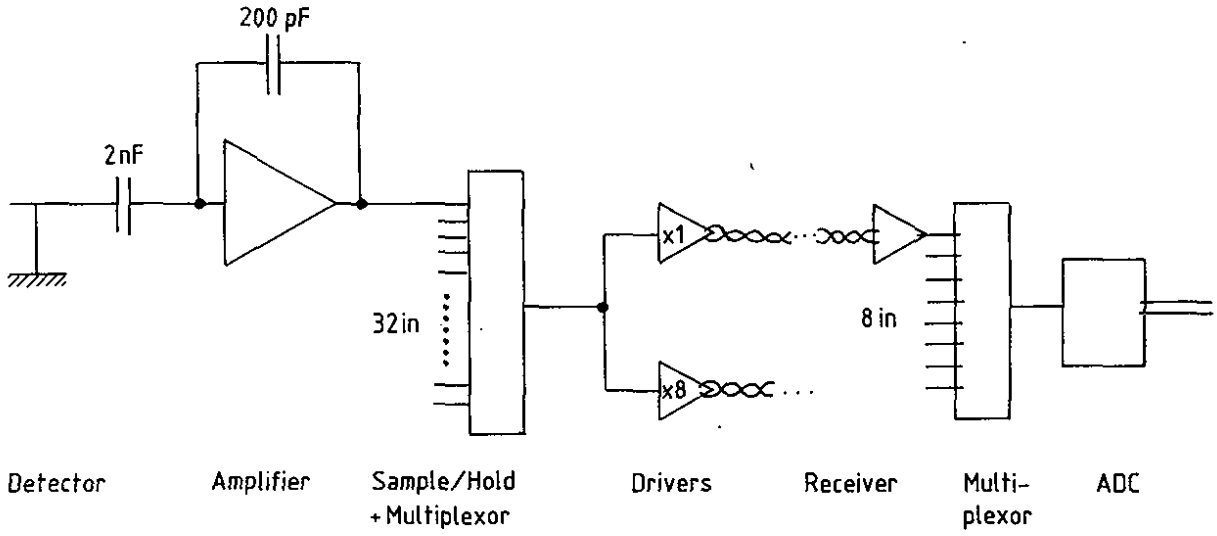
200 pF
2nF
32in
x1
x8
8 in
Detector
Amplifier
Sample/Hold
+Multiplexor
Drivers
Receiver
Multi-
plexor
ADC

Fig. 31

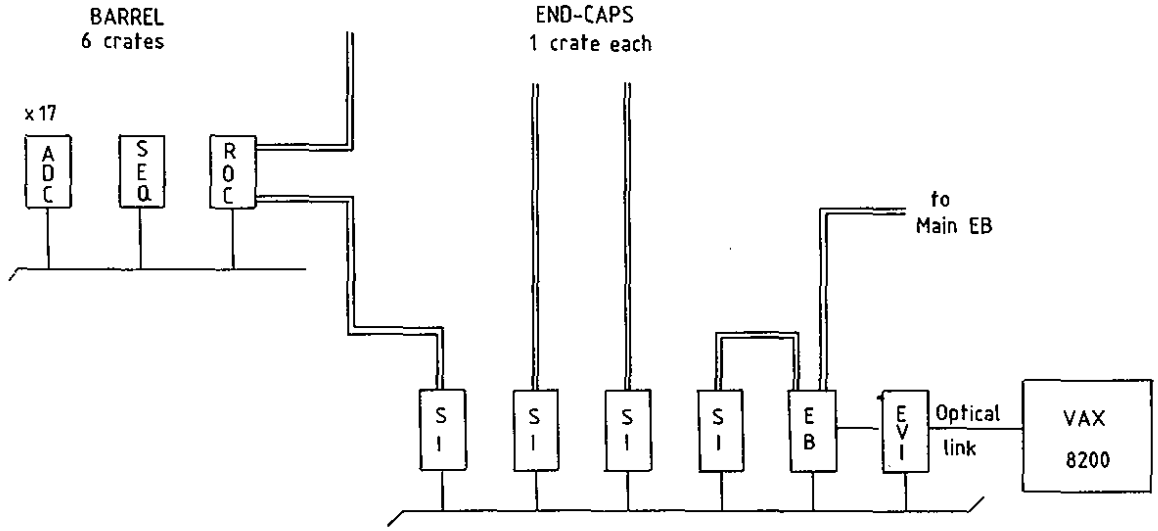
BARREL
6 crates
END-CAPS
1 crate each
x17
ADC
SEQ
ROC
SI
SI
SI
SI
EB
EVI
to
Main EB
Optical
link
VAX
8200

Fig. 32

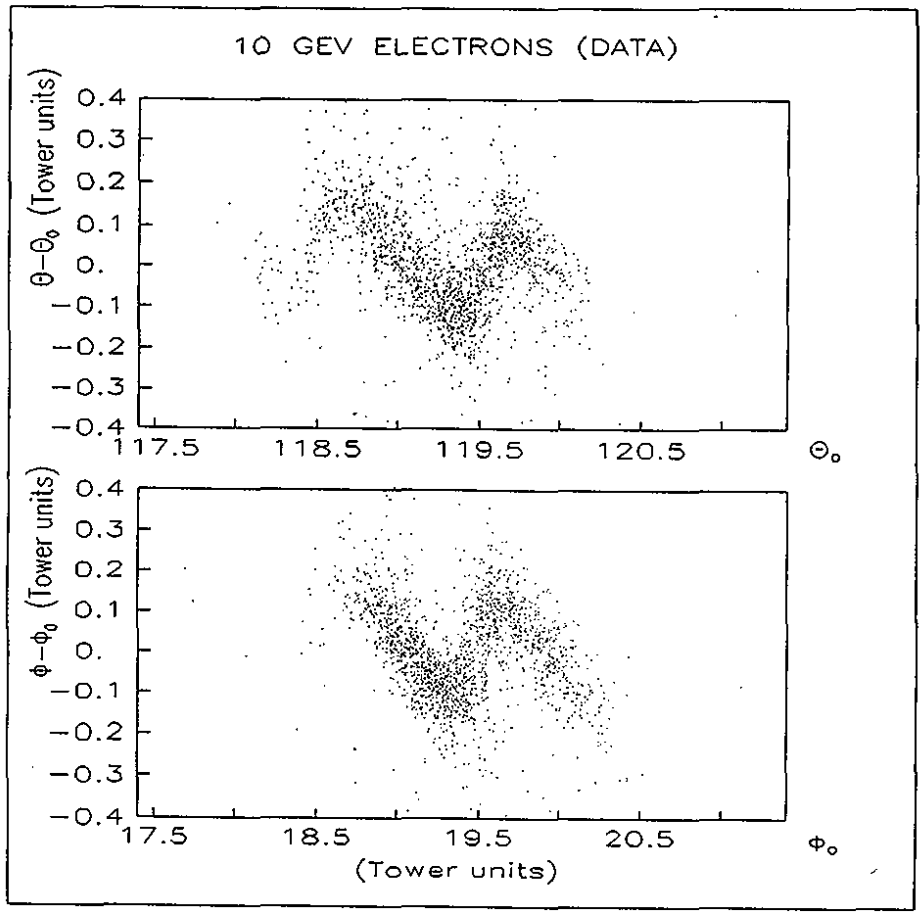
10 GEV ELECTRONS (DATA)
θ−θ₀ (Tower units)
0.4
0.3
0.2
0.1
0.
−0.1
−0.2
−0.3
−0.4
117.5
118.5
119.5
120.5
Θ₀
φ−φ₀ (Tower units)
17.5
18.5
19.5
20.5
Φ₀
(Tower units)

Fig. 33

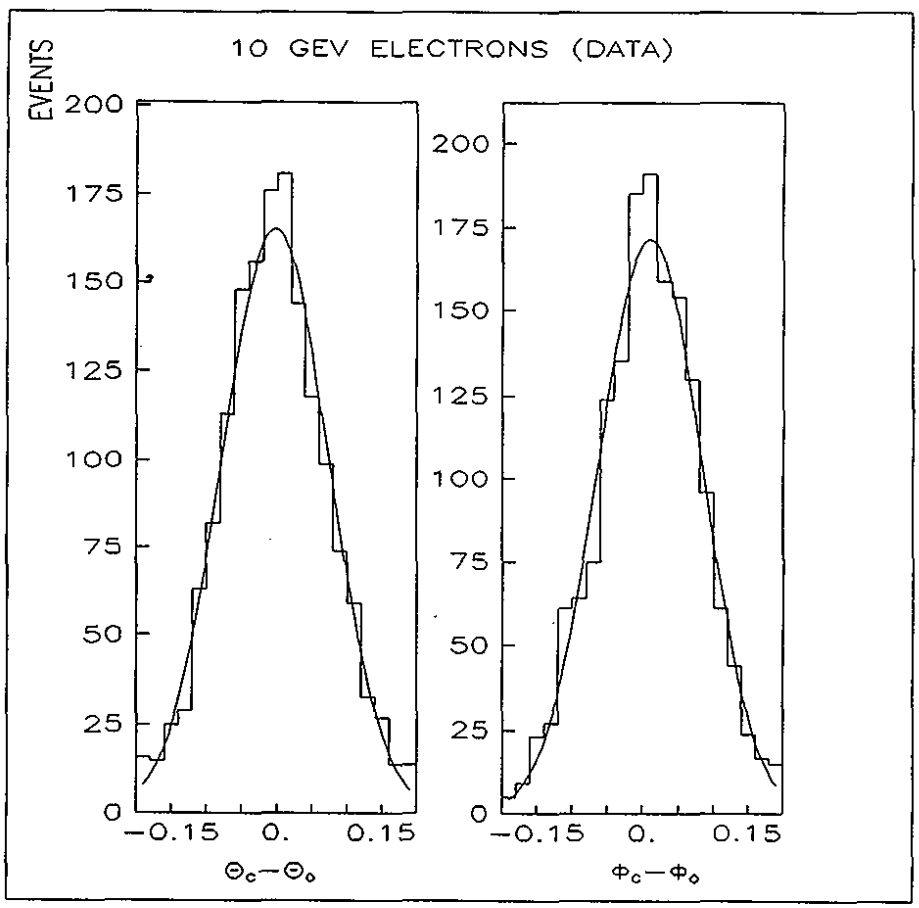
10 GEV ELECTRONS (DATA)
EVENTS
200
175
150
125
100
75
50
25
0
−0.15
0.
0.15
Θc−Θ₀
Φc−Φ₀

Fig. 34

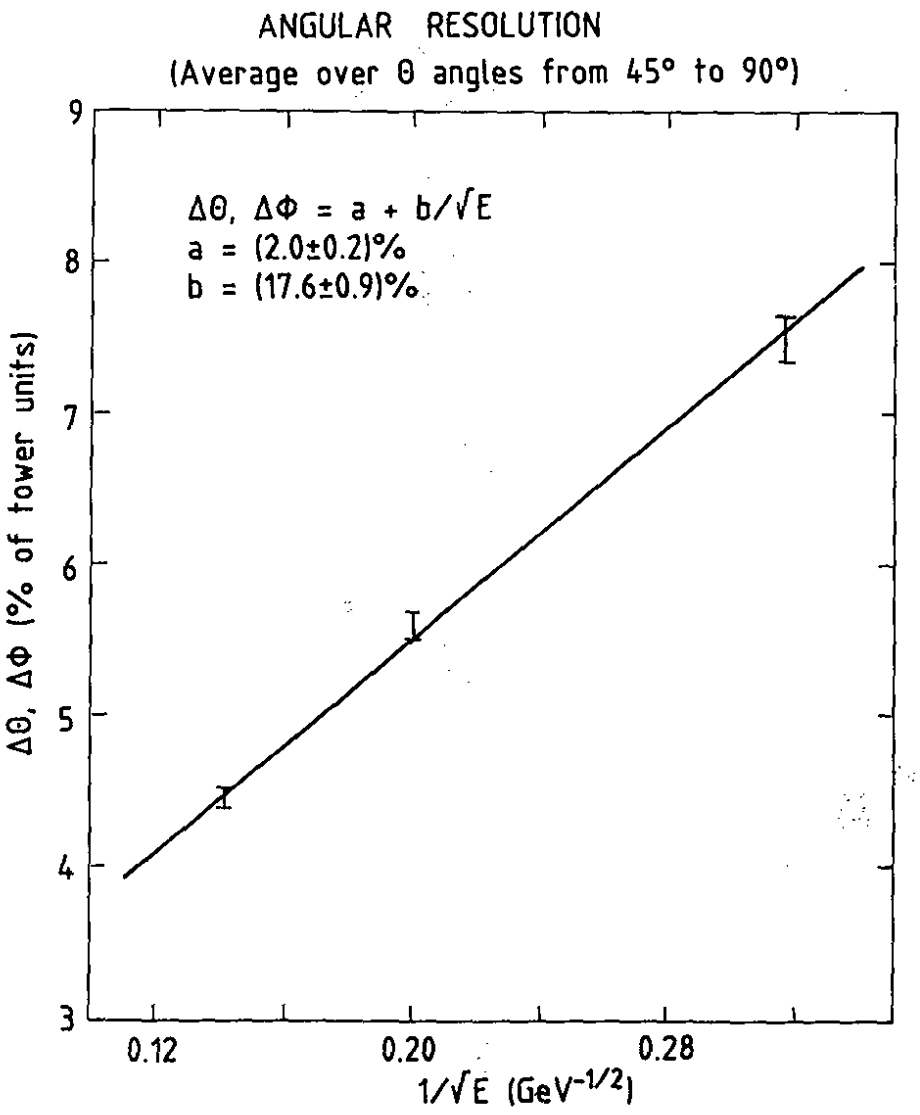
ANGULAR RESOLUTION
(Average over θ angles from 45° to 90°)
ΔΘ, ΔΦ = a + b/√E
a = (2.0±0.2)%
b = (17.6±0.9)%
ΔΘ, ΔΦ (% of tower units)
9
8
7
6
5
4
3
0.12
0.20
0.28
1/√E (GeV^-1/2)

Fig. 35

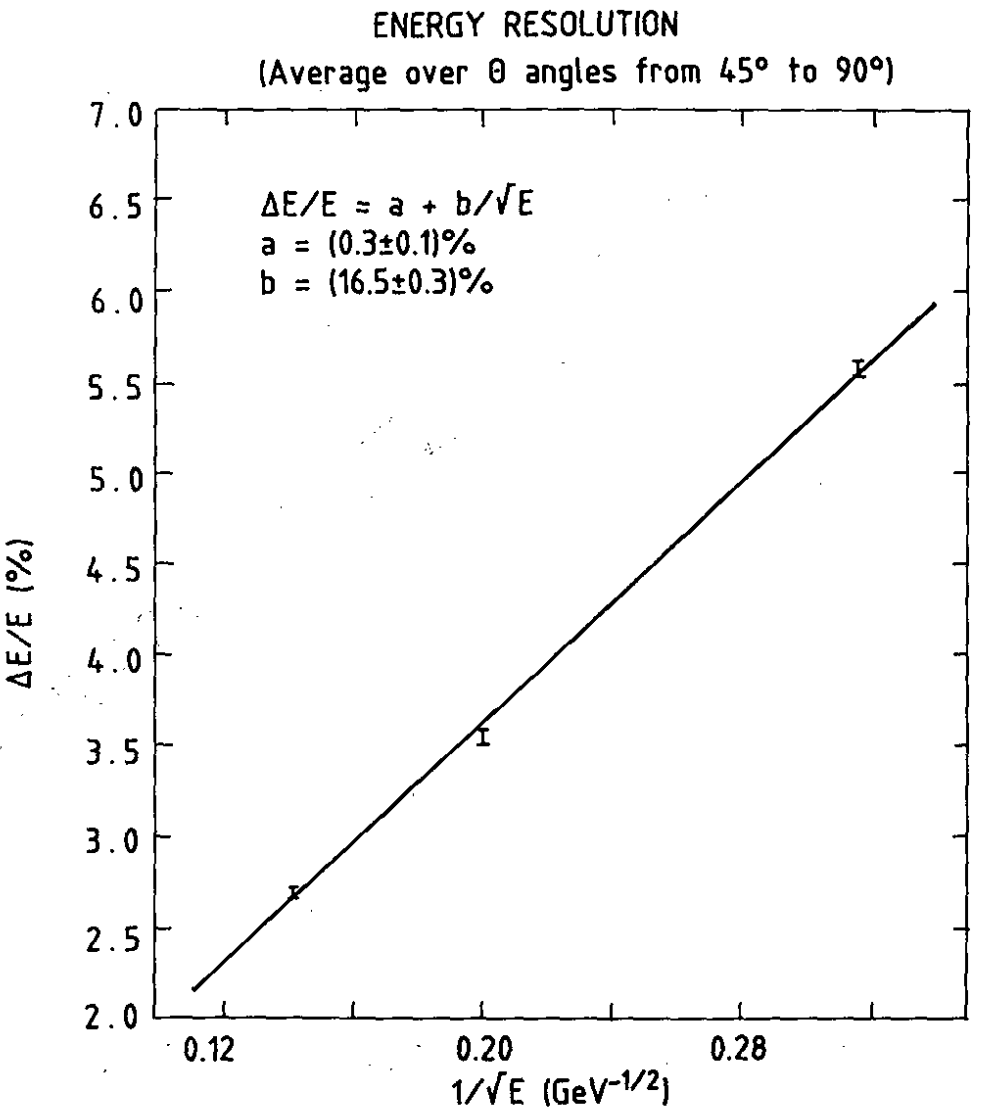
ENERGY RESOLUTION
(Average over θ angles from 45° to 90°)
ΔE/E = a + b/√E
a = (0.3±0.1)%
b = (16.5±0.3)%
ΔE/E (%)
7.0
6.5
6.0
5.5
5.0
4.5
4.0
3.5
3.0
2.5
2.0
0.12
0.20
0.28
1/√E (GeV^-1/2)

Fig. 36

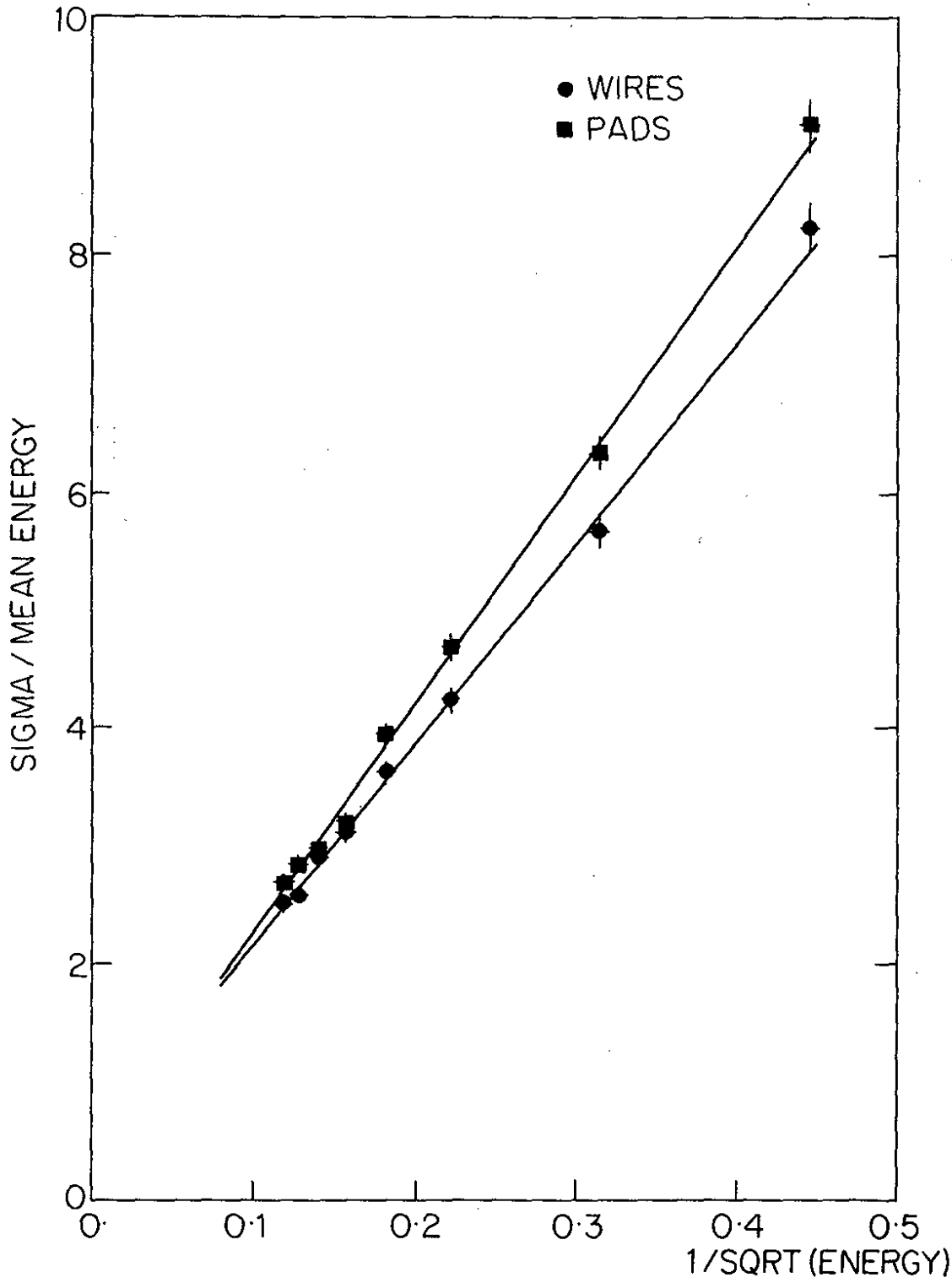
10
8
6
4
2
0
0·
0·1
0·2
0·3
0·4
0·5
WIRES
PADS
SIGMA / MEAN ENERGY
1/SQRT (ENERGY)

Fig. 37

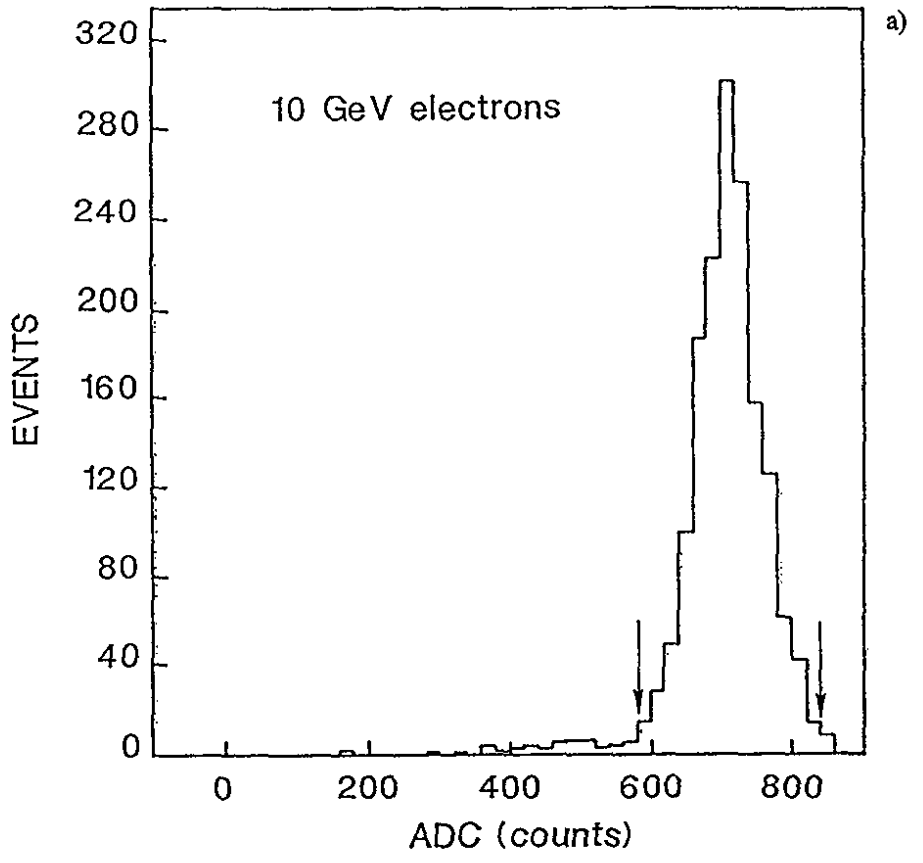
a)
10 GeV electrons
EVENTS
320
280
240
200
160
120
80
40
0
0
200
400
600
800
ADC (counts)

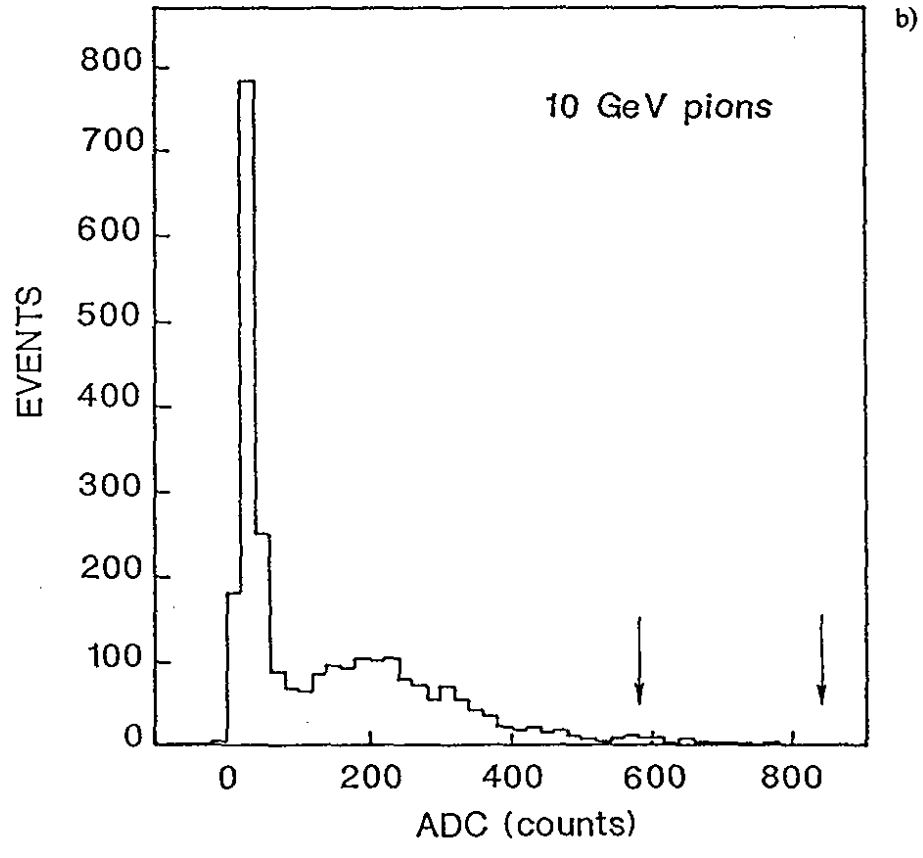
b)
10 GeV pions
EVENTS
800
700
600
500
400
300
200
100
0
0
200
400
600
800
ADC (counts)

Fig. 38

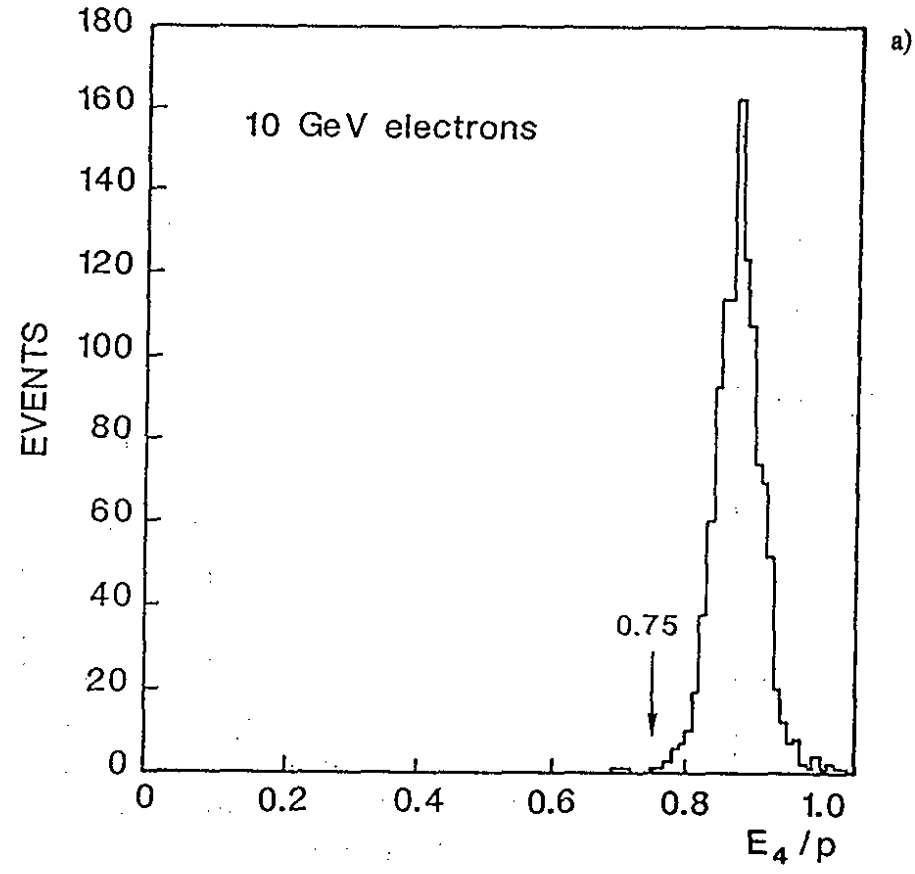
a)
10 GeV electrons
EVENTS
180
160
140
120
100
80
60
40
20
0
0.75
0
0.2
0.4
0.6
0.8
1.0
E4 /p

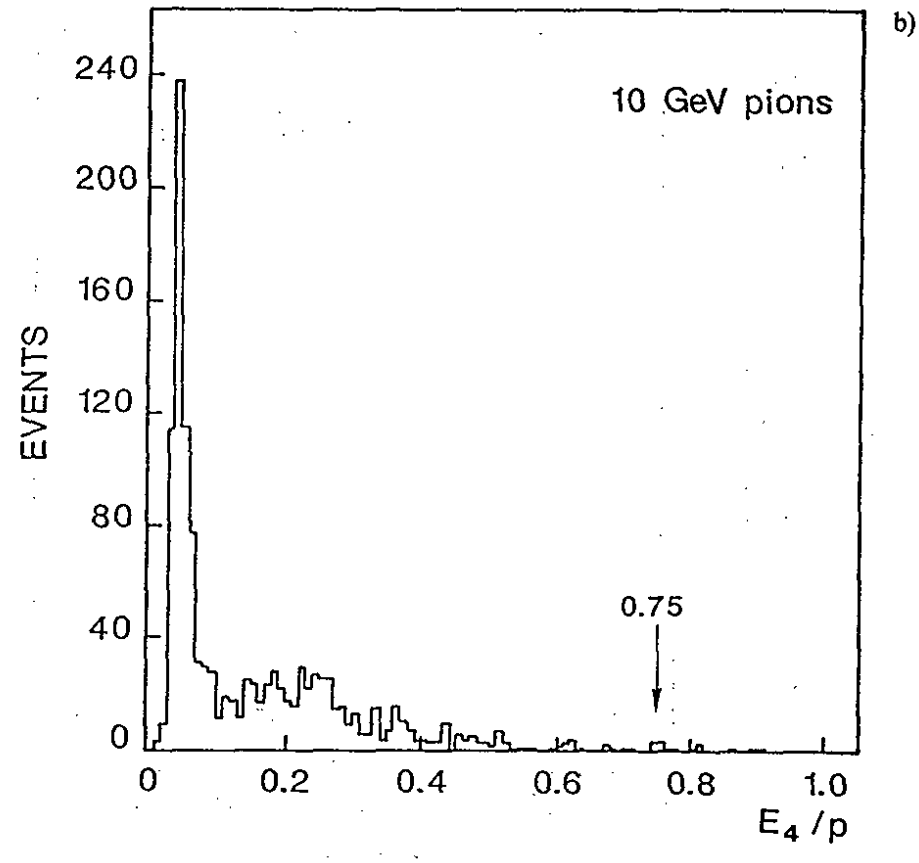
b)
10 GeV pions
EVENTS
240
200
160
120
80
40
0
0.75
0
0.2
0.4
0.6
0.8
1.0
E4 /p

Fig. 39

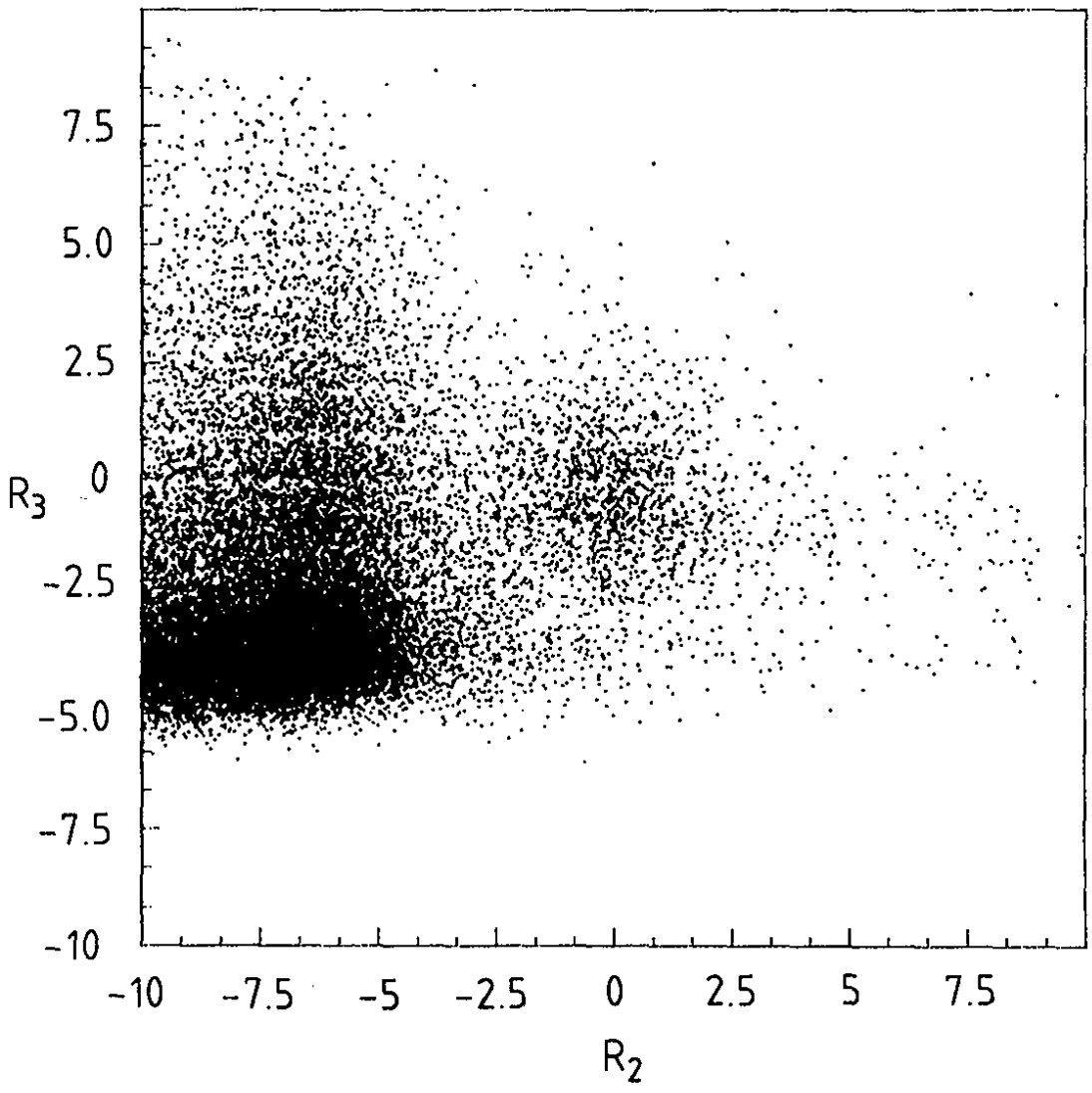

Fig. 40

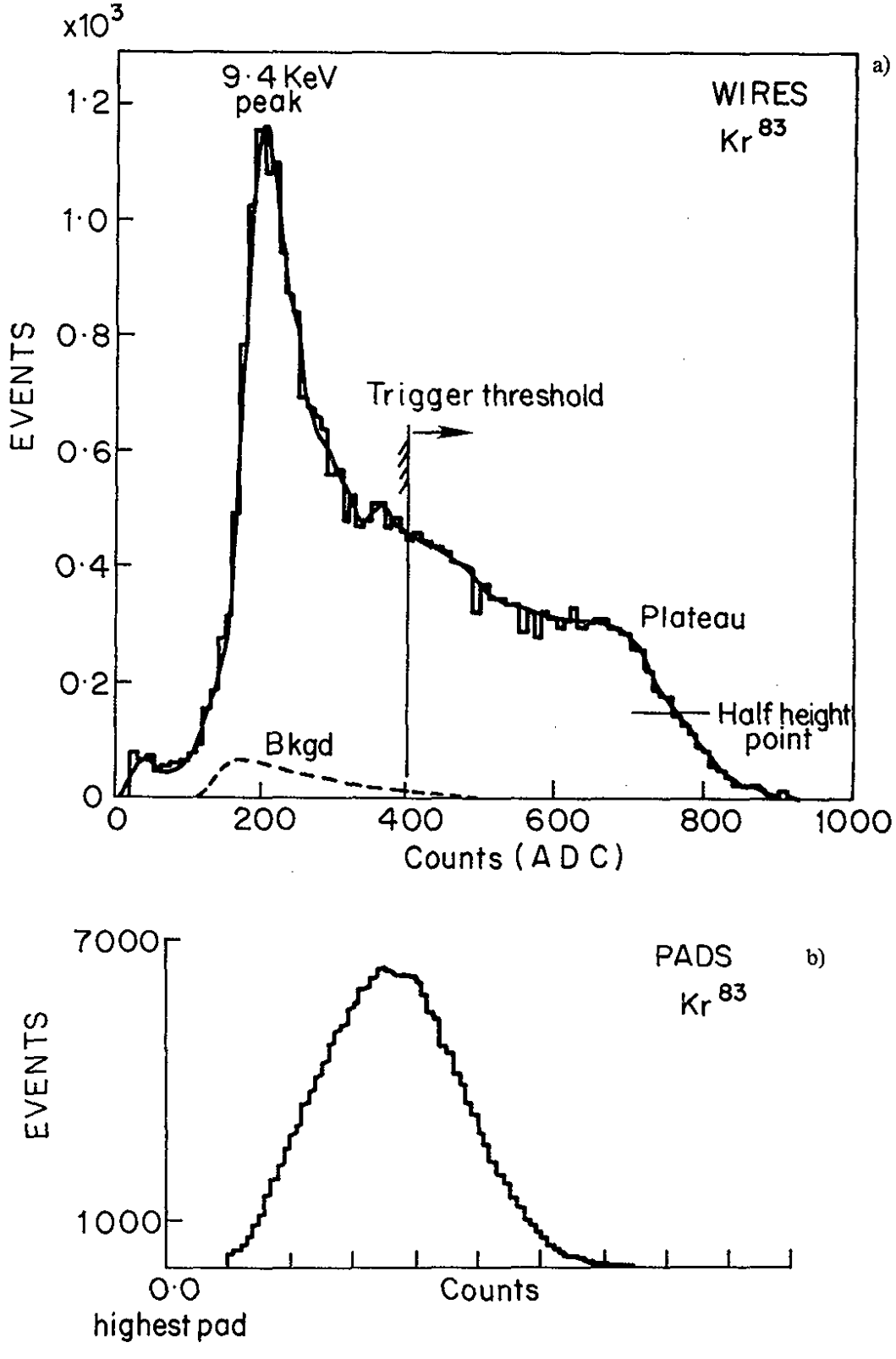
x10³
1·2
1·0
0·8
0·6
0·4
0·2
0
EVENTS
9·4 KeV
peak
WIRES
Kr 83
a)
Trigger threshold
Plateau
Half height
point
Bkgd
0
200
400
600
800
1000
Counts (A D C)
7000
1000
EVENTS
PADS
Kr 83
b)
0·0
highest pad
Counts

Fig. 41

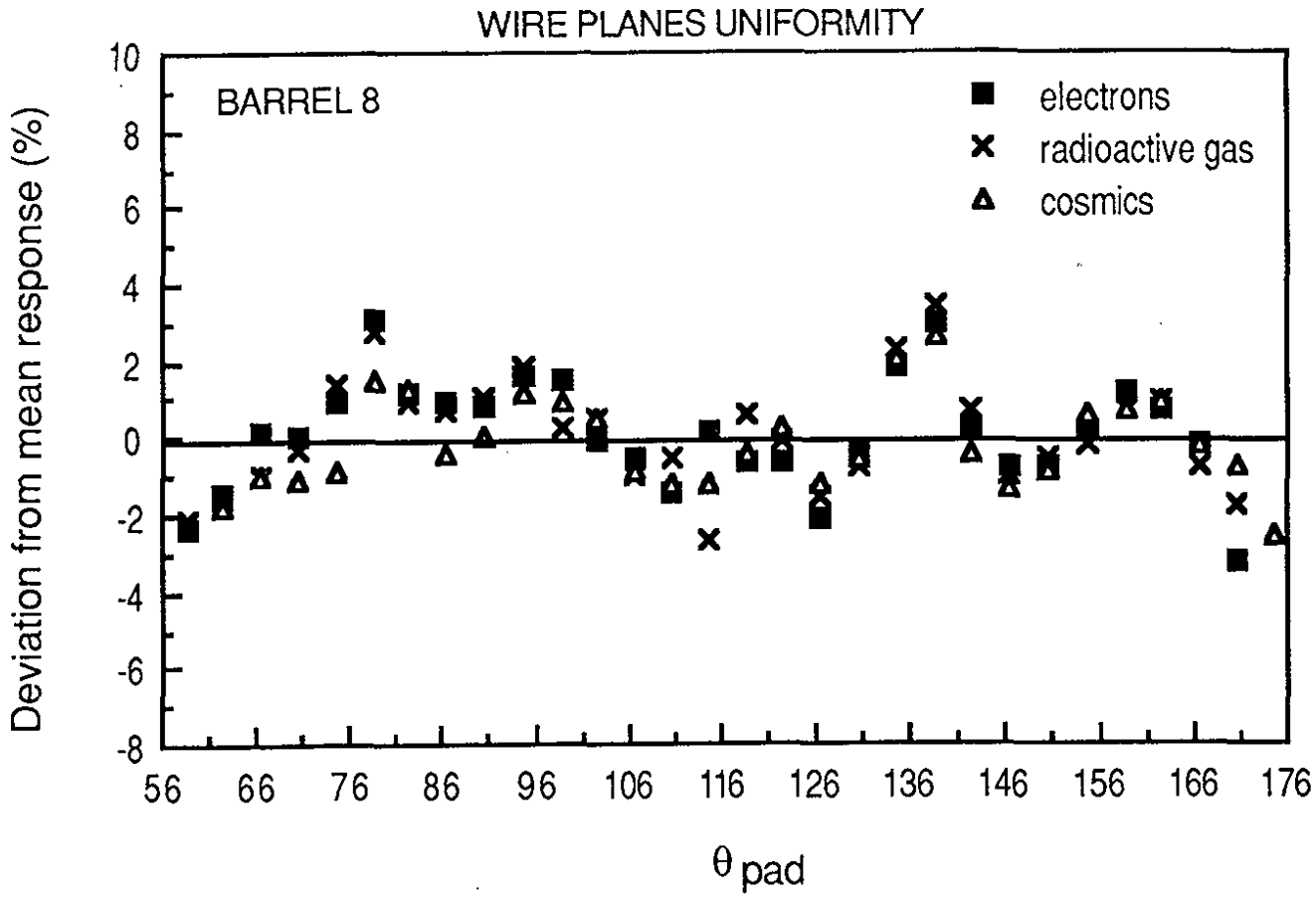
WIRE PLANES UNIFORMITY
BARREL 8
electrons
radioactive gas
cosmics
Deviation from mean response (%)
10
8
6
4
2
0
-2
-4
-6
-8
56
66
76
86
96
106
116
126
136
146
156
166
176
θ pad

Fig. 42

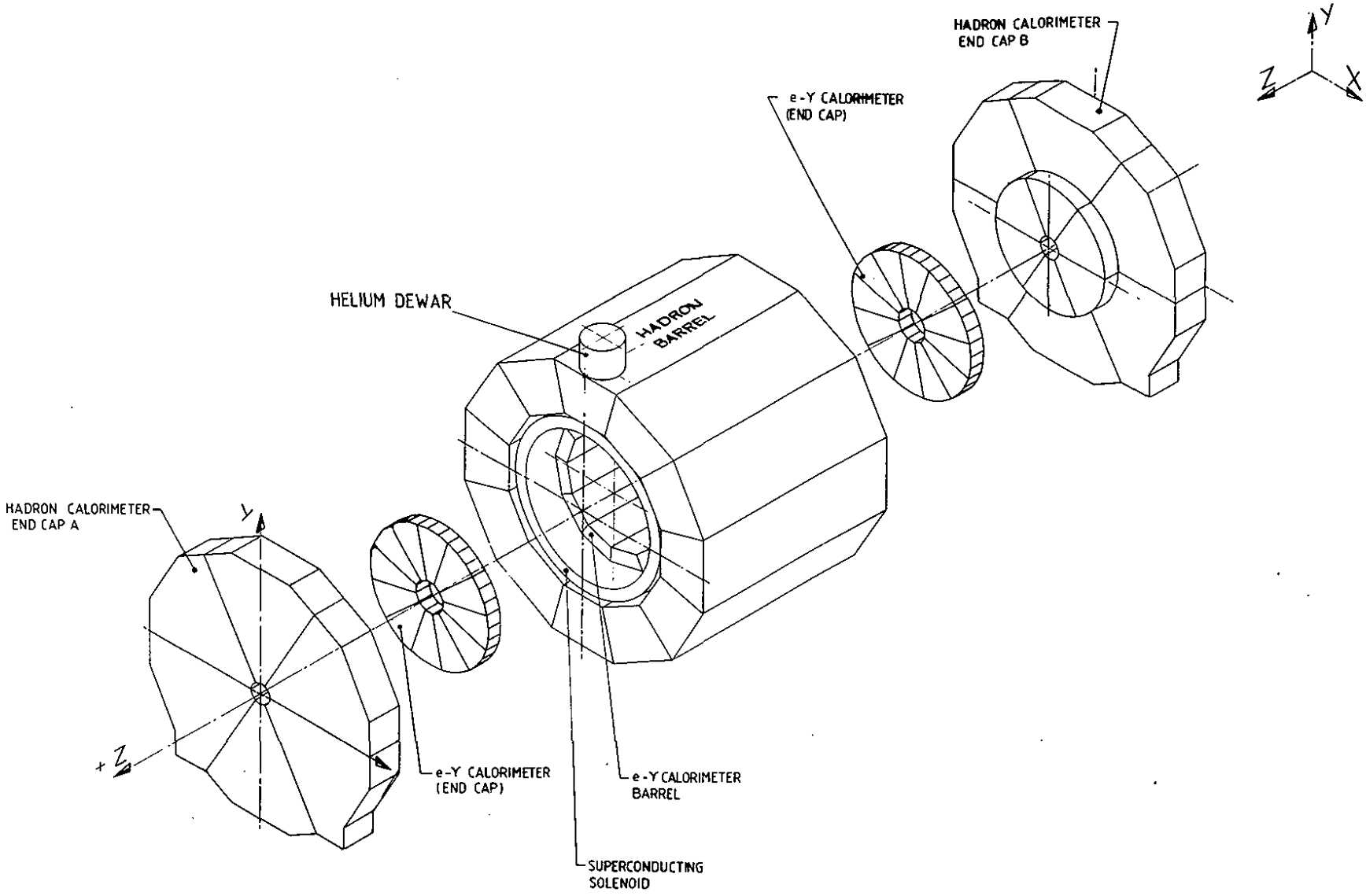
HADRON CALORIMETER
END CAP B
e-Y CALORIMETER
(END CAP)
HELIUM DEWAR
HADRON
BARREL
HADRON CALORIMETER
END CAP A
e-Y CALORIMETER
(END CAP)
e-Y CALORIMETER
BARREL
SUPERCONDUCTING
SOLENOID

Fig. 43

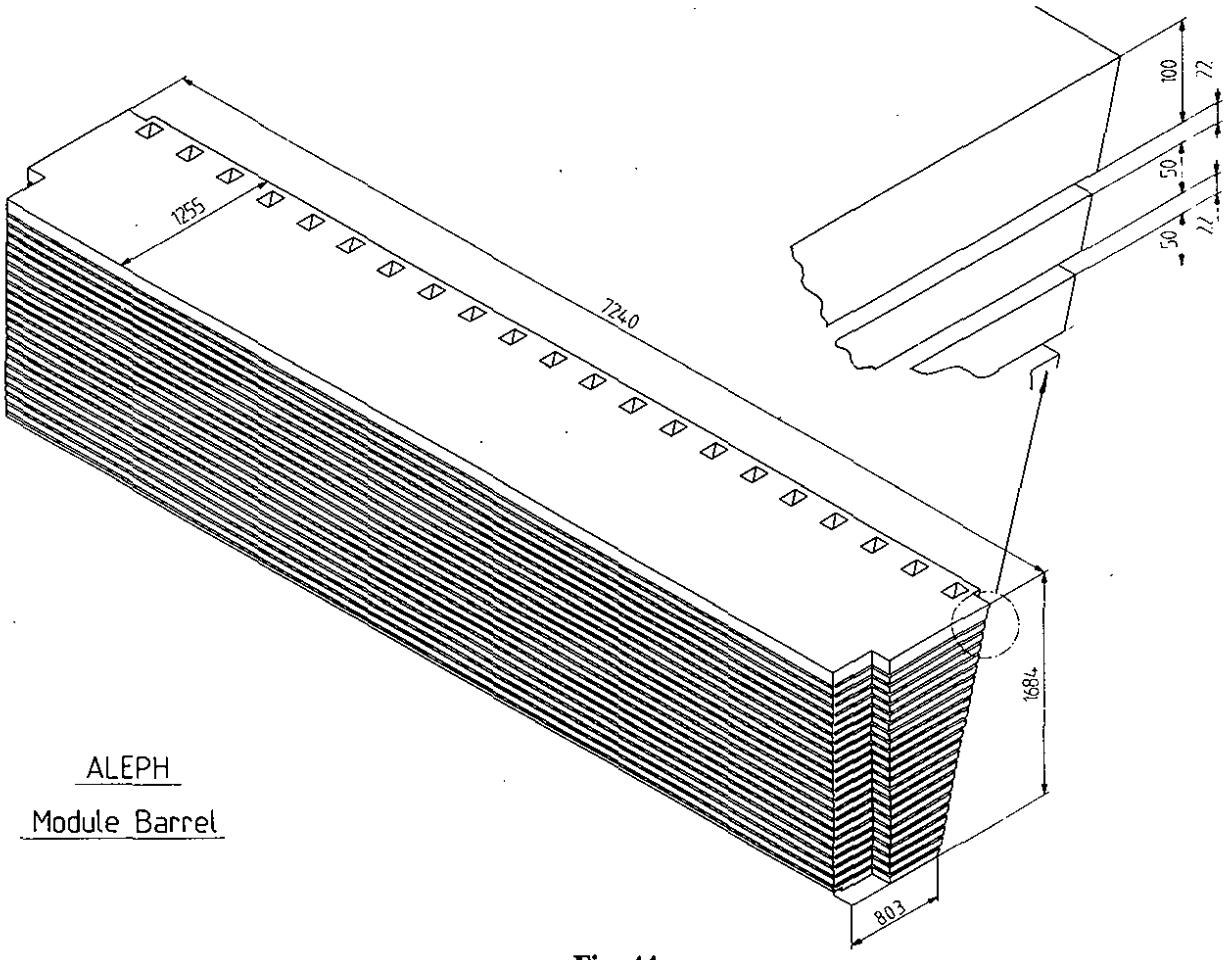

Fig. 44

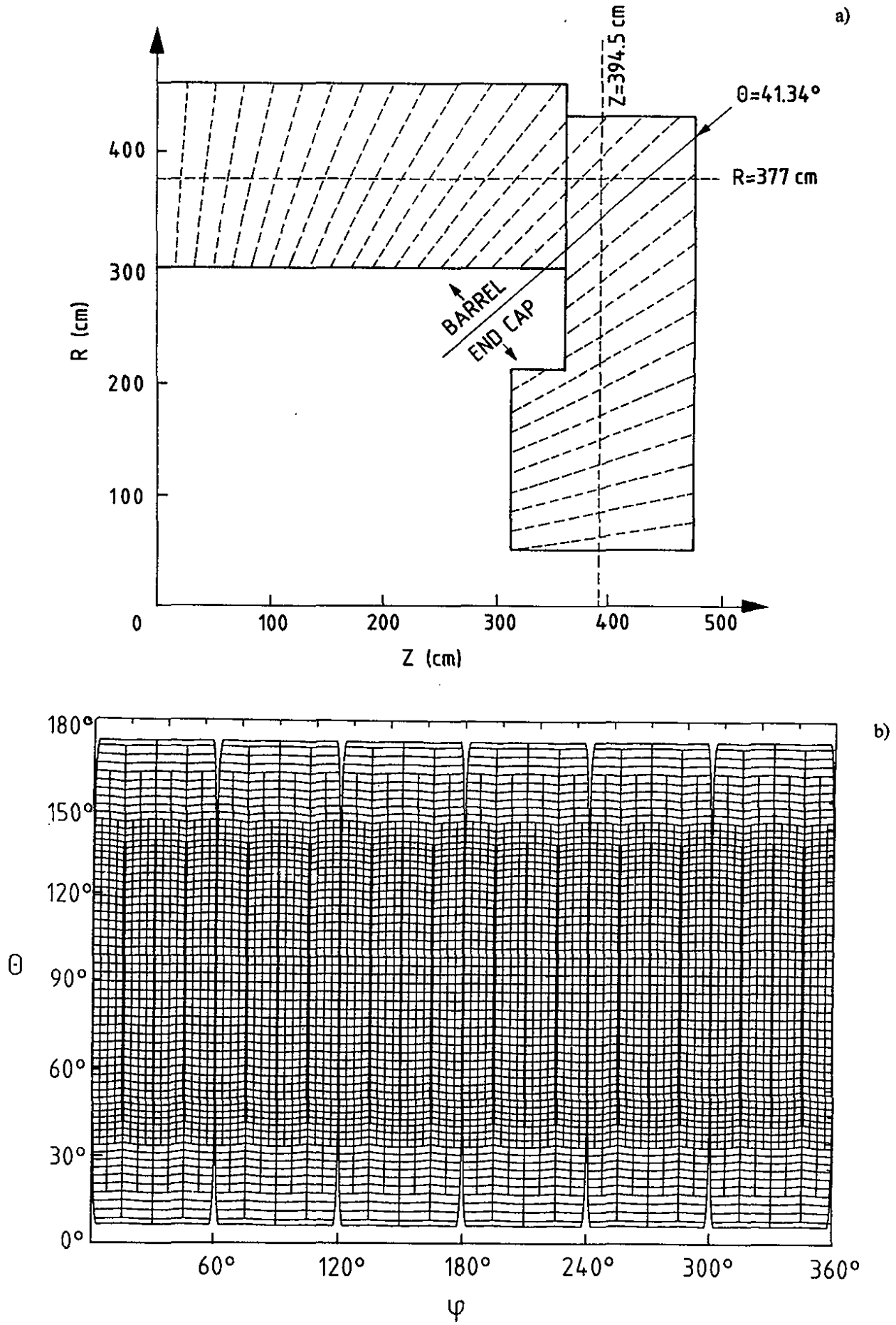
a)
Z=394.5 cm
θ=41.34°
R=377 cm
BARREL
END CAP
R (cm)
400
300
200
100
0
100
200
300
400
500
Z (cm)
b)
180°
150°
120°
90°
60°
30°
0°
θ
60°
120°
180°
240°
300°
360°
φ

Fig. 45

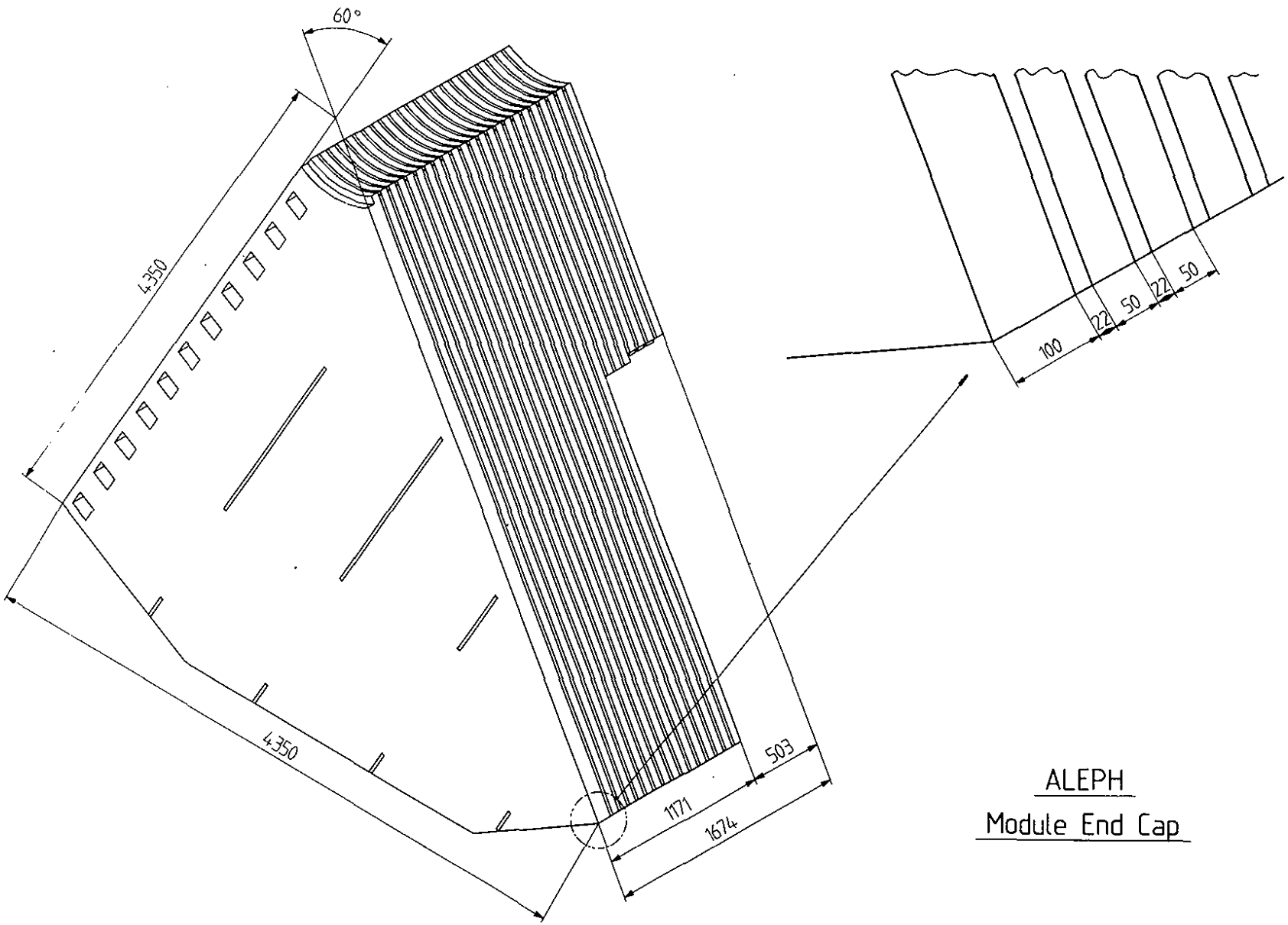

Fig. 46

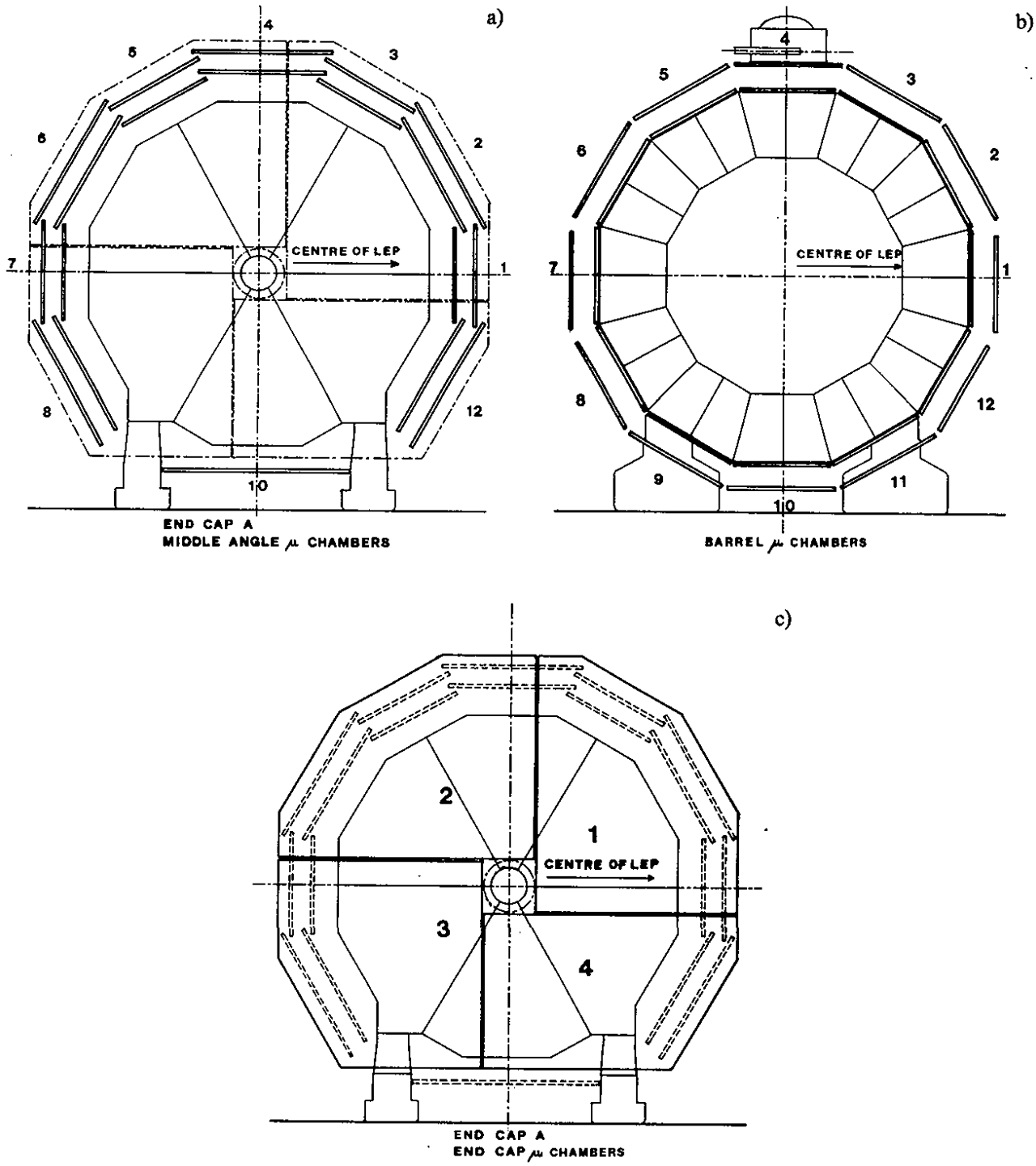
a)
4
5
3
6
2
CENTRE OF LEP
7
1
8
12
10
END CAP A
MIDDLE ANGLE μ CHAMBERS
b)
4
5
3
6
2
CENTRE OF LEP
7
1
8
12
9
11
10
BARREL μ CHAMBERS
c)
2
1
CENTRE OF LEP
3
4
END CAP A
END CAP μ CHAMBERS

Fig. 47

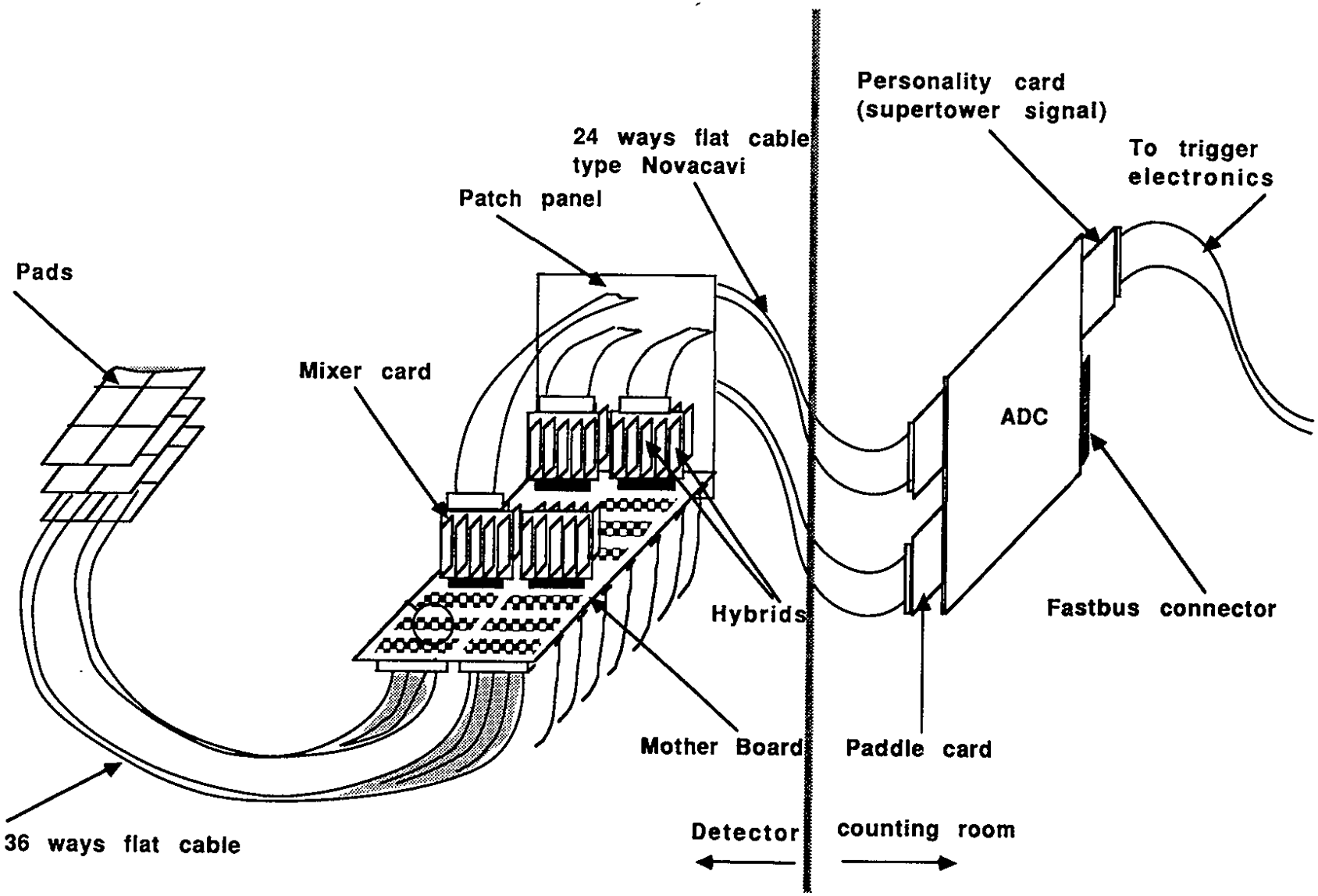
Personality card
(supertower signal)
24 ways flat cable
type Novacavi
To trigger
electronics
Patch panel
Pads
Mixer card
ADC
Hybrids
Fastbus connector
Mother Board
Paddle card
36 ways flat cable
Detector
counting room

Fig. 48

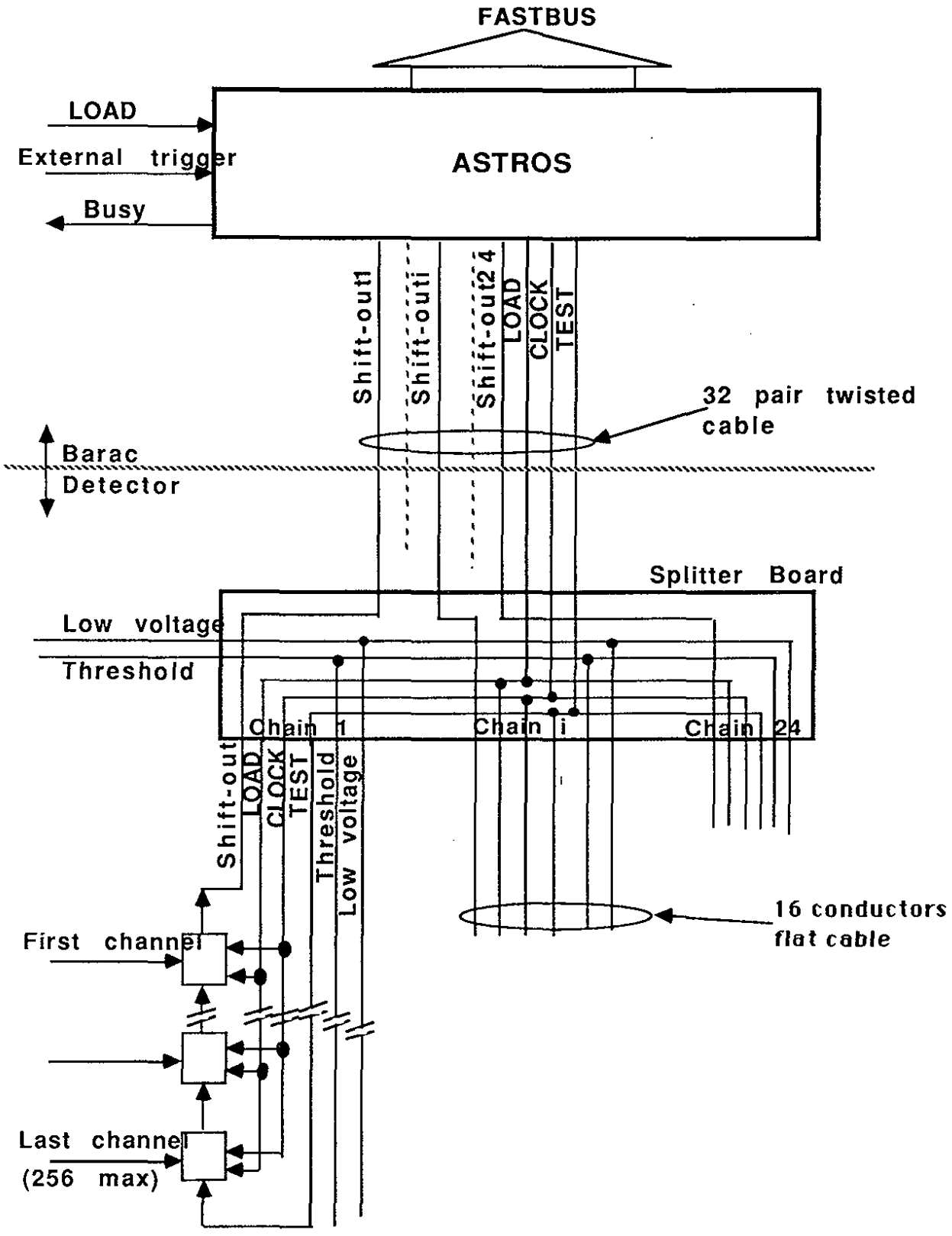
FASTBUS
LOAD
External trigger
Busy
ASTROS
Shift-out1
Shift-outi
Shift-out24
LOAD
CLOCK
TEST
32 pair twisted cable
Barac
Detector
Splitter Board
Low voltage
Threshold
Chain 1
Chain i
Chain 24
Shift-out
LOAD
CLOCK
TEST
Threshold
Low voltage
16 conductors flat cable
First channel
Last channel
(256 max)

Fig. 49

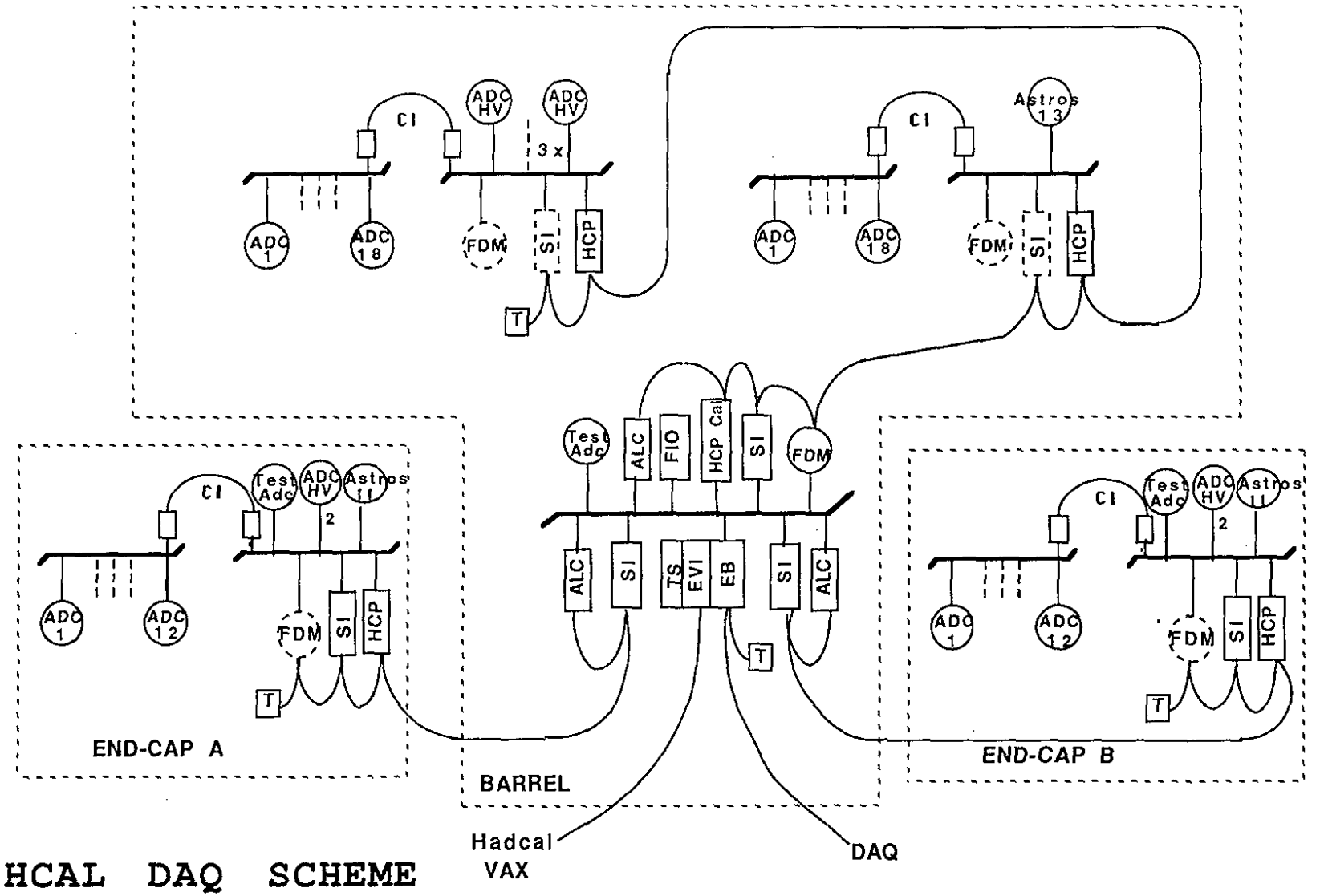

HCAL DAQ SCHEME

Fig. 50

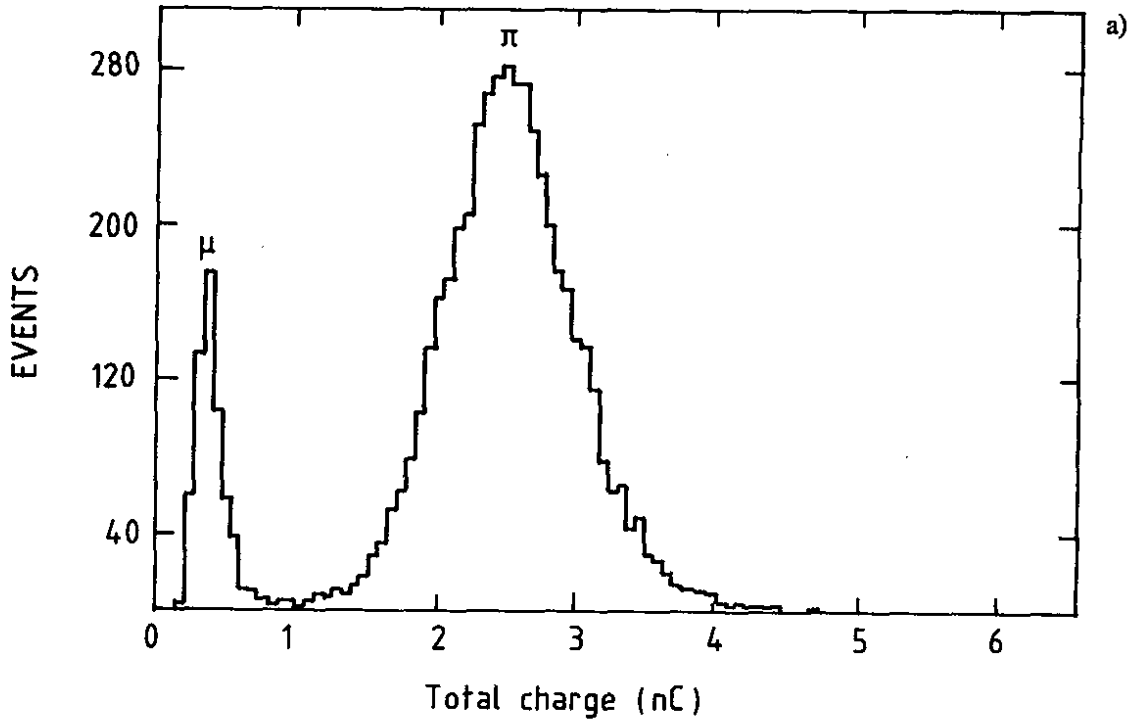
a)
EVENTS
280
200
120
40
μ
π
0
1
2
3
4
5
6
Total charge (nC)

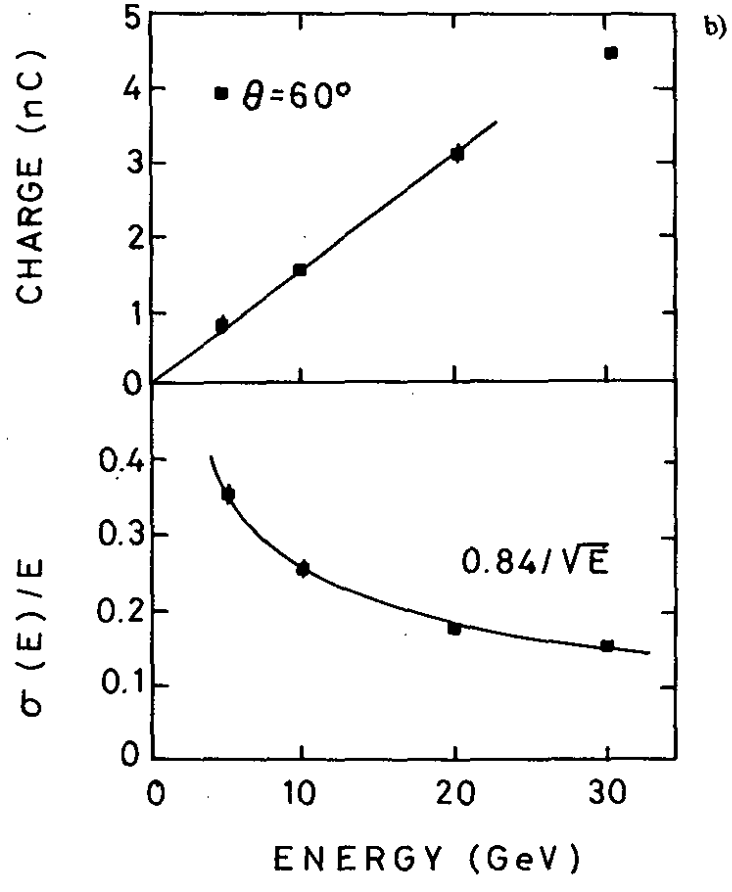
b)
CHARGE (nC)
θ=60°
5
4
3
2
1
0
σ(E)/E
0.4
0.3
0.2
0.1
0
0.84/√E
0
10
20
30
ENERGY (GeV)

Fig. 51

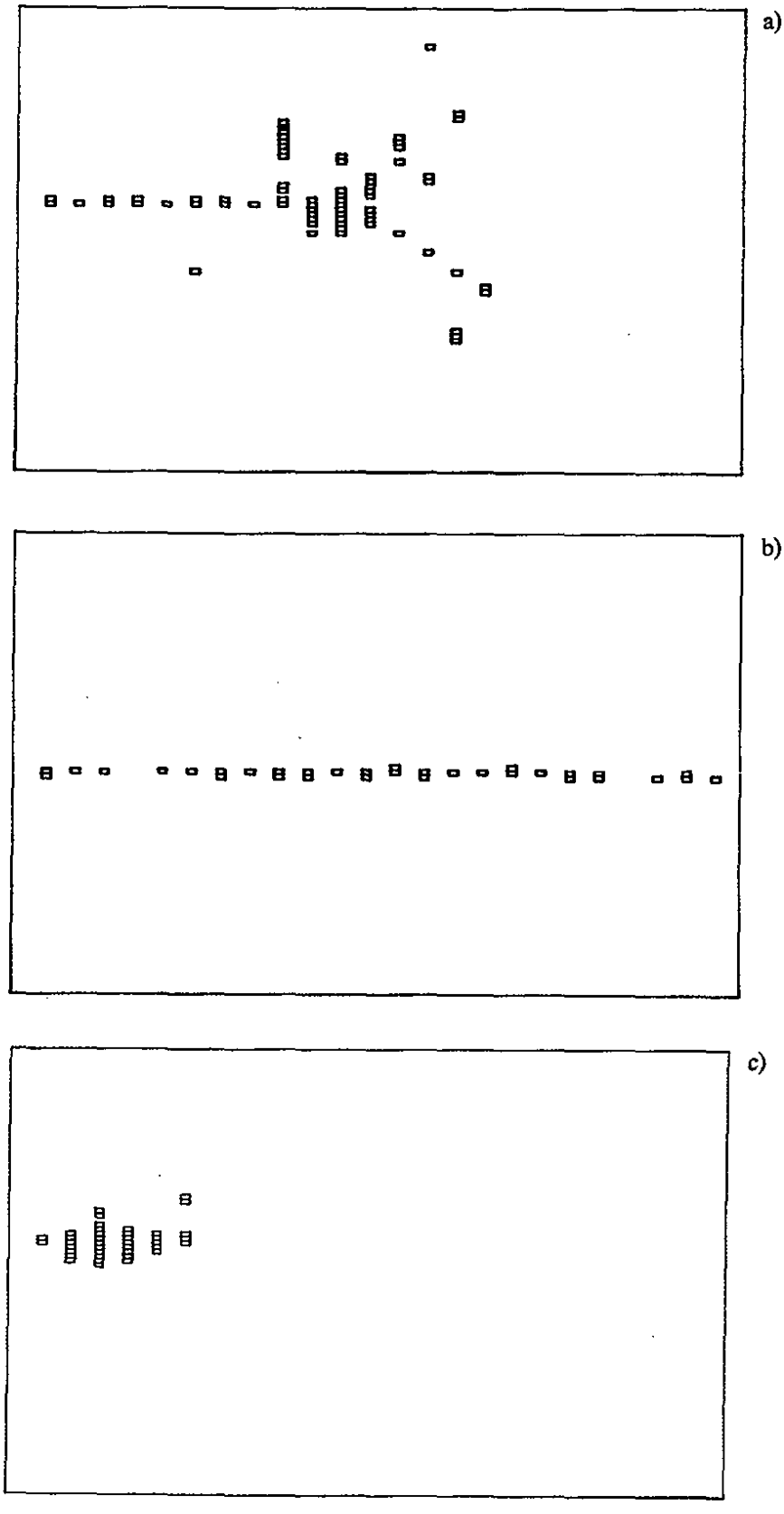

Fig. 52

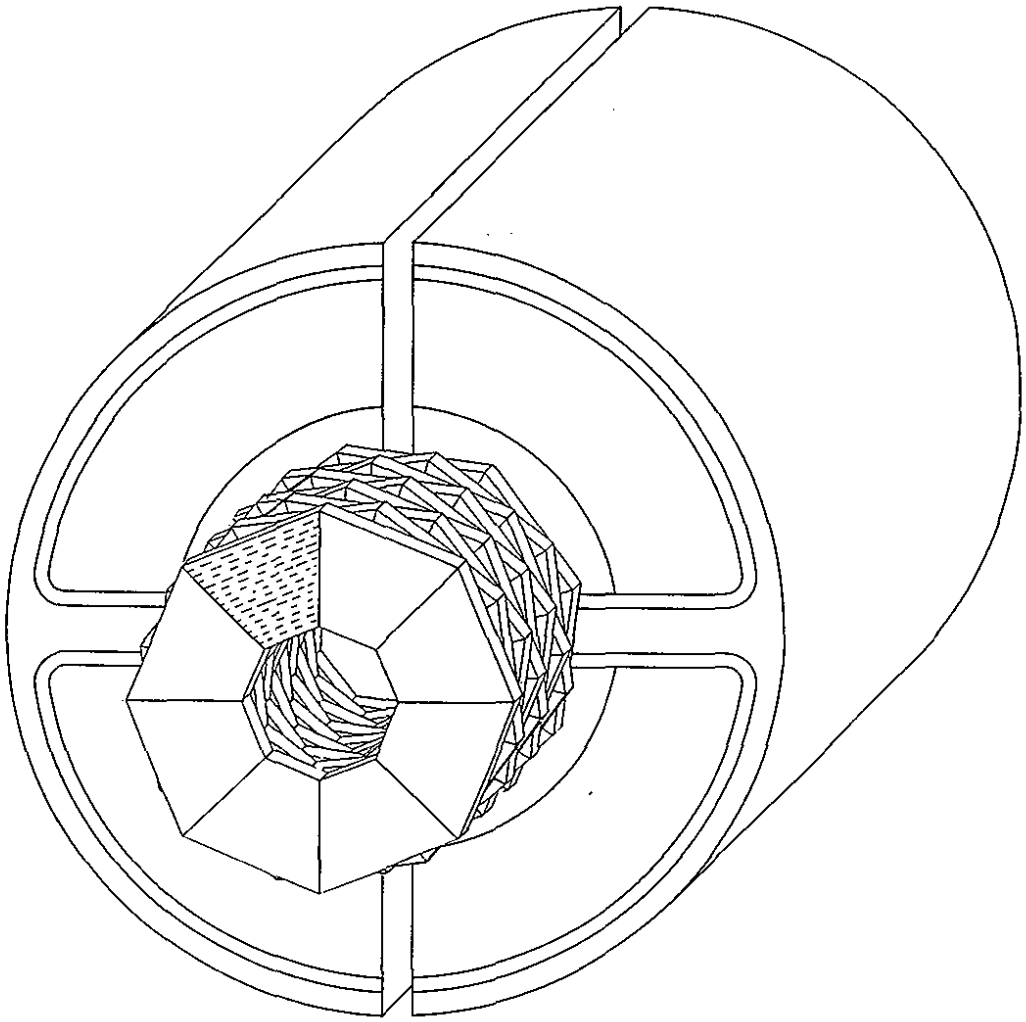

Fig. 53

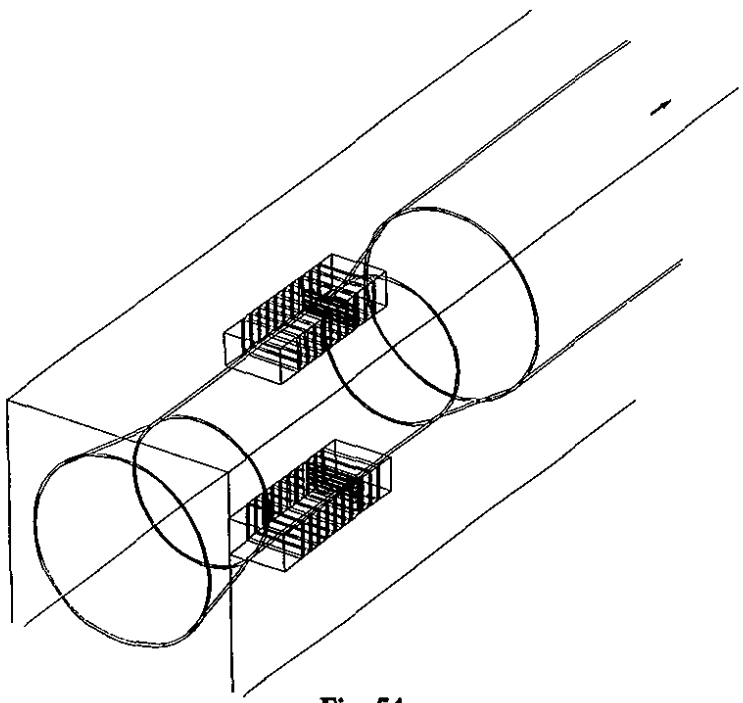

Fig. 54

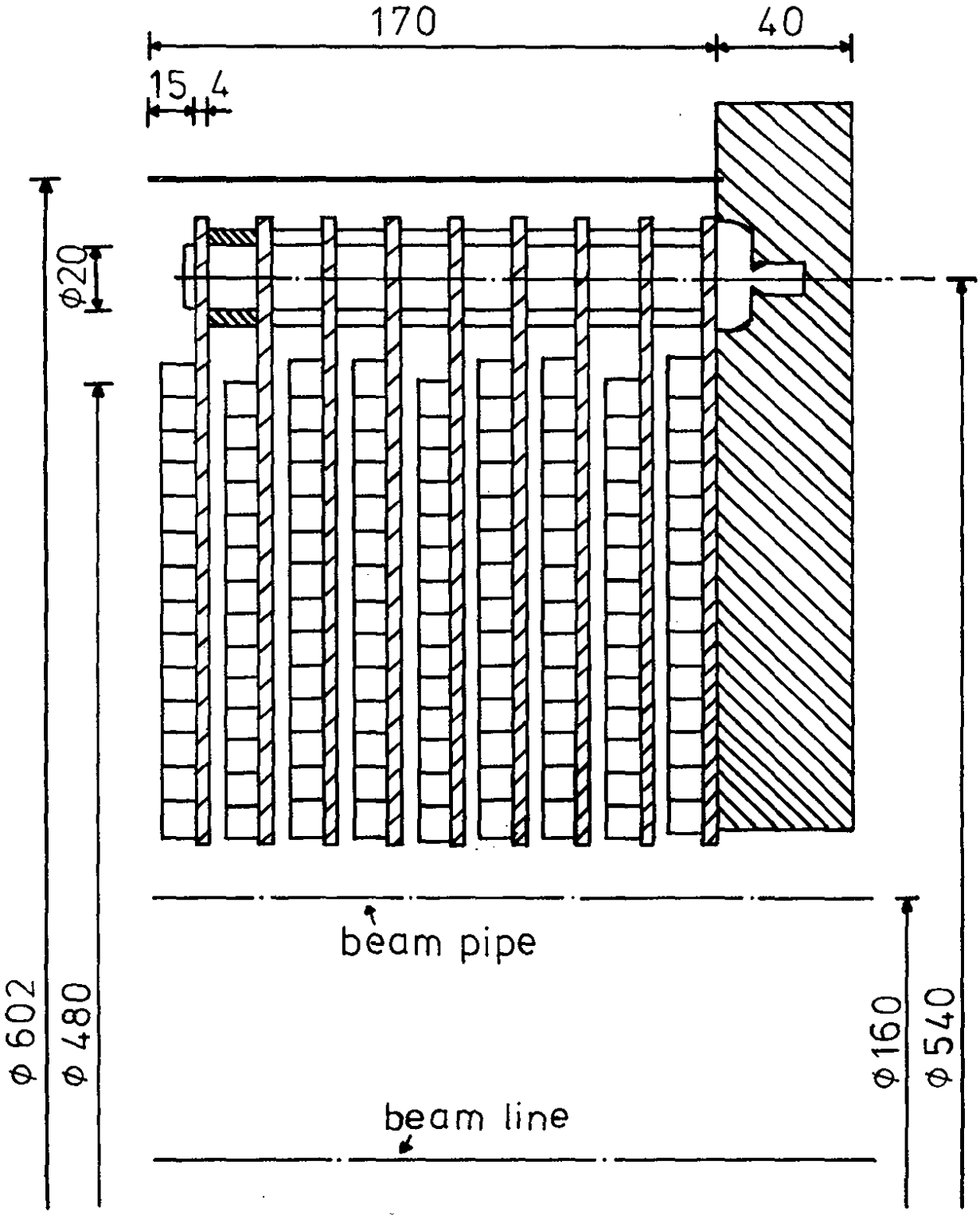

Fig. 55

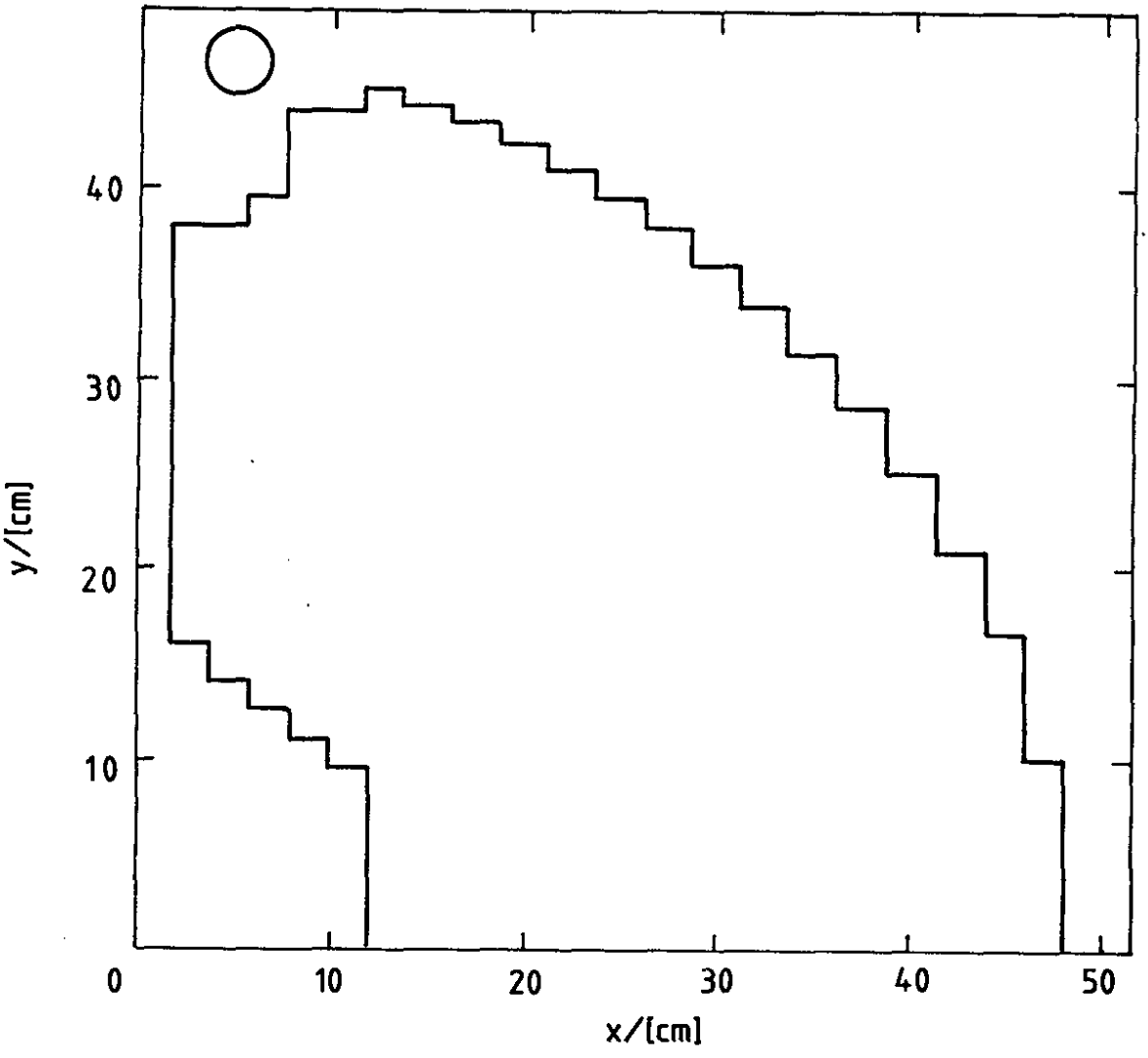

Fig. 56

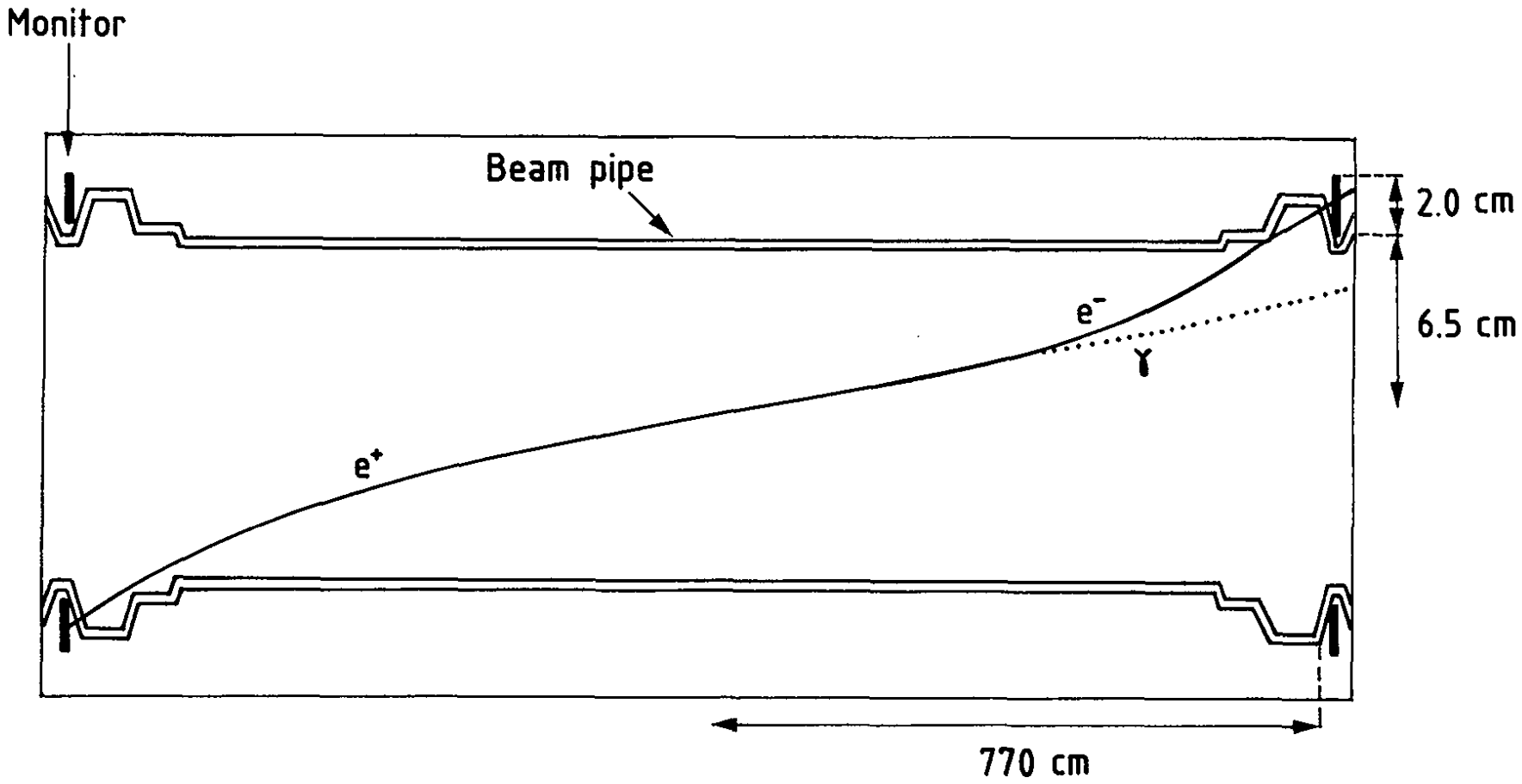

Fig. 57

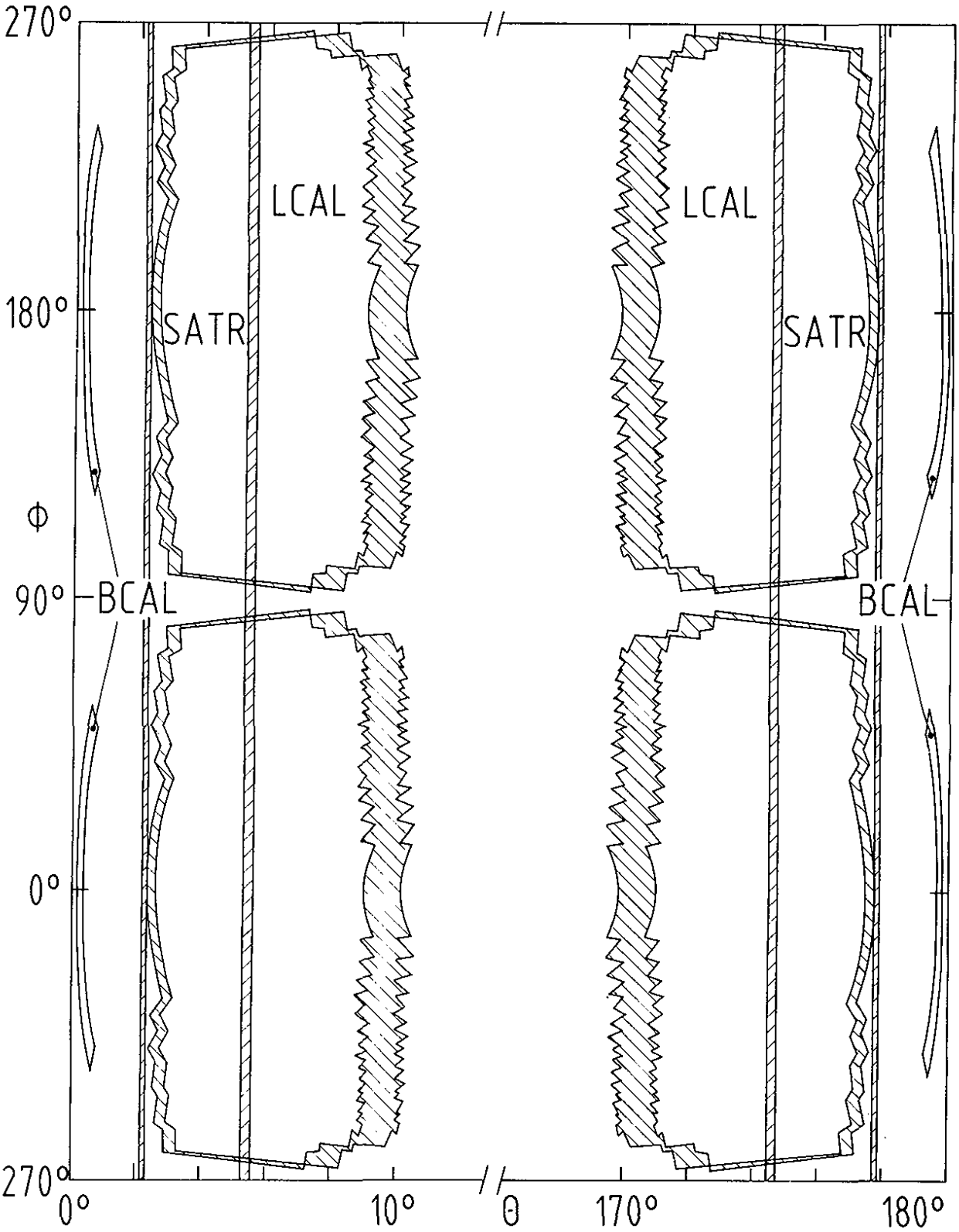

Fig. 58

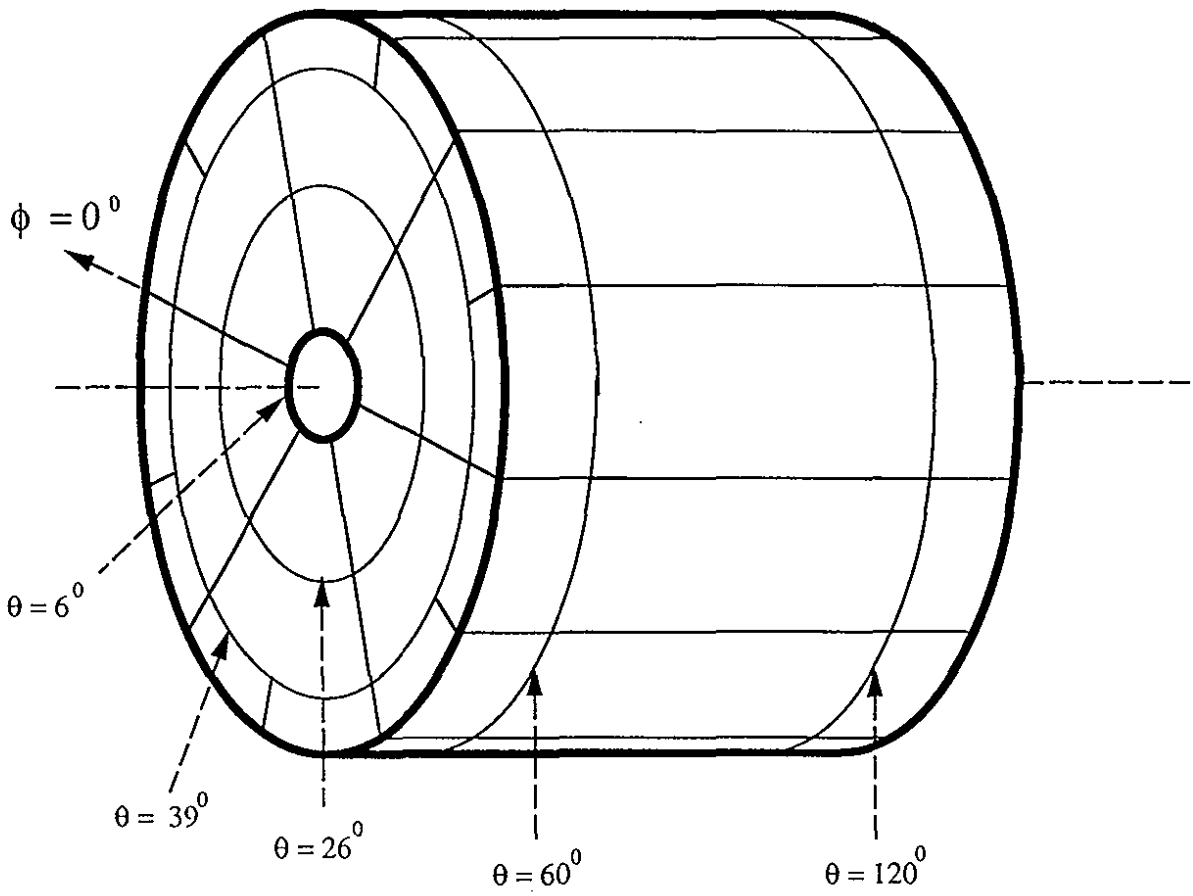

Fig. 59

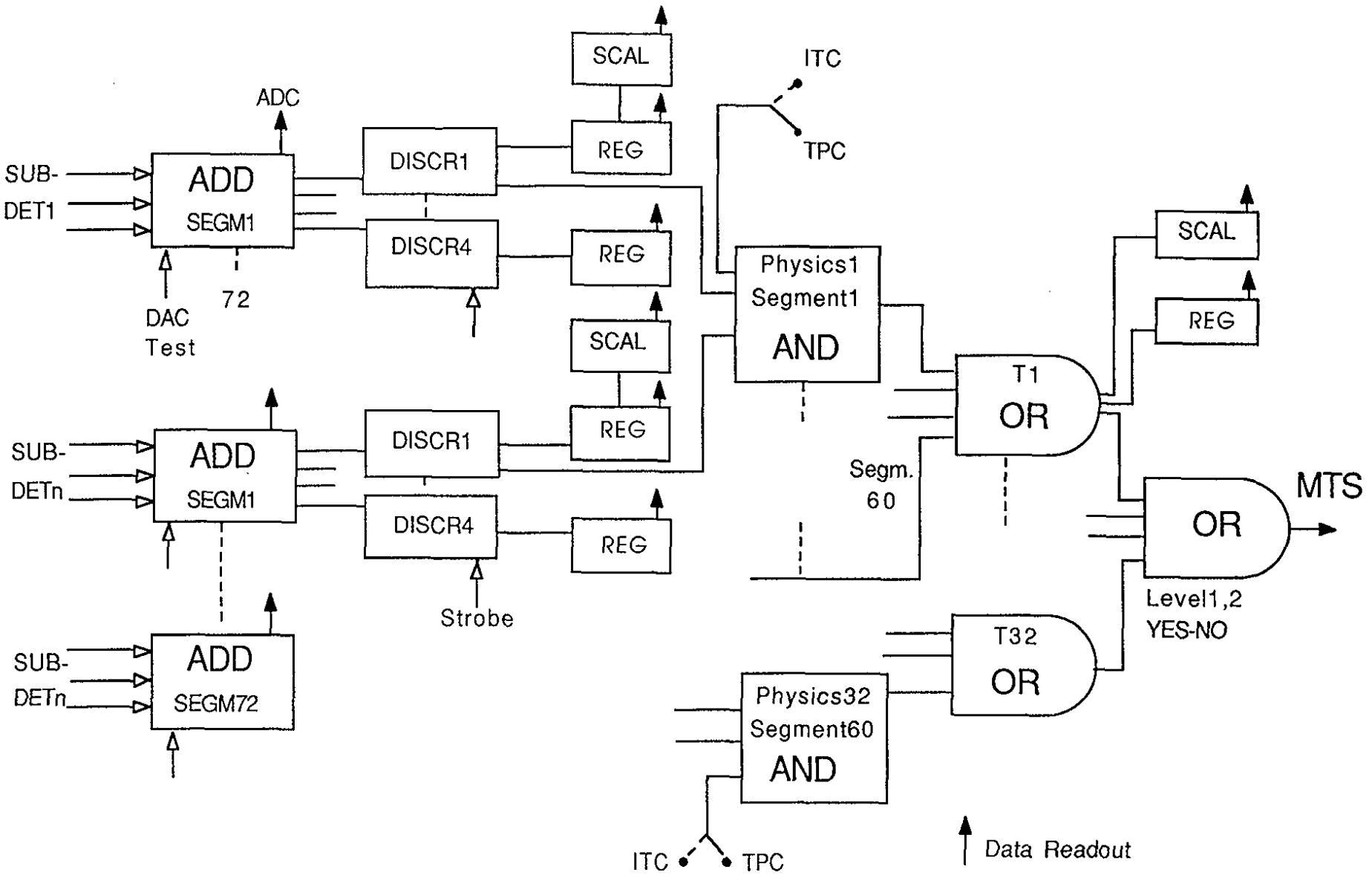
SCAL
ITC
ADC
TPC
SUB-
DET1
ADD
SEGM1
DISCR1
REG
DISCR4
REG
Physics1
Segment1
AND
SCAL
REG
DAC
Test
72
SCAL
T1
OR
REG
SUB-
DETn
ADD
SEGM1
DISCR1
REG
Segm.
60
MTS
DISCR4
REG
OR
Strobe
Level1,2
YES-NO
T32
OR
SUB-
DETn
ADD
SEGM72
Physics32
Segment60
AND
ITC
TPC
Data Readout

Fig. 60

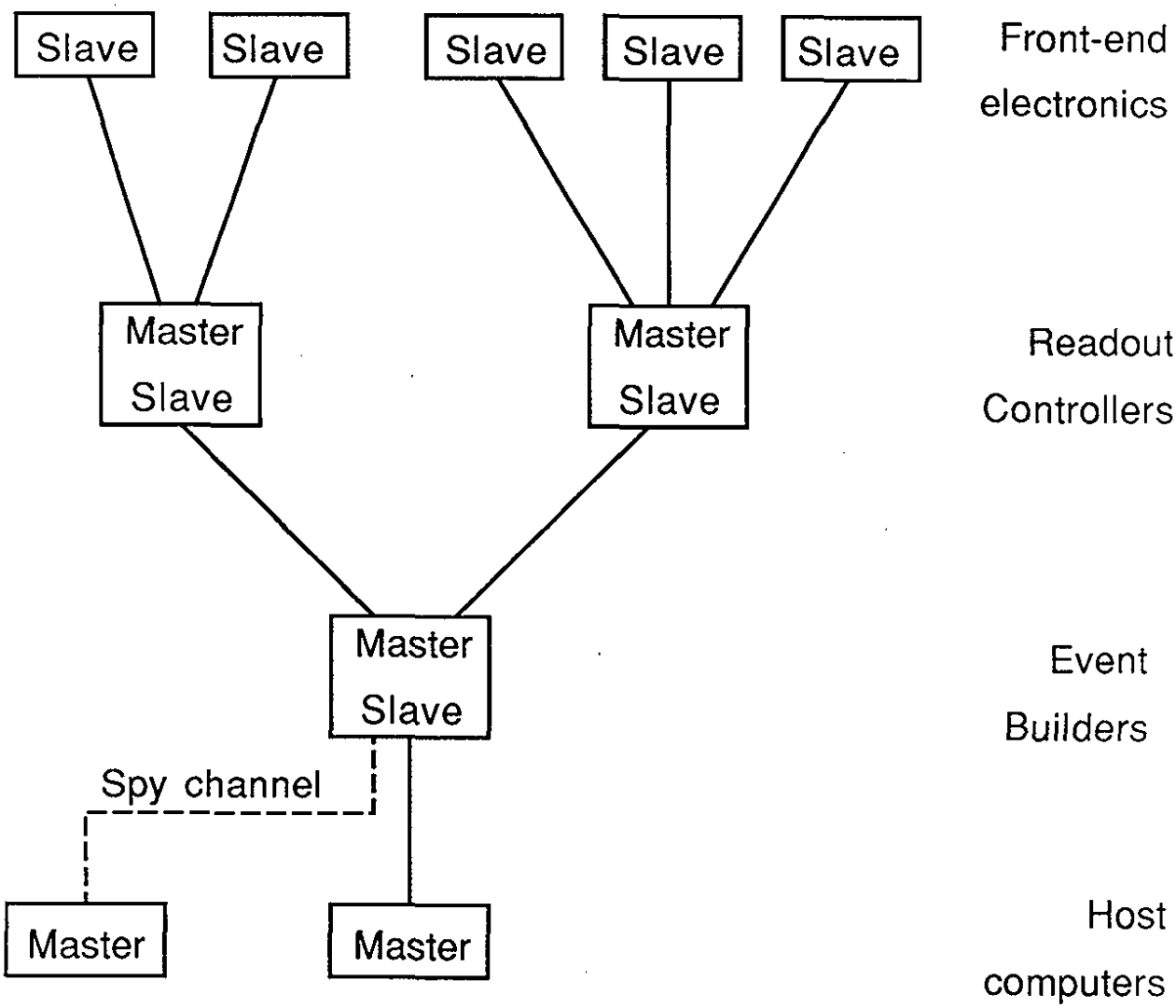
Slave
Slave
Slave
Slave
Slave
Front-end
electronics
Master
Slave
Master
Slave
Readout
Controllers
Master
Slave
Event
Builders
Spy channel
Master
Master
Host
computers

Fig. 61

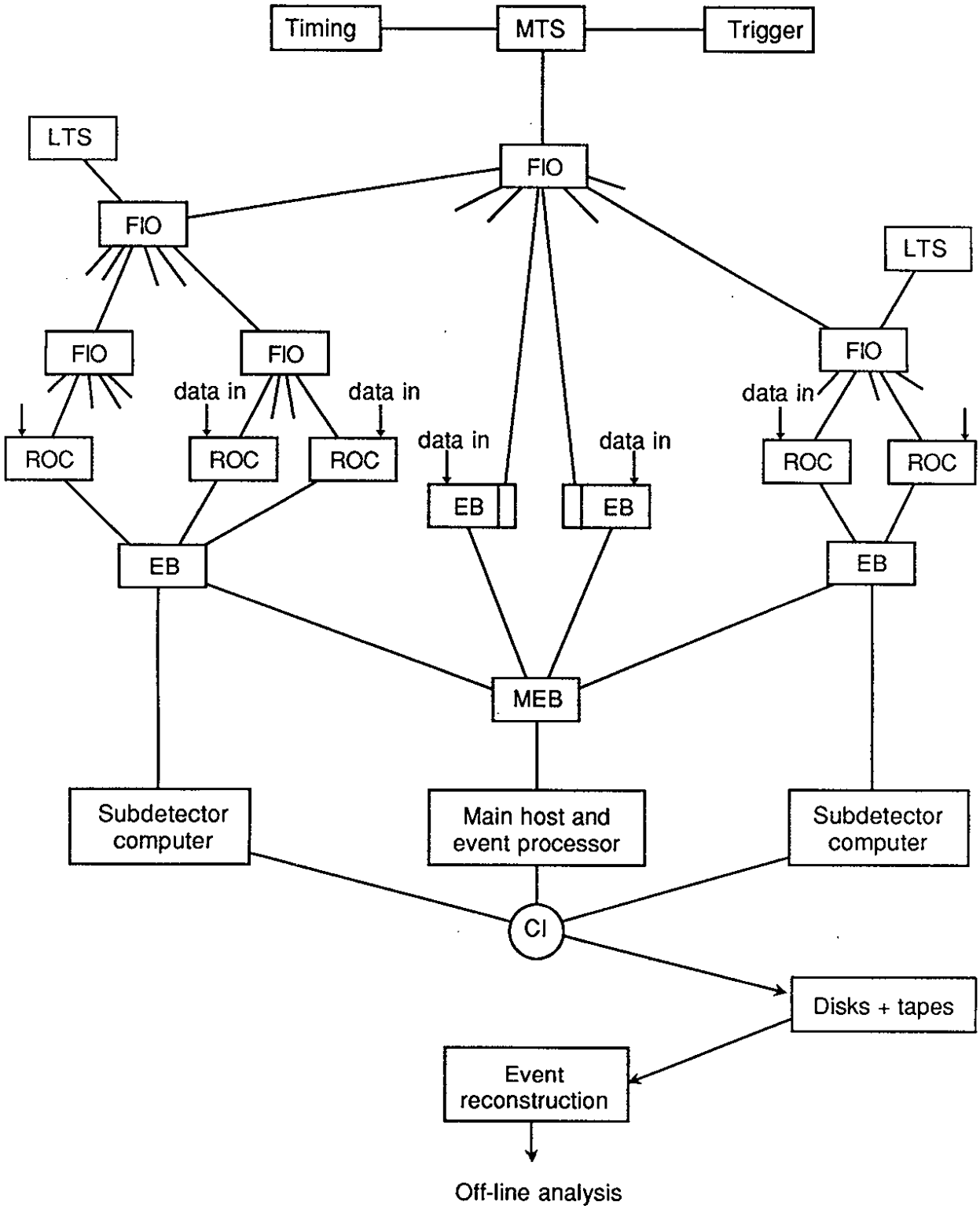
Timing
MTS
Trigger
LTS
FIO
FIO
LTS
FIO
FIO
FIO
data in
data in
data in
data in
data in
ROC
ROC
ROC
ROC
ROC
ROC
EB
EB
EB
EB
MEB
Subdetector computer
Main host and event processor
Subdetector computer
CI
Disks + tapes
Event reconstruction
Off-line analysis

Fig. 62

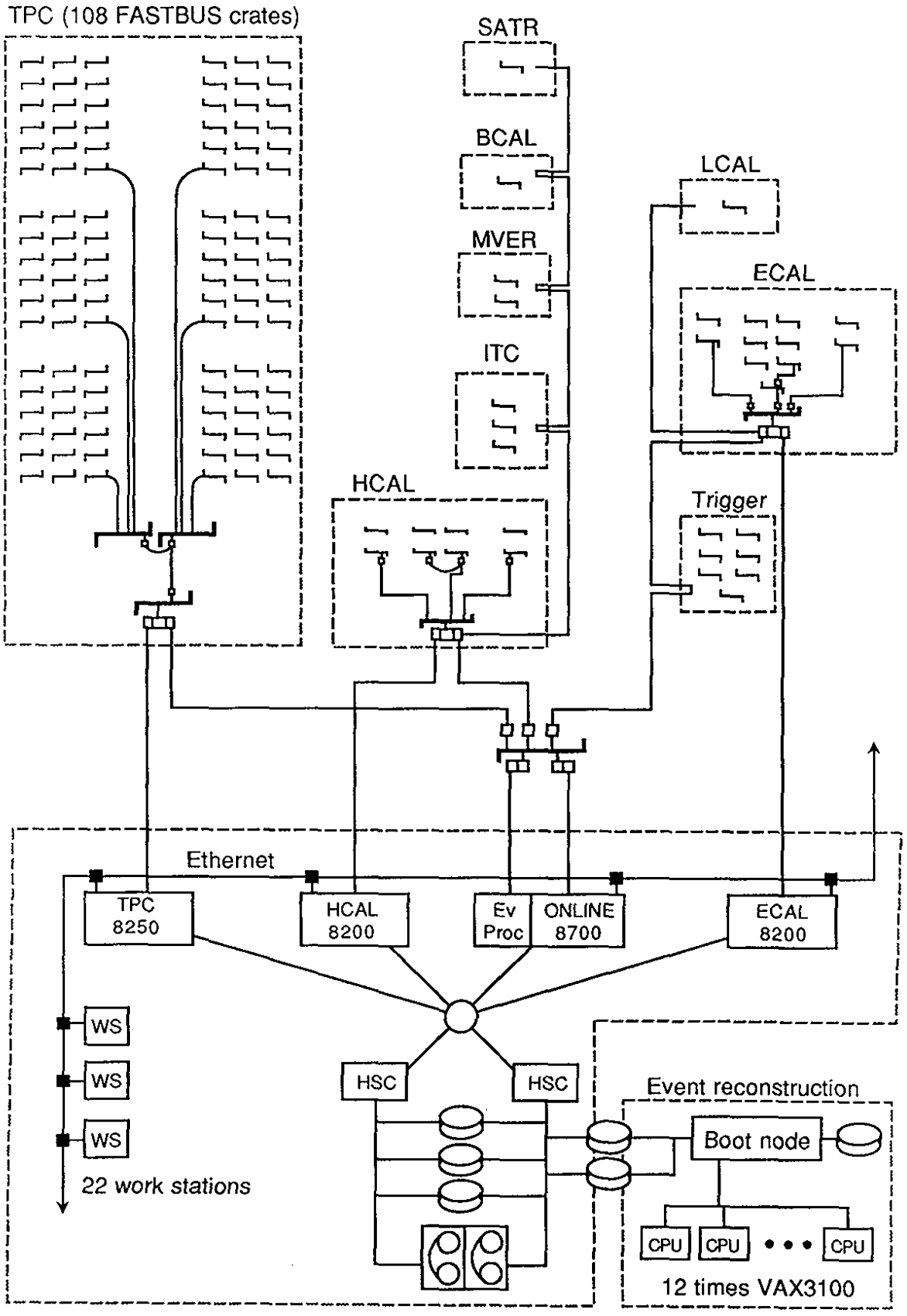
TPC (108 FASTBUS crates)
SATR
BCAL
MVER
ITC
HCAL
LCAL
ECAL
Trigger
Ethernet
TPC 8250
HCAL 8200
Ev Proc
ONLINE 8700
ECAL 8200
WS
WS
WS
22 work stations
HSC
HSC
Event reconstruction
Boot node
CPU
CPU
CPU
12 times VAX3100

Fig. 63

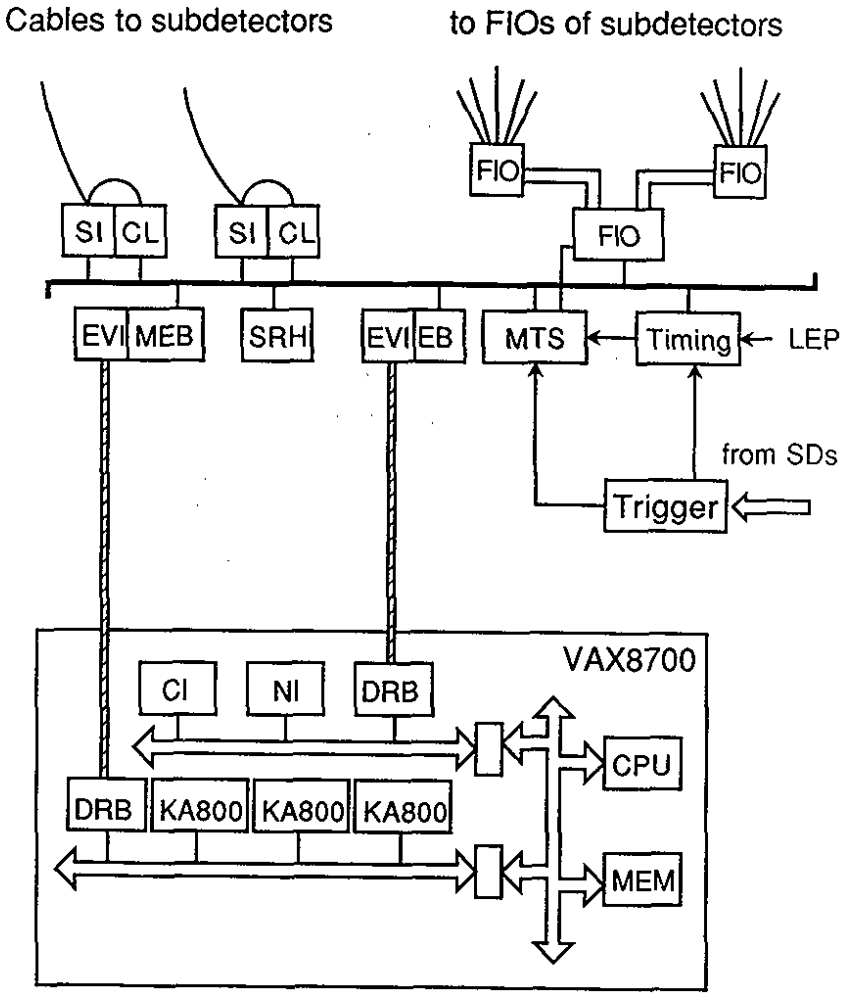
Cables to subdetectors
to FIOs of subdetectors
SI
CL
SI
CL
FIO
FIO
FIO
EVI
MEB
SRH
EVI
EB
MTS
Timing
LEP
from SDs
Trigger
VAX8700
CI
NI
DRB
CPU
DRB
KA800
KA800
KA800
MEM

Fig. 64

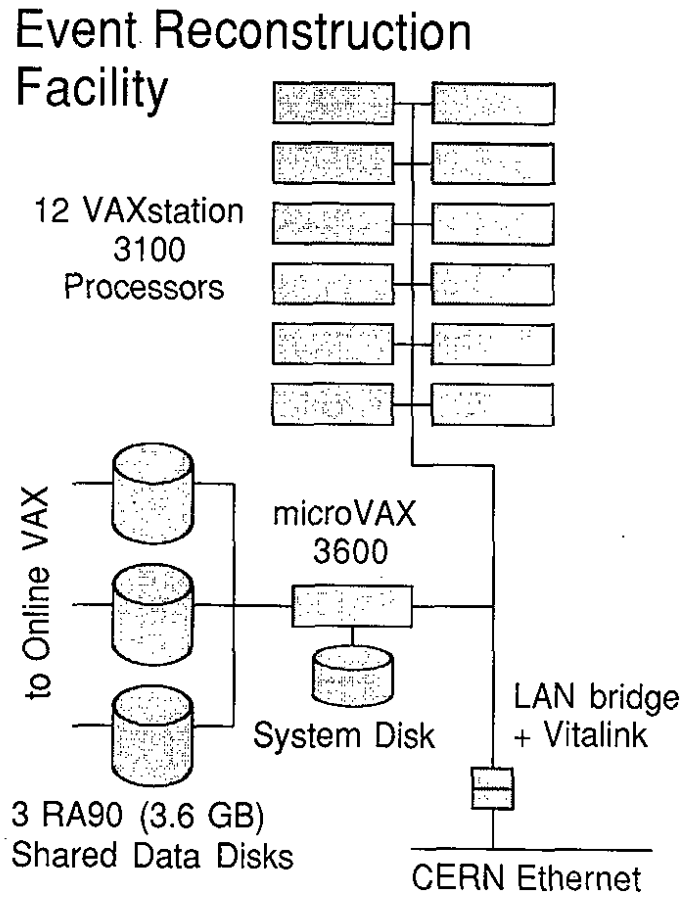
Event Reconstruction Facility
12 VAXstation 3100 Processors
to Online VAX
microVAX 3600
System Disk
LAN bridge + Vitalink
3 RA90 (3.6 GB) Shared Data Disks
CERN Ethernet

Fig. 65

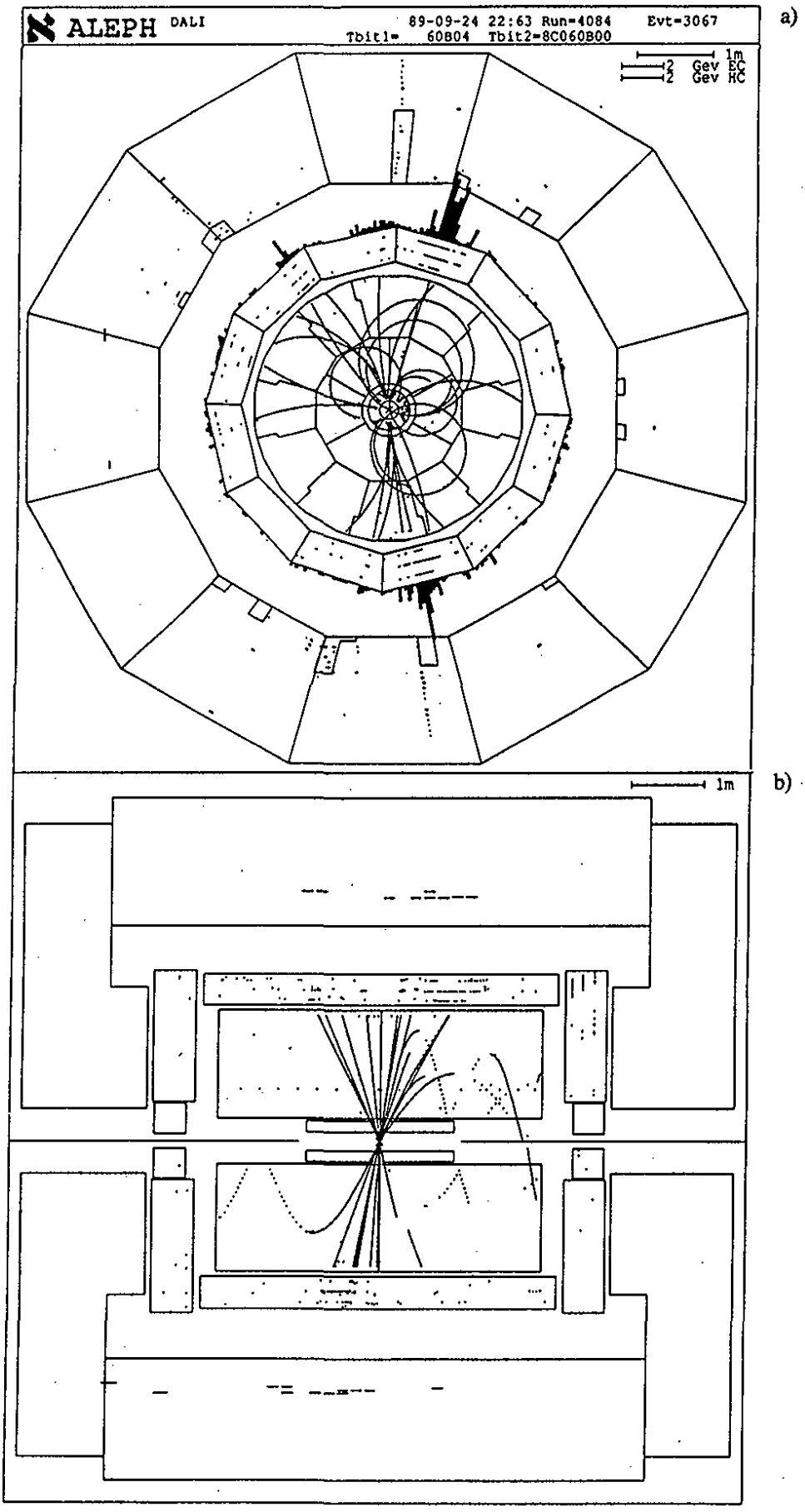
ALEPH DALI
89-09-24 22:63 Run=4084 Evt=3067
Tbit1= 60804 Tbit2=8C060B00
1m
2 Gev EC
2 Gev HC
a)
1m
b)

Fig. 66